Measurement of the B_s^0 Decay Widths at CMS with $B_s^0 \to J/\psi\ \phi$

Dissertation

zur

Erlangung der naturwissenschaftlichen Doktorwürde

(Dr. sc. nat.)
vorgelegt der

Mathematisch-naturwissenschaftlichen Fakultät

der

Universität Zürich

von

Bárbara Millán Mejías

aus

Venezuela

Promotionskomitee

Prof. Dr. C. Amsler (Vorsitz)
Prof. Dr. V. Chiochia
Dr. H. Snoek

Zürich, 2013

Contents

Abstract

This thesis focuses on the study of the decay channel $B_s^0 \to J/\psi\ \phi \to \mu^+\mu^- K^+K^-$ to measure the width difference $|\Delta\Gamma_s|$ between the light and heavy eigenstates of the B_s^0 meson. The analysis is performed using a data sample of proton-proton collisions at $\sqrt{s} = 7$ TeV, corresponding to an integrated luminosity of 5 fb^{-1} and recorded by the CMS detector at the LHC.

First, the reconstruction and selection of the $B_s^0 \to J/\psi\ \phi \to \mu^+\mu^- K^+K^-$ decay channel is presented. In this channel, the four-track candidates are displaced from the primary vertex due to the decay of the B_s^0 meson. The trigger selection requires di-muon events with the presence of a J/ψ candidate with a vertex displaced from the primary vertex. Monte Carlo samples are used to validate the theoretical models, the contributions of the possible background processes, and the event selection techniques. The comparison of results of the different possible triggers obtained from real data and from simulation studies confirm that the triggering and selection methods used are appropriate for selecting the $B_s^0 \to J/\psi\ \phi \to \mu^+\mu^- K^+K^-$ decay channel. After applying all selection cuts, 19 200 $B_s^0 \to J/\psi\ \phi \to \mu^+\mu^- K^+K^-$ event candidates are obtained. A full untagged angular analysis is performed to disentangle the mass eigenstates of the B_s^0 meson and to extract the parameters $\tau_s = 1/\Gamma_s$, $|\Delta\Gamma_s|$, $|A_0|^2$, $|A_\perp|^2$, and the strong phase $\delta_{||}$. A fitting technique is developed based on the maximum-likelihood method. This thesis assumes a vanishing CP violating phase ϕ_s, predicted to be very small in the Standard Model. The multiple likelihood fit is performed in several steps. First, the B_s^0 invariant mass distribution is fitted between [5.24, 5.49] GeV/c^2. Then, the sideband regions are fitted with the empirical model that defines the background. In a third step, the likelihood fit is performed on the selected events and the physical parameters are extracted. Finally, 14 556 $\pm$ 139 signal events are found with a lifetime difference of $|\Delta\Gamma_s| = 0.048 \pm 0.024$ (stat.) $\pm$ 0.003 (syst.) ps^{-1}, and the average lifetime $\tau_s = 1.527 \pm 0.020$ (stat.) $\pm$ 0.010 (syst.) ps.

Zusammenfassung

Diese Dissertation behandelt die Untersuchung des Zerfallskanals $B_s^0 \to J/\psi\ \phi \to \mu^+\mu^-K^+K^-$, um die Differenz der Zerfallsbreiten $|\Delta\Gamma_s|$ zwischen den leichten und schweren Eigenzuständen des B_s^0 Mesons zu messen. Die Analyse wird mit einem Datensatz von Proton-Proton Kollisionen durchgeführt, der einer integrierten Luminosität von 5 fb^{-1} entspricht, und der bei einer Schwerpunktsenergie von $\sqrt{s} = 7$ TeV vom CMS Detektor gesammelt wurde. Zuerst wird die Rekonstruktion und Selektion des $B_s^0 \to J/\psi\ \phi \to \mu^+\mu^-K^+K^-$ Zerfallskanals präsentiert. Wegen des B_s^0-Zerfalls sind in diesem Kanal die Vier-Spur Kandidaten vom Primärvertex versetzt. Ein Trigger selektiert Ereignisse mit zwei Müonen und einem Kandidaten für ein J/ψ mit einem vom Primärvertex verschobenen Zerfallsvertex. Monte Carlo Daten werden benutzt um die theoretischen Modelle, die Beiträge von möglichen Hintergrund-Ereignissen, und die Techniken für die Ereignis-Selektion zu validieren. Der Vergleich der Resultate simulierten Daten der verschiedenen möglichen Trigger bestätigt, dass das benutzte Triggering und die Selektions-Methoden geeignet sind, um den $B_s^0 \to J/\psi\ \phi \to \mu^+\mu^-K^+K^-$ Zerfalls-Kanal zu isolieren.
Nach der Anwendung aller Selektionskriterien bleiben 19 200 $B_s^0 \to J/\psi\ \phi \to \mu^+\mu^-K^+K^-$ Ereigniskandidaten. Eine volle Winkelanalyse ohne Tagging wird durchgeführt, um die beiden Masseneigenzustände des B_s^0 Mesons zu separieren, und um die Parameter $\tau_s = 1/\Gamma_s$, $|\Delta\Gamma_s|$, $|A_0|^2$, $|A_\perp|^2$, und die starke Phase $\delta_{||}$ zu erhalten. Eine Fit-Technik basierend auf der Maximum-Likelihood Methode wird entwickelt. Diese Dissertation benutzt die Annahme einer verschwindenden CP-verletzenden Phase ϕ_s, im Standard Modell als sehr klein vorhergesagt wird. Der Multiple-Likelihood Fit wird in mehreren Schritten durchgeführt. Zuerst wird die invariante Masse des B_s^0 Mesons zwischen [5.24, 5.49] GeV/c^2 gefittet. Danach werden die Seitenband Regionen mit einem empirischen Modell gefittet, welches die Hintergrund-Prozesse definiert. Im dritten Schritt wuden die physikalischen Parameter extrahiert. Schlussendlich werden 14 556 $\pm$ 139 Signalereignisse gefunden mit $|\Delta\Gamma_s| = 0.048\ \pm\ 0.024$ (stat.) $\pm\ 0.003$ (syst.) ps^{-1}. Die mittlere Lebensdauer ist $\tau_s =\ 1.527\ \pm 0.020$ (stat.) $\pm\, 0.010$ (syst.) ps.

Chapter 1

Introduction

The Standard Model (SM) [1] is a collection of theories that explains how particles interact with the forces that govern nature, containing our present-day understanding of fundamental particles. Since the establishment of the Standard Model, in the 60s and 70s, it has been tested by different experiments, being very successful in predicting a large number of physics phenomena. However, many questions remain unanswered, and our comprehension of the universe is still incomplete. The Large Hadron Collider (LHC) [2] at the European Laboratory for Particle Physics CERN was designed to study fundamental particles and its interactions, hoping to answer some of these fundamental questions.

These questions can be grouped in four main topics. One topic is the explanation of the origin of mass, which started to be clarified when a "Higgs" like particle was announced by two of the main experiments of the LHC (CMS and ATLAS) in 2012 [3, 4], and later confirmed in March 2013. The second topic is related to how all fundamental forces are unified. The third topic is the search for additional elementary particles that could explain the observational evidence that the visible matter is only 4 % of the Universe [5, 6]. And finally, the fourth topic, and the one related to this thesis, is the study of the properties of antimatter.

After the Big Bang matter and antimatter must have been produced in equal quantities, but astronomical experiments and studies of the cosmic microwave background show that the visible universe is composed mostly of matter [7]. Therefore, there must have been a mechanism that produced an imbalance in the Universe. In principle, the difference between matter and antimatter could be explained by the C-charge and P-parity (CP) violating processes in the weak interactions. However, the levels of CP violation predicted by the Standard Model are not able to explain the imbalance of anti-matter in the universe.

The study of B mesons is nevertheless interesting since it allows to measure characteristics of matter and anti-matter, because neutral B mesons oscillate between their particle and their anti-particle state. Particularly, when studying the characteristics of the B_s^0 mesons it is possible to constrain fundamental parameters of the flavor model such as the CP violating parameter ϕ_s. The constrained parameters hint to the presence of physics beyond the Standard Model, and to different models that would explain the imbalance of matter and anti-matter in the universe.

This dissertation presents an untagged angular analysis of the $B_s^0 \to J/\psi\ \phi$ decay channel, in order to determine the difference in partial widths $|\Delta\Gamma_s|$ and the mixing amplitudes. The analysis is called untagged because no distinction is made between B_s^0 and $\bar{B}_s^0$ mesons. In this channel the J/ψ meson decays into $\mu^+\mu^-$ and the $\phi(1020)$ meson decays into K^+K^-. The data used are proton-proton collisions collected by the CMS detector at a center of mass energy of 7 TeV.

The outline of this dissertation is as follows. Chapter 2 presents the CP violation principles, their inclusion in the Standard Model through the CKM matrix, and how the CKM parameters are related to the $B_s^0 \to J/\psi\ \phi$ decay channel. In the same chapter, the details about the B_s^0-$\bar{B}_s^0$ mixing, and the analysis strategy to measure the $B_s^0 \to J/\psi\ \phi$ decay width are explained. Chapter 3 describes the Compact Muon Solenoid (CMS) experiment, the trigger chain used to select the $B_s^0 \to J/\psi\ \phi$ signal candidates, and the process of particle decay reconstruction. Chapter 4 explains the reconstruction and details of the selection of the $B_s^0 \to J/\psi\ \phi$ signal candidates, while trying to eliminate as much as possible the background. Chapter 5 describes the implementation of the untagged angular analysis. This chapter presents the validations of different Probability Density Functions (PDF) components, the implementation of the multiple likelihood fit, validates the calculus of the resolution effects and the different efficiencies present in the analysis, and explains all the systematic uncertainties accounted for in this thesis. Finally, Chapter 7 shows the final results of this work and compares them with other experiments.

This thesis is an extension on the internal and public notes of the CMS collaboration for which I was one of the main authors:

- "Measurement of the lifetime difference $\Delta\Gamma_s$ in the decay $B_s \to J/\psi\ \phi$", G. Fedi, B. Millán Mejías, V. Jha, and G. Cerizza. [8].
- "Measurement of the B_s lifetime difference", CMS Collaboration. [9].

Chapter 2

Theoretical description

Since combined Charge and Parity (CP) violation effects were discovered in the $K^0 - \bar{K^0}$ system in 1964 [10], CP violation has been one of the main topics of study in particle physics. CP symmetry violation is a consequence of the Standard Model with three quark generations. The CP violation predictions in the Standard Model are governed by the Cabibbo-Kobayashi-Maskawa (CKM) mechanism [11], which contains a (3×3) matrix with complex coupling constants [12].

By studying the B decays it is possible to obtain direct information on parameters of the CKM matrix and the complex phases that are related to the CP violation occurrences. In particular, this thesis discusses the occurrence of CP violation in the mixing and decay between B_s^0-$\bar{B}_s^0$ mesons, by studying the decay channel $B_s^0 \to J/\psi\,\phi$. The final state $B_s^0 \to J/\psi\ \phi$ is a mixture of CP-even, and CP-odd eigenstates. Therefore, to extract parameters like the polarization phases and the difference in partial widths $\Delta\Gamma_s$, it is necessary to perform an angular analysis as a function of decay time.

This chapter provides a brief description of the role of CP violation in the Standard Model and the advantages of studying the $B_s^0 \to J/\psi\ \phi$ decay channel. First, the inclusion of the CKM matrix in the Standard Model to accommodate the CP violation is explained. Then, the B_s^0-$\bar{B}_s^0$ mixing and the time dependent angular expressions that describe $B_s^0 \to J/\psi\ \phi$ are given. The latest results on the CP asymmetry for $B_s^0 \to J/\psi\ \phi$ channel are presented. Finally, the analysis strategy is discussed.

2.1 CP Violation

In field theory there are three discrete types of transformations: Charge C, parity P, and time T. The charge conjugation C transforms the particle into its antiparticle while other properties of the particle remain unchanged. The parity operator P exchanges the sign of all spatial coordinates. Finally, the time reversal T, reverses the time flow in the physical process. The combination of the three transformations, CPT, is an exact symmetry in many Lagrangian field theory [13]. It has been shown experimentally that electromagnetism and strong interaction are symmetric with respect to the operators C, P, and T [12]. It was assumed that the electroweak interaction was invariant to the CPT transformations as well, until 1957, when the weak interaction was confirmed by experiments to violate parity P [14]. Later, in 1964, the CP violation in the neutral kaon system was observed [10]. To describe the CP violation within the Standard Model, it was necessary to introduce three or more generations of quarks. This inclusion was done in 1973 [11] and led to the prediction of the top and b quarks, which were later discovered experimentally [15, 16].

2.2 The CKM quark-mixing matrix

The CP violation was included in the Standard Model through the charged weak currents interaction. The charge weak current is defined as follows:

$$J^{\mu^-} = (\bar{u_L}\bar{c_L}\bar{t_L})\gamma^\mu \hat{V}_{CKM} \begin{pmatrix} d_L \\ s_L \\ b_L \end{pmatrix}, \tag{2.1}$$

with γ^μ the Dirac matrix, and V_{CKM} the 3×3 Cabibbo-Kobayashi-Maskawa (CKM) matrix. The charge current interaction is represented as:

$$\mathcal{L}_W = \frac{g}{\sqrt{2}} J^{\mu^-} W_\mu^- + h.c., \tag{2.2}$$

where g is the weak coupling constant, and W_μ^- is the charged vector boson. The CKM matrix relates the weak eigenstates with the three quark generations in the Standard Model , establishing the relative strength of the weak charge couplings between different quark flavors.

As can be seen in Eq. (2.1) the 3×3 CKM matrix operates on the three down type quarks (d, s, b) [11]. The weak eigenstates d', s', and b' are related to the mass eigenstates through the CKM matrix like:

$$\begin{pmatrix} d' \\ s' \\ b' \end{pmatrix} = V_{CKM} \begin{pmatrix} d \\ s \\ b \end{pmatrix}, \tag{2.3}$$

where:

$$V_{CKM} = \begin{pmatrix} V_{ud} & V_{us} & V_{ub} \\ V_{cd} & V_{cs} & V_{cb} \\ V_{td} & V_{ts} & V_{tb} \end{pmatrix}. \tag{2.4}$$

The CKM matrix depends on four parameters: Three angles and one phase, called the Kobayashi-Maskawa phase. In the particular case in which the matrix depends only on three generations of quarks, and the quarks cannot transform in other quantum states, the matrix needs to be unitary $V_{CKM}V_{CKM}^{\dagger} = 1$.

The CKM matrix can be represented in different ways, one of which is the Wolfenstein parameterization [17] defined as:

$$V_{CKM} = \begin{pmatrix} 1-\lambda^2/2 & \lambda & A\lambda^3(\rho - i\eta) \\ -\lambda & 1-\lambda^2/2 & A\lambda^2 \\ A\lambda^3(1-\rho-i\eta) & -A\lambda^2 & 1 \end{pmatrix}, \tag{2.5}$$

where A, ρ, η, and λ are real parameters defined in [17]. The unitarity of the CKM matrix imposes nine constraints. Six of these relations can be represented geometrically as unitary triangles on the complex plane. Two of these relations are related to the coupling of b-quarks, and are as follows:

$$V_{ud}V_{ub}^{*} + V_{cd}V_{cb}^{*} + V_{td}V_{tb}* = 0, \tag{2.6}$$

$$V_{us}V_{ub}^{*} + V_{cs}V_{cb}^{*} + V_{ts}V_{tb}* = 0. \tag{2.7}$$

The triangle formed from the relation in Eq. 2.6 represents the so-called "Unitarity Triangle" of the CKM matrix. Measuring the angles of the unitarity angles gives a result consistent with the SM expectation $\alpha + \beta + \gamma = (178^{11}_{-12})^{\circ}$ However, this section will focus on the relation in Eq. 2.7 which is relevant for the B_s^0 system. The equation has been normalized, so that one of the sides of the triangle is real, and equal to one dividing by $V_{cs}V_{cb}^{*}$. The angles of the triangle are defined as:

$$\begin{aligned} \beta_s &\equiv \arg(-\tfrac{V_{cs}V_{cb}^{*}}{V_{ts}V_{tb}^{*}}), \\ \alpha_s &\equiv \arg(-\tfrac{V_{ts}V_{tb}^{*}}{V_{us}V_{ub}^{*}}), \\ \gamma_s &\equiv \arg(-\tfrac{V_{us}V_{ub}^{*}}{V_{cs}V_{cb}^{*}}). \end{aligned} \tag{2.8}$$

All the triangles have the same area. The surface of the unitarity triangle is proportional to the size of CP violation present in weak interactions [18]. The B_s^0 triangle is shown in Fig. 2.1. The vertices of the triangle are (0,0), (0,1), and $(\bar{\rho}_s, \bar{\eta}_s)$, where $(\bar{\rho}_s, \bar{\eta}_s)$ are defined like:

$$\frac{V_{us}V_{ub}^*}{V_{cs}V_{cb}^*} = (\bar{\rho}_s\bar{\eta}_s);\ \bar{\rho}_s \simeq \frac{-\lambda^2}{1-\lambda^2/2}\rho, \text{ and } \bar{\eta}_s \simeq \frac{-\lambda^2}{1-\lambda^2/2}\eta. \tag{2.9}$$

The angle β_s has been measured, $\beta_s = 0.035 \pm 0.05$ [19]. However, in the B_s^0

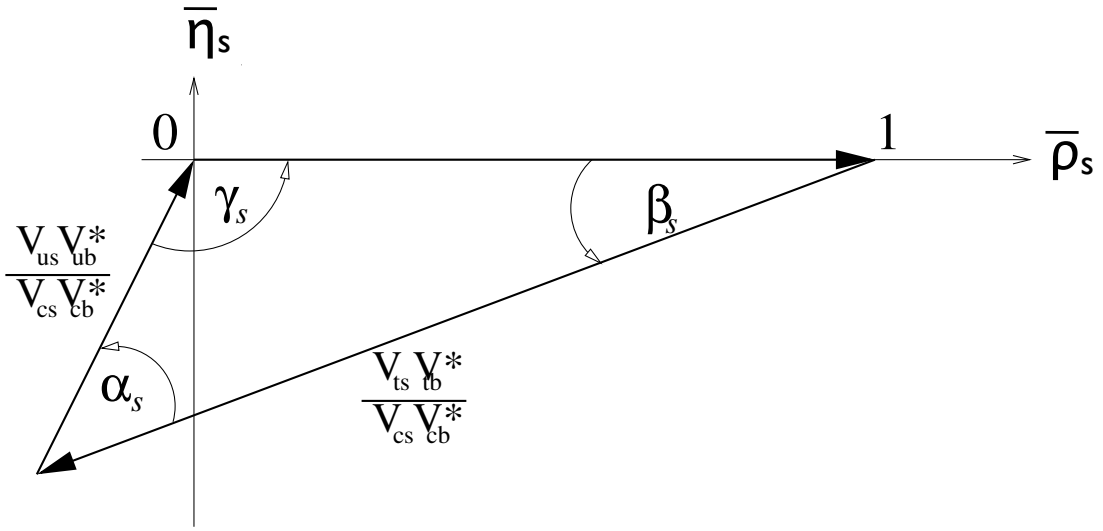

Figure 2.1: Graphical representation of the unitary triangle related to the B_s^0 meson.

unitarity triangle, the uncertainty in the value β_s is forty times the SM uncertainty. More precision measurements are needed to check if the triangle closes.

Each element of the CKM matrix of weak interactions needs to be measured from experiments. The parameters $|V_{ud}|$, $|V_{us}|$, $|V_{cd}|$, and $|V_{cs}|$ are measured through direct decays of hadrons into leptons and neutrinos. The others parameters are measured using B meson decays [12]:

- $|V_{ud}|$: Studying the superallowed $0^+ \to 0^+$ nuclear beta decays, and measuring the neutron lifetime.
- $|V_{us}|$: Measuring for example the decays $K_L^0 \to \pi e\nu$, $K_L^0 \to \pi\mu\nu$, $K_L^\pm \to \pi^0 e^\pm\nu$, $K_L^\pm \to \pi^0\mu^\pm\nu$, and $K_S^0 \to \pi e\nu$.
- $|V_{cd}|$: Using semileptonic charm decays if the theoretical form factors is available like $D \to Kl\nu$, and $D \to l\nu$.

- $|V_{cs}|$: Can be measured directly using flavor-tagged W-decay, for example $W^+ \to c\bar{s}$ decays, or from semileptonic D or leptonic D_s decays.
- $|V_{cb}|$: Measuring exclusive and inclusive semileptonic decays of B mesons to charm. For example B mesons decaying to D or D^* mesons.
- $|V_{ub}|$: Measuring for example $B \to X_u l\bar{\nu}$, where $l\bar{\nu}$ is a lepton with its corresponding neutrino, and X_u is a particle that contains a u quark like π.
- $|V_{td}|$ and $|V_{ts}|$: Needs to be measured using $B - \bar{B}$ oscillations.
- $|V_{tb}|$: Can be determined from the ratio $R = \mathcal{B}(t \to Wb)/\mathcal{B}(t \to Wq)$ being $q = b, s, d$ quarks.

The most recent values for the Wolfenstein parameters are $\lambda = 0.22535 \pm 0.00065$, $A = 0.817 \pm 0.015$, $\rho = 0.136 \pm 0.018$, and $\eta = 0.348 \pm 0.014$ [12, 20], which results in the following CKM values:

$$|V_{CKM}| = \begin{pmatrix} 0.97427 \pm 0.00015 & 0.22534 \pm 0.00065 & 0.00351^{+0.00015}_{-0.00014} \\ 0.22520 \pm 0.00065 & 0.97344 \pm 0.00016 & 0.0412^{+0.0011}_{-0.0005} \\ 0.00867^{+0.00029}_{-0.00031} & 0.0404^{+0.0011}_{-0.0005} & 0.999146^{+0.000021}_{-0.000046} \end{pmatrix}. \quad (2.10)$$

The global fit that uses all the measurement together and imposes all the SM constraints in the $\bar{\rho}_s$ vs. $\bar{\eta}_s$ plane, and includes theory predictions on the Unitarity Triangle, relevant to the B_s^0 system are shown in Fig. 2.2.

2.3 The B_s^0 meson system and the $B_s^0 - \bar{B}_s^0$ mixing

B mesons are particles formed by two quarks, one anti-bottom quark and one up, down, charm or strange quark. Each of these combinations produces a different B meson: B^+, B^0, B_c^+ and B_s^0 and their charged conjugated B^-, $\bar{B}^0$, B_c^-, $\bar{B}_s^0$ respectively. In Table 2.3 are presented the quark content of the B mesons, charge, and their masses. The B mesons have a characteristically long decay lifetime, which allows the study of their properties, and they have a large probability of particle anti-particle mixing. This dissertation focuses on the study of the B_s^0 mesons, composed by an anti b-quark, and a s-quark ($\bar{b}s$). According to the Particle Data Group the B_s^0 meson has the following characteristics [12]: Mass of 5 366.77 $\pm$ 0.24 MeV/c^2, and lifetime measured using the $B_s^0 \to J/\psi\ \phi$ decay is 1.429 $\pm$ 0.088. The branching fraction for the $B_s^0 \to J/\psi\ \phi$ decay is $(1.09^{0.28}_{0.23}) \times 10^{-3}$.

The $B_s^0 - \bar{B}_s^0$ oscillations were observed for the first time in 2006 at the CDF experiment with 1 fb^{-1} of data [23]. The B_s^0 meson can oscillate to a $\bar{B}_s^0$ and vice

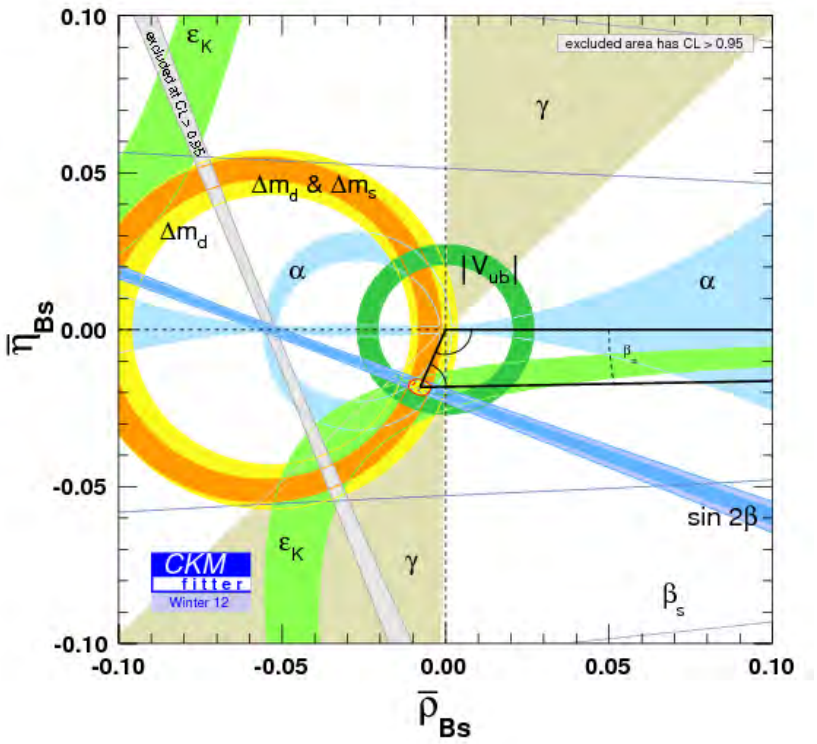

Figure 2.2: Constraints in the $(\bar{\rho}_s,\bar{\eta}_s)$ plane. The red hashed region of the global combination corresponds to 68% CL. The (almost horizontal) thin blue lines correspond to the 68% and 95% CL constraints on β_s from the combined results on $B_s^0 \to J/\psi\ \phi$ from CDF [21] and LHCb [22] obtained from [20].

Table 2.1: Properties of the B mesons:B^+, B^0, B_c^+ and B_s^0 according to PDG [12]

Particle	Anti-particle	Quark content	Charge	Mass MeV/c^2	Mean lifetime (ps)
B^+	B^-	$u\bar{b}$	+1	5 279.25 $\pm$ 0.17	1.641 $\pm$ 0.008
B^0	$\bar{B^0}$	$d\bar{b}$	0	5 279.58 $\pm$ 0.17	1.519 $\pm$ 0.007
B_s^0	$\bar{B_s^0}$	$s\bar{b}$	0	5 366.77 $\pm$ 0.24	1.497 $\pm$ 0.015
B_c^+	B_c^-	$c\bar{b}$	+1	6 277 $\pm$ 6	0.453 $\pm$ 0.041

versa, with a frequency of $\Delta m_s = 17.63 \pm 0.11$ (stat) ± 0.02 (syst) ps^{-1} [24], which is on average oscillating five times before decaying. The oscillation is given by the mass difference of the heavy (H) and the light (L) mass eigenstates. The mass eigenstates are different from the flavor eigenstates B_s^0, and $\bar{B_s^0}$. If CP violation would not be present, the mass eigenstates and the flavor eigenstates would be the same. In Figure 2.3 the two leading box Feynman diagrams of the B_s^0 mixing are shown.

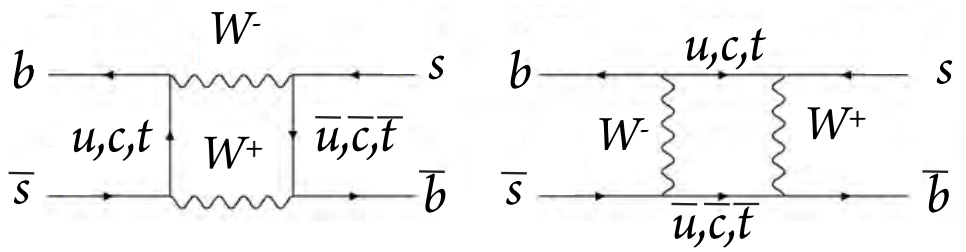

Figure 2.3: Leading box diagrams for the $B_s^0 - \bar{B}_s^0$ oscillations.

The B_s^0 meson time evolution can be written as a function of the flavor eigenstates $|B_s^0\rangle$ and $|\bar{B}_s^0\rangle$ as:

$$|\psi(t)\rangle = a(t)|B_s^0\rangle + b(t)|\bar{B}_s^0\rangle. \tag{2.11}$$

The time evolution follows the Schrödinger equation:

$$i\frac{\partial}{\partial t}|B_s^0\rangle = (M - \frac{i}{2}\Gamma)|B_s^0\rangle, \tag{2.12}$$

where M and Γ are the mass and lifetime matrices. In this equation it is required that $M = M^\dagger$ and $\Gamma = \Gamma^\dagger$ together with CPT invariance, the diagonal elements of M and Γ are the flavor conserving transitions $B_s^0 \to B_s^0$ or $\bar{B}_s^0 \to \bar{B}_s^0$, whereas the off-diagonal elements are responsible for the flavor changing transitions $B_s^0 \leftrightarrow \bar{B}_s^0$. The heavy and light mass eigenstates of the Hamiltonian are constructed like:

$$\begin{aligned} |B_s^H\rangle &= p|B_s^0\rangle - q|\bar{B}_s^0\rangle \\ |B_s^L\rangle &= p|B_s^0\rangle + q|\bar{B}_s^0\rangle. \end{aligned} \tag{2.13}$$

In case there is no CP violation, the normalization condition is $|p|^2 + |q|^2 = 1$. Using the convention that the heavy eigenstate has the largest mass, the mass difference for the mass eigenstates is represented as:

$$\Delta m_s \equiv m_s^H - m_s^L, \tag{2.14}$$

and the decay width difference is:

$$\Delta\Gamma_s \equiv \Gamma_s^L - \Gamma_s^H, \tag{2.15}$$

where $\Gamma_L \equiv 1/\tau_L$ and $\Gamma_H \equiv 1/\tau_H$, being τ_L and τ_H the mean lifetime of the two mass eigenstates. The $\Delta\Gamma_s$ value has two possible solutions, one negative and one positive. In the Standard Model $\Delta\Gamma_s$ is supposed to be positive, which means that the Heavy state is supposed to live shorter than the Light state. Recently, the LHCb experiment presented the first result where $\Delta\Gamma_s$ value is found to be positive [25].

Solving Eq. 2.12 gives that the time evolution of $|B_s^0\rangle$ or $|\bar{B_s^0}\rangle$ can be written as:

$$|B_s^0(t)\rangle = g_+(t)|B_s^0\rangle + \frac{q}{p}g_-(t)|\bar{B_s^0}\rangle, \tag{2.16}$$

$$|\bar{B_s^0}(t)\rangle = g_+(t)|\bar{B_s^0}\rangle + \frac{p}{q}g_-(t)|B_s^0\rangle, \tag{2.17}$$

where $g_\pm$ are defined as:

$$|g_\pm(t)|^2 = \frac{e^{-\Gamma_s t}}{2}[\cosh(\frac{\Delta\Gamma_s}{2}t) \pm \cos(\Delta m_s t)], \tag{2.18}$$

and $\Gamma_s \equiv (\Gamma_s^H + \Gamma_s^L)/2 = 1/\tau_{B_s^0}$, where $\tau_{B_s^0}$ is the proper decay time of the B_s^0 meson.

Finally, the $\Delta\Gamma_s$ value can be approximated to the diagonal values of the Γ matrix like [26–28]:

$$\Delta\Gamma_s = \Gamma_L^s - \Gamma_H^s = 2|\Gamma_{12}^s|\cos\phi_s, \tag{2.19}$$

where ϕ_s is the CP violating weak phase, and is defined as $\phi_s = \arg(M_{12}/\Gamma_{12})$. ϕ_s is related to the B_s^0 CKM unitarity triangle like:

$$\phi_s = -2\beta_s, \tag{2.20}$$

where β_s is defined in Eq. 2.8.

2.4 CP violation in $B_s^0 \to J/\psi\ \phi$ decays

This analysis focuses on the study and reconstruction of the B_s^0 meson decaying to the final state $J/\psi\ \phi(1020)$, where J/ψ decays into two muons of opposite charge $\mu^+\mu^-$, and the $\phi(1020)$ decays into two kaons of opposite charge K^+K^-. The B_s^0 meson can decay in two ways: The B_s^0 can oscillate to $\bar{B_s^0}$ and then decay to the final state; Analogously, the $\bar{B_s^0}$ meson can decay oscillating to the B_s^0 mesons, or directly to the final state.

In the $B_s^0 \to J/\psi\ \phi$ decay, the CP violation term arises from the interference between the mixing and the direct decay. Figure 2.4 shows the Feynman diagram of the direct decay.

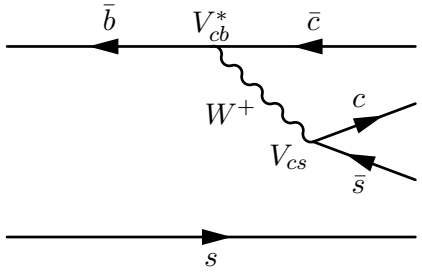

Figure 2.4: Feynman diagram of the $B_s^0 \to J/\psi\ \phi$ decay.

In the Standard Model, the CP eigenstates can be associated to the mass eigenstates in the following way [29]:

$$\begin{aligned} |B_s^L\rangle &\simeq |B_{even}^0\rangle \\ |B_s^H\rangle &\simeq |B_{odd}^0\rangle, \end{aligned} \tag{2.21}$$

so that the B_s^0 meson is a composition of CP even and CP odd states.

Since the B_s^0 meson is a pseudo scalar, and J/ψ and $\phi(1020)$ are vector mesons, the orbital angular momentum of the two decay products can have the values $L =$ 0, 1, and 2. In the final state three types of polarization exist: The longitudinal polarization, with amplitude $A_0(0)$ for $L = 0$, which is CP even; the perpendicular polarization, with amplitude $A_\perp(0)$ for $L = 1$, which is CP odd; and the parallel polarization, with amplitude $A_{||}(0)$ for $L = 2$, which is CP even. To determine the amplitudes of the polarization, the CP violating weak phase, and the $\Delta\Gamma_s$ value, it is necessary to separate both CP contributions. Measuring the angular distributions of the final decay products, the CP eigenstates can be statistically disentangled.

The differential decay rate as a function of the proper decay time t can be represented as function of various parameters:

$$\frac{d^4\Gamma(B_s(t))}{d\Theta dt} = f(\Theta, \alpha, t) = \sum_{i=1}^{6} O_i(\alpha, t).g_i(\Theta), \tag{2.22}$$

where O_i are kinematics-independent observables, g_i are the angular distributions, α denotes a set of physics parameters of interest (Γ_s, $|\Delta\Gamma_s|$, $|A_0|^2$, $|A_{||}|^2$, $|A_\perp|^2$, and strong phases $\delta_{||}$ and $\delta_\perp$), and Θ are the physical angles that describe the decay. By fitting the time dependent decay rate it is feasible to extract the parameters of interest.

In this thesis an untagged analysis is performed, which implies that no distinction is made between the B_s^0 and $\bar{B_s^0}$ mesons. The time evolution of the observables is given by a bi-linear combination of the decay products polarization amplitudes, and the observables are described using the following equations [30, 31]:

$$\begin{aligned}
O_1 &= |A_0(t)|^2 \\
&= |A_0(0)|^2 e^{-\Gamma_s t}[\cosh(\Delta\Gamma_s t/2) - |\cos\phi_s| \sinh(|\Delta\Gamma_s|t/2)], \\
O_2 &= |A_{||}(t)|^2 \\
&= |A_{||}(0)|^2 e^{-\Gamma_s t}[\cosh(\Delta\Gamma_s t/2) - |\cos\phi_s| \sinh(|\Delta\Gamma_s|t/2)], \\
O_3 &= |A_\perp(t)|^2 \\
&= |A_\perp(0)|^2 e^{-\Gamma_s t}[\cosh(\Delta\Gamma_s t/2) + |\cos\phi_s| \sinh(|\Delta\Gamma_s|t/2)], \\
O_4 &= Im(A_{||}^*(t)A_\perp(t)) \\
&= |A_{||}(0)||A_\perp(0)| e^{-\Gamma_s t}[\cos(\delta_\perp - \delta_{||}) \sin\phi_s \sinh(|\Delta\Gamma_s|t/2)], \\
O_5 &= Re(A_0^*(t)A_{||}(t)) \\
&= |A_0(0)||A_{||}(0)| \cos(\delta_{||} - \delta_0) e^{-\Gamma_s t}[\cosh(\Delta\Gamma_s t/2) \\
&\quad -|\cos\phi_s| \sinh(|\Delta\Gamma_s|t/2)], \\
O_6 &= Im(A_0^*(t)A_\perp(t)) \\
&= |A_0(0)||A_\perp(0)| e^{-\Gamma_s t}[-\cos(\delta_\perp - \delta_0) \sin\phi_s \sinh(|\Delta\Gamma_s|t/2)].
\end{aligned} \tag{2.23}$$

This analysis assumes a value of zero for ϕ_s, but other values of ϕ_s have been considered to account for systematic uncertainties that may arise from this assumption. The amplitude constraints at time $t = 0$ is $|A_0(0)|^2 + |A_{||}(0)|^2 + |A_\perp(0)|^2 = 1$. In addition, the two strong phases are denoted by $\delta_{||}$ =arg$(A_{||}(0)A_0^*(0))$ and $\delta_\perp$ =arg$(A_\perp A_0^*)$, and the δ_0 phase is set to zero by convention.

The angles $\Theta = (\theta, \psi, \varphi)$ are defined in the transversity basis [29] to describe the topology of the decay $B_s^0 \to J/\psi\ \phi$, as shown in Fig. 2.5.

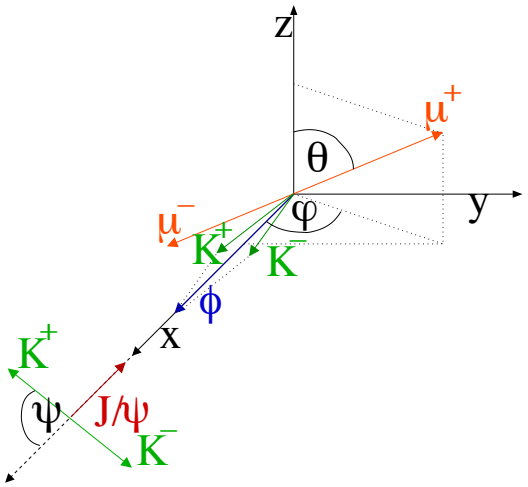

Figure 2.5: Diagram of the physical angles that describe the $B_s^0 \to J/\psi\ \phi$ decay. The angles θ and φ are defined in the J/ψ rest frame, and the angle ψ is defined in the $\phi(1020)$ meson frame.

The angles θ and φ are the polar and azimuthal angles of the μ^+ in the rest frame of the J/ψ respectively, where the x-axis is defined by the direction of the B_s^0, and the xy-plane by the decay plane of the $\phi \to K^+K^-$. The helicity angle ψ is the angle of the K^+ in the $\phi(1020)$ rest frame with respect to the negative B_s^0 flight direction. The set of angles Θ can be defined as a function of the vector momenta of the muons and the kaons, as follows:

$$\begin{aligned} \sin\theta\cos\varphi &= \mathbf{p}_{\mu^+} \cdot \mathbf{x} \\ \sin\theta\sin\varphi &= \mathbf{p}_{\mu^+} \cdot \mathbf{y} \\ \cos\theta &= \mathbf{p}_{\mu^+} \cdot \mathbf{z} \\ \cos\psi &= -\mathbf{p'}_{K^+} \cdot \mathbf{p'}_{J/\psi}, \end{aligned} \tag{2.24}$$

where $\mathbf{p}$ is the momentum measured in the J/ψ rest frame, and the $\mathbf{p'}$ is measured in the rest frame of the $\phi(1020)$.

The individual angular distributions, from Eq. 2.22, are given by the following equations:

$$
\begin{aligned}
g_1 &= 2\cos^2(\psi)(1-\sin^2(\theta)\cos^2(\varphi)),\\
g_2 &= \sin^2(\psi)(1-\sin^2(\theta)\sin^2(\varphi)),\\
g_3 &= \sin^2(\psi)\sin^2(\theta),\\
g_4 &= -\sin^2(\psi)\sin^2(2\theta)\sin(\varphi),\\
g_5 &= \frac{1}{\sqrt{2}}\sin(2\psi)\sin^2(\theta)\sin(2\varphi),\\
g_6 &= \frac{1}{\sqrt{2}}\sin(2\psi)\sin(2\theta)\sin(\varphi).
\end{aligned}
\tag{2.25}
$$

The physical parameters $|\Delta\Gamma_s|$ and ϕ_s values, can be extracted when an angular analysis is performed to the $B_s^0 \to J/\psi\ \phi$ channel. This analysis does not measure the signed of the $\Delta\Gamma_s$ value, however, by simplicity and knowing the value of $\Delta\Gamma_s$ is positive [25] this thesis uses $\Delta\Gamma_s$ without the absolute value.

As the CP violation phase in the Standard Model is small, $\phi_s{=}{-}0.0363^{+0.0016}_{-0.0015}$ rad [32, 33], this implies that $\Delta\Gamma_s \simeq 2|\Gamma^s_{12}|$. The Standard Model value for $\Delta\Gamma_s$ is:

$$\Delta\Gamma_s^{SM} \simeq 2|\Gamma_{12}| = (0.087 \pm 0.021)\text{ps}^{-1}, \tag{2.26}$$

where $\Delta\Gamma_s^{SM}/\Gamma_s \simeq 2|\Gamma_{12}|/\Gamma_s = 0.133 \pm 0.032$, and the oscillation frequency of the B_s^0 mesons is $\Delta m_s^{SM} = (17.3 \pm 2.6)\text{ps}^{-1}$ [26].

2.5 Results from other experiments

During the last ten years, the Tevatron accelerator produced most of the results on the CP asymmetry of the $B_s^0 \to J/\psi\ \phi$ channel. However, with the start of the LHC, three of the four detectors are producing interesting B physics results. The most recent and precise result of B_s^0 oscillation comes from the LHCb experiment, using 36 pb^{-1} of data at $\sqrt{s} = 7$ TeV, according to which the $B_s^0 - \bar{B}_s^0$ oscillation frequency is $\Delta m_s = 17 \pm 0.08$ ps^{-1} [24]. The world average value of the mixing, which takes into account all the available results, is $\Delta m_s = 17.719 \pm 0.036(\text{stat}) \pm 0.023(\text{syst})$ ps^{-1} [12].

The latest results presented from Tevatron (CDF and D0) were obtained at $\sqrt{s} =$ 1.96 TeV. The CDF experiment accumulated a luminosity of 9.6 fb^{-1} of data, and the D0 experiment a luminosity of 8 fb^{-1}. From the LHC accelerator, the LHCb experiment presented the results using a tagged analysis. LHCb obtained the first observation of $\Delta\Gamma_s$ different from zero and is currently the most precise value for $\Delta\Gamma_s$ and the CP violation phase ϕ_s [25]. Additionally, the ATLAS detector published an

untagged analysis of $B_s^0 \to J/\psi\ \phi$ [34]. Table 2.2 summarizes the aforementioned results from the different experiment, including the results shown in this thesis which are the current public result from the CMS collaboration.

Table 2.2: Summary of the $\Delta\Gamma_s$ and $\Delta\Gamma_s/\Gamma_s$ from the D0 and CDF experiments from the Tevatron accelerator, and LHCb, and ATLAS from the LHC accelerator.

Detector	Ref.	$\Delta\Gamma_s$ (ps^{-1})	Γ_s (ps^{-1})	$\Delta\Gamma_s$ /Γ_s
D0	[35]	$0.163^{+0.065}_{-0.064}$	$0.693^{+0.018}_{-0.017}$	0.235
CDF	[36]	0.068 ± 0.026 (stat.) ± 0.009 (syst.)	0.654 ± 0.008 (stat.) ± 0.004 (syst.)	0.104 ± 0.040
LHCb	[19]	0.100 ± 0.016 (stat.) ± 0.003 (syst.)	0.663 ± 0.005 (stat.) ± 0.006 (syst.)	0.151 ± 0.024
ATLAS	[34]	0.053 ± 0.021 (stat.) ± 0.010 (syst.)	0.677 ± 0.007 (stat.) ± 0.004 (syst.)	0.078 ± 0.031

2.6 Analysis strategy

To perform the measurement of $\Delta\Gamma_s$ in the $B_s^0 \to J/\psi\ \phi$ decay, a number of steps need to be done. The first task is to reconstruct the B_s^0 meson through the decay products, J/ψ decaying to two muons and $\phi(1020)$ decaying to two kaons. The chosen analysis approach uses a trigger that selects events with two muons. A sophisticated procedure is applied to select four tracks, in order to form candidates of B_s^0 mesons.

The observables of interest in this analysis are the decay length and invariant mass of the $\mu^+\mu^-K^+K^-$ system, and a set of three angles $\Theta = (\theta, \psi, \varphi)$ that describe the topology of the decay $B_s^0 \to J/\psi\ \phi$, described in Eq. 2.24.

Finally, the physical parameters of interest (α), are obtained from a Maximum Likelihood Fit on a probability density function (PDF) that describes the properties of the signal and the background in data.

Chapter 3

The Compact Muon Solenoid experiment

The Large Hadron Collider (LHC) [2] is a two-ring super-conducting accelerator located at CERN (Conseil Européen pour la Recherche Nucléaire), in Geneva, Switzerland. It is a circular collider, with a circumference of 26.7 km, designed to accelerate protons or heavy ions. Two proton beams move in opposite directions and collide at four points (called the interaction points) at 7 TeV of center of mass energy (8 TeV in 2012), and at a luminosity of 10^{33} $\mathrm{cm}^{-2}\mathrm{s}^{-1}$. The LHC has been designed to study physics at the TeV energy scale, having as a main motivation the explanation of the nature of electroweak symmetry breaking, and the discovery of new physics beyond the Standard Model.

The CMS detector is located in one of the four interaction points present in the LHC ring. It is a general-purpose detector with the idea of covering the broadest possible range of physics topics. The CMS collaboration consists of more than four thousand members from 179 institutions and 41 countries.

This chapter introduces the LHC complex facility in Section 3.1. Then, a short overview of the Compact Muon Solenoid (CMS) detector is given in Section 3.3. The trigger system is described in Section 3.4. The event reconstruction is discussed in Section 3.5, and the CMS detector alignment procedures in Section 3.6. Finally, the data sample used for this dissertation is presented in detail in Section 3.2.

3.1 The Large Hadron Collider

The LHC acronym stands for Large Hadron Collider. The term Large refers to its size of approximately 27 km in circumference, Hadron refers to the protons or ions being accelerated, and Collider indicates that the protons (ions) travel in two beams moving in opposite directions and collide at four intersection points of the machine. The machine has been designed for colliding proton proton with a centre-of-mass energy of 14 TeV and a luminosity $10^{34}\text{cm}^{-2}\text{s}^{-1}$.

The LHC machine forms part of the accelerator complex at CERN. The complex is a chain of several machines, where the particle beams are successively accelerated and finally injected to the LHC. First, the protons are extracted from a hydrogen bottle and injected into the initial linear accelerator (LINAC2), where they are accelerated to 50 MeV. Then, the energy of the proton is risen up to 1.4 GeV in the Proton Synchrotron Booster (Booster), and injected into the Proton Synchrotron (PS) where their energy reaches 25 GeV. Afterwards, the protons are injected to the Super Proton Synchrotron (SPS) where they are accelerated to 450 GeV. Finally, the protons are injected into the LHC (both in a clockwise and counterclockwise direction), and accelerated to their final energy which in 2012 reached 4 TeV. The full LHC complex scheme can be seen in Figure 3.1.

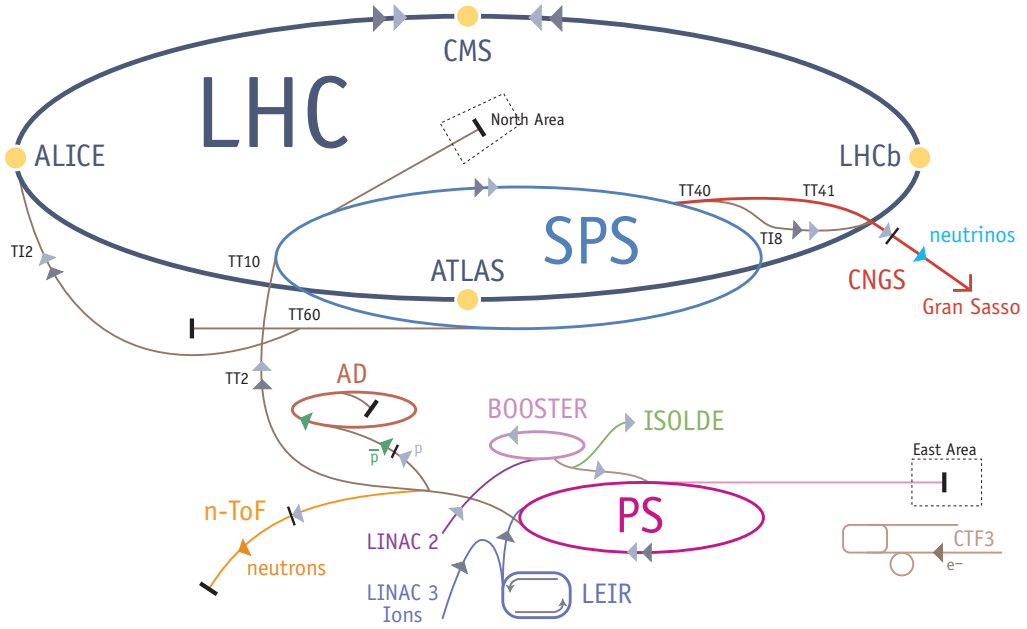

Figure 3.1: Layout of the LHC accelerator complex. The main experiments (CMS, ATLAS, LHCb and ALICE) are located at the four interactions points (taken from [37]).

The most relevant machine parameters that describe the collider are the center

of mass energy ($\sqrt{s}$), the instantaneous luminosity ($\mathcal{L}$), and the number of proton bunches per beam. The instantaneous luminosity is calculated according to the following equation [2]:

$$\mathcal{L} = \frac{\gamma N_p^2 f k_B}{4\pi\epsilon_n \beta^*} F, \tag{3.1}$$

where γ is the relativistic Lorentz factor, N_p is the number of protons per bunch, f is the revolution frequency of the machine, k_B is the number of bunches, ϵ_n is the normalized transverse beam emittance, β^* is the betatron function at the collision point, and F is the geometric luminosity reduction factor due to the crossing angle. At full luminosity during 2011, the LHC is running with a spacing of 50 ns between bunches (approximately 15 m), corresponding to a collision frequency of 20 MHz.

Four experiments are installed in each of the four interaction points of the LHC. Two experiments are general purpose detectors: CMS (Compact Muon Solenoid) and ATLAS (A Toroidal LHC AparatuS). Additionally, there are two specialized detectors: LHCb is devoted to the study of CP violation and weak interactions in the B system, while ALICE (A Large Ion Collider Experiment) is dedicated to the study of heavy ion collisions. The work of this thesis is done within the CMS collaboration. In the next section the CMS general layout is explained.

3.2 Luminosity and data collection

The LHC started operations on the 10th of September 2008, with first beams at the injection energy of 450 GeV. Unfortunately, nine days later an accident occurred while raising currents in the magnets. Consequently, the plans for the LHC were changed. It was decided that LHC would provide proton beams of 3.5 TeV for the 2010 and 2011 data taking. Due to the good performance of the LHC machine, during 2012 the LHC has been providing proton beams of 4 TeV. Figure 3.2 shows the cumulative luminosity delivered to CMS during the operations of 2010, 2011, and 2012.

The 30th of March 2010, first collisions at 7 TeV center of mass energy were produced. During 2010, the peak luminosity was 2.1 $\times 10^{32}$ cm ^{2}s^{-1}. The performance of the machine exceeded the expectations, and at the end of 2011 the peak luminosity reached 3.6 $\times 10^{33}$ cm ^{2}s^{-1}. For the 2012 data taking period, the LHC machine ran at 8 TeV center of mass, reaching an instantaneous peak luminosity of 3.9 $\times 10^{33}$ cm ^{2}s^{-1}.

This dissertation focuses on the data taken with beams with 10^{11} proton bunches, between 150 and 50 ns apart, providing proton-proton collisions with a center of mass

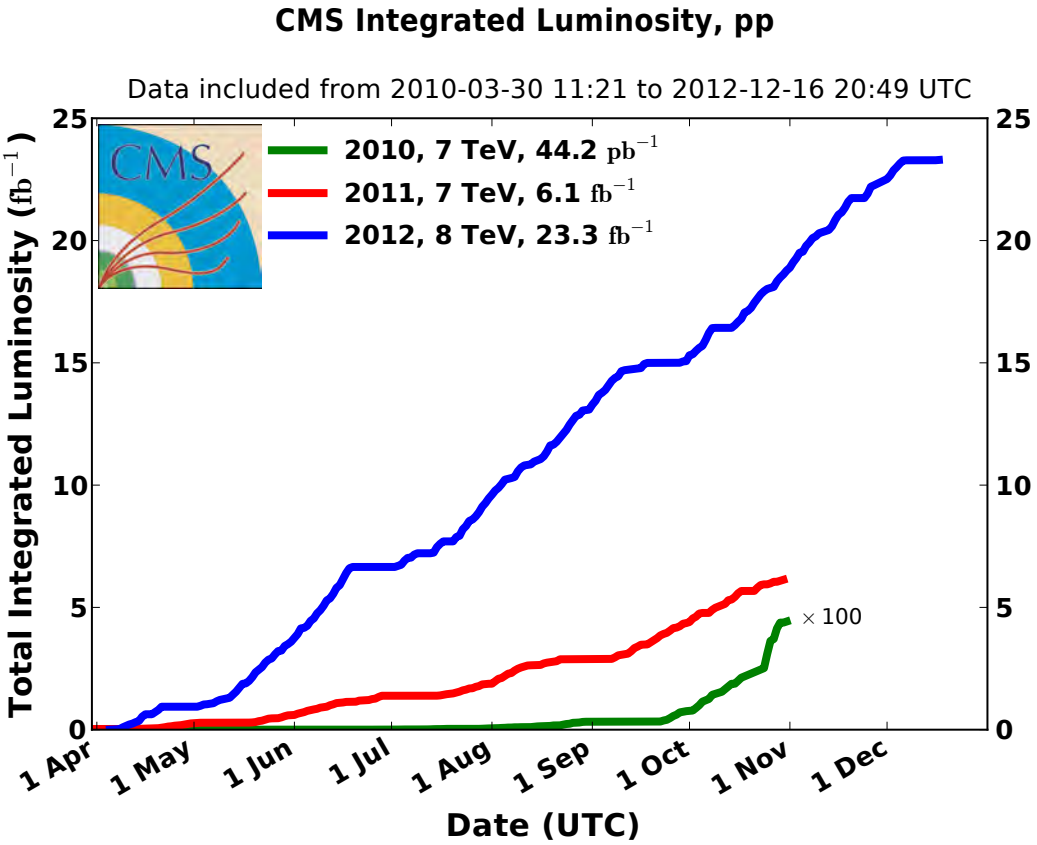

Figure 3.2: Total cumulative integrated luminosity versus day delivered to CMS with proton-proton collisions during data taking of 2010 (green), 2011 (red), and 2012 (blue) (Courtesy of CMS).

energy of 7 TeV. This data was gathered during the 2011 data taking period, between February and October 2011.

The CMS online luminosity measurement calculates the luminosity measuring the signal from the Hadron Forward Calorimeter. Two methods exist for performing this measurement. The first one is called "zero counting" and it uses the mean number of interactions per bunch crossing. The second method uses a linear relation on the average transverse energy and the luminosity. The luminosity is calibrated using a Van der Meer scan [56].

The total recorded luminosity in 2011 was $\mathcal{L}$= 5.56 fb^{-1}, which is 91 % of the delivered luminosity. In this analysis $\mathcal{L}$= 5.0 $\pm$ 0.1 fb^{-1} of good quality data were used.

3.3 CMS general layout

CMS is a multi-purpose detector, designed to cover the full physics potential of the LHC. The CMS detector is 21.6 m long, it has a diameter of 14.6 m, and weighs 12500 tons. The CMS detector is constructed around a superconductive solenoid coil, with a magnetic field of 3.8 T.

Figure 3.3 shows a schematic view of the detector, where the different sub-detectors are shown. The one closer to the interaction point is the silicon tracker, which is use to reconstruct the trajectories of the particles. The tracker is surrounded by the electromagnetic and the hadronic calorimeters, which measure the energy of particles. Except for the hadron forward calorimeters, all the sub-detectors named are located inside the super-conductive coil. Lastly, the muon system is used to identify and measure the momentum of the muons, combining with the information from the tracker and the calorimeters.

In order to fulfill the LHC physics goals, the detector is designed to have a good muon identification and a muon resolution varying from few GeV to the TeV scale, as well as an inner tracker with good resolution for determining the momentum of charged particles. The tracker also allows for a precise vertex reconstruction which is crucial to identify long-lived particles like B mesons.

Apart from the high resolution of the tracking and muon devices, the large solenoidal magnetic field of 3.8 T allows to measure the momenta of charged particles with great precision due to the large curvature of the particle trajectories.

3.3.1 CMS coordinate system

The CMS coordinate system is the reference for all the measurements in the detector. The origin of this coordinate system is based on the nominal collision point inside the detector. The z-axis is directed along the beam direction. The x-axis is oriented in the horizontal plane toward the center of the LHC ring and the y-axis is defined to point upward.

A polar coordinate system is also defined. The azimuthal angle of this system, ϕ, is measured starting from the x-axis and moving into the xy-plane in the range $[0, 2\pi]$. The radial coordinate in this plane is denoted by r. The polar angle θ, which is the angle with respect to the z-axis, is in the range $[0, \pi]$.

The pseudo-rapidity is defined as:

$$\eta = -\ln\left(\tan\frac{\theta}{2}\right). \tag{3.2}$$

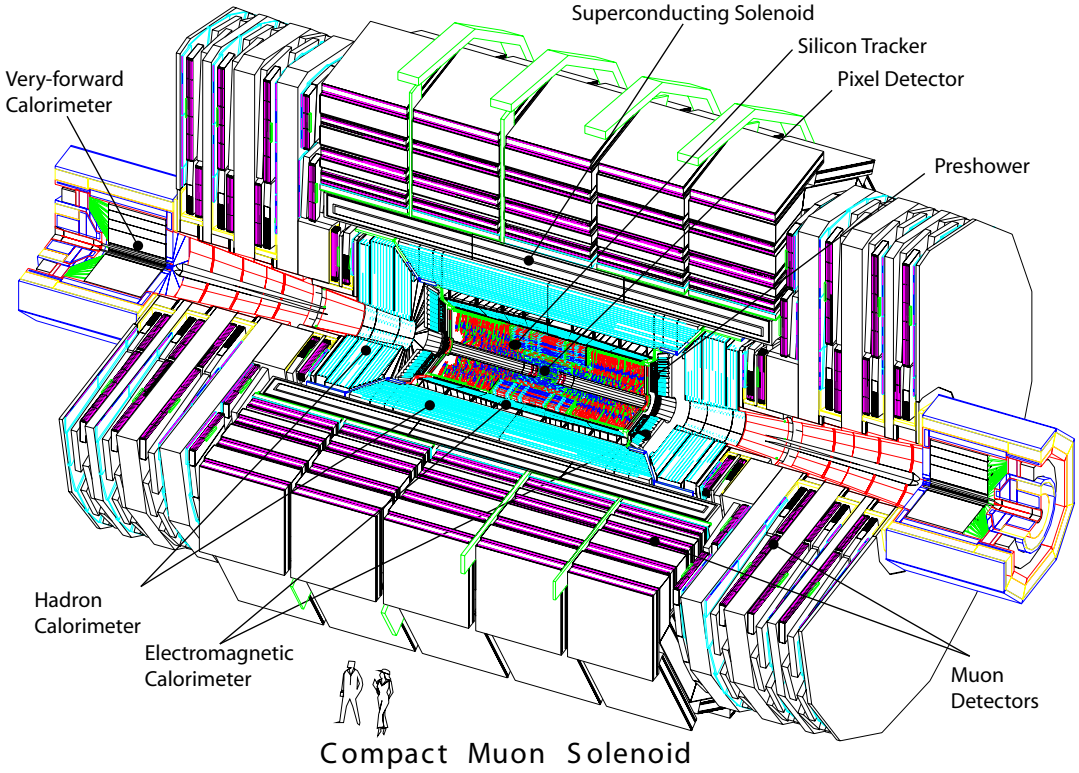

Figure 3.3: CMS schematic view (courtesy of CMS).

Distance in the pseudorapidity-azimuthal space is defined as $\Delta R = \sqrt{\Delta\eta^2 + \Delta\phi^2}$. The energy and momentum measured in the plane transverse to the beam are called E_T and p_T, respectively.

3.3.2 Inner tracking system

The tracking system [38–40] is the innermost component of the CMS detector, and one of the main detectors used for the analysis presented in this thesis. Its role is to provide precise spatial measurements that are used for the reconstruction of charged particles near the interaction point. The tracking system is an essential detector for the reconstruction of primary and secondary vertices, and for the reconstruction of long-lived particles, like B_s^0 mesons.

The CMS tracker has a total area of 200 m^2 of active silicon detectors. It is divided into the pixel silicon detector and the silicon strip detector. The pixel detector covers a region around the interaction point in a radius of 4 cm to 15 cm from the interaction point, while the silicon micro-strip detector covers a radial range of 20 cm to 120 cm. Figure 3.4 shows a schematic view of the pixel detector.

Several requirements were considered while designing the tracker. The tracker

should operate in a high radiation environment as it is close to the beam pipe. The trajectories of all the traversing particles should be measured with high precision in order to calculate the momenta of the particles and identify the charge with the curvature of the tracks. Finally, the material budget needed to be as small as possible in order to reduce effects like multiple scattering, bremsstrahlung, photon conversions and nuclear interactions.

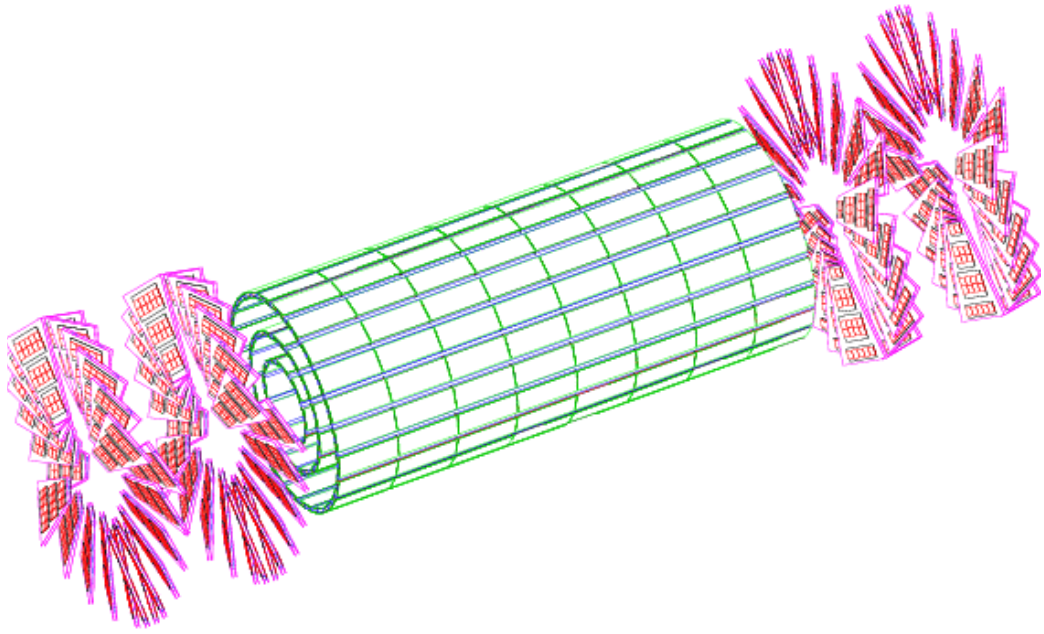

Figure 3.4: Schematic view of the pixel detector, showing the three barrel layers and the four end-cap disks (courtesy of CMS).

The pixel detector has a length of 53 cm, and consists of three barrel layers (BPIX), and two end-caps (FPIX) on each side of the detector. The innermost barrel layer is located at a radius of 4.0 cm, the second at 7.2 cm and the third layer at 11 cm. The two end disks are located along the beam pipe at z = $\pm$ 34.5 cm and z = $\pm$ 46.5 cm. The end-caps extend from 6 cm to 15 cm in radius. The pixel has 1440 silicon sensor modules with a total of 66 million readout channels [40]. The pixel size is 100$\times$150 μm, and every pixel measures an analog pulse that is analyzed in the readout system. The pixels have a square shape in order to have the most similar tracking resolution in the $r - \phi$ and z direction, which allows a good 3-dimensional vertex reconstruction. The need for a material with high radiation tolerance motivated the use of n-implants introduced into a high resistance n-substrate.

The silicon strip tracker (SST) [41], consists of four subsystems: tracker inner barrel (TIB), tracker outer barrel (TOB), tracker inner disk (TID) and tracker end-caps (TEC). Figure 3.5 shows a schematic view of the silicon strip tracker and the

pixel detector. The SST is 5.5 m long and 2.4 m in diameter, covering a total area of 198 m^2. It is formed by 15148 detector modules which include 9.3 million detector channels. The sensors are single sided p-on-n type silicon micro-strips.

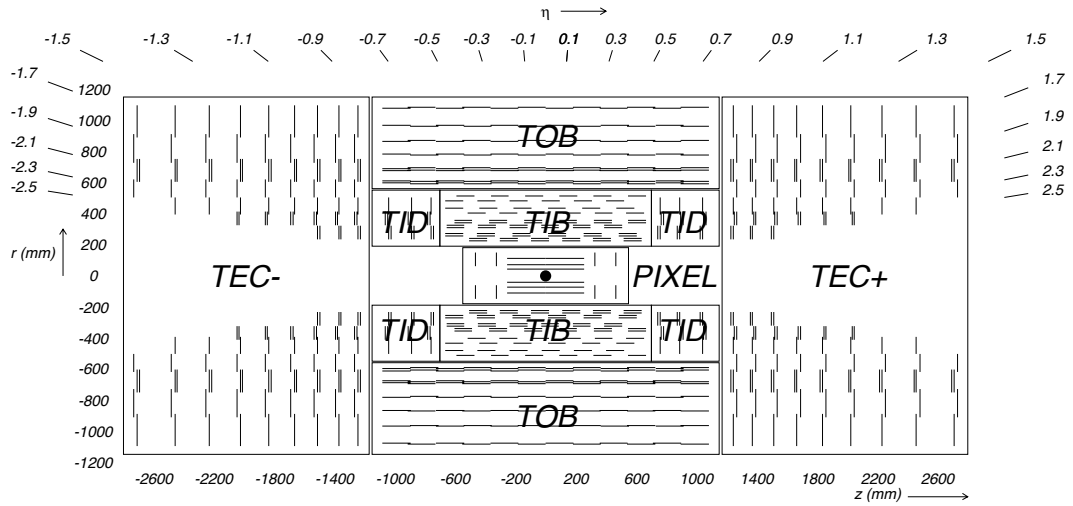

Figure 3.5: CMS schematic view of the CMS tracker. Each type of line represents a detector module. Double lines show the double-sided modules [42].

The TIB detector is formed of four layers and extends to $|z| < 65$ cm. It uses silicon sensors with thickness of 320 μm and a strip pitch that varies from 80 to 120 μm. The TOB detector is made of six layers with a half length $|z| < 110$ cm. It has silicon sensors of 500 μm thickness. The strip pitches go from 120 to 180 μm.

The end-caps are divided in TEC and TID. Each TEC and TID has nine disks, in the range of $120 < |z| < 280$ cm. The TID contains three small disks that fill the space between TIB and TEC. The TEC and TID are organized in rings, which are centered around the beam pipe. The two innermost rings of TID and the three innermost disks of TEC are "stereo" modules. Table 3.1 summarizes the different types of detector of the silicon tracker.

3.3.3 Calorimeters

The CMS calorimeter is a sampling calorimeter, made of layers of absorbing material and scintillators to measure the energy loss of particles transversing it. The electromagnetic calorimeter (ECAL) absorbs the 'lighter' charged particles, like the electrons, positrons and photons. The hadron calorimeter (HCAL) absorbs the 'heavier' neutral or charged hadrons, like protons and neutrons.

The ECAL is organized in two regions: barrel(s) and end-caps. The ECAL is made of 61 200 lead tungstate ($PbWO_4$) crystals in the central barrel, and 7 324 crystals

Part	number of detectors	thickness (μm)	mean pitch (μm)
TIB	2 724	320	81/118
TOB	5 208	500	81/183
TID	816	320	97/128/143
TEC	2 512	320	96/126/128/143

Table 3.1: Distribution of the modules in the silicon tracker.

in each of the two end-caps. The crystals have short radiation lengths (X_0=0.89 cm) and fast response (80% of the light is emitted in 25 ns).

The HCAL goal is to measure the hadronic part of the jets, which in turn are used to derive the MET[1]. The MET is derived from all the measurements in the event, muons, electrons, jets (which are constructed from the measurements in the ECAL, HCAL and the tracker). There is an additional layer of scintillators, named hadron outer, located between the solenoid and the muon chambers. The absorber material is made of brass, which has a short interaction length and is non-magnetic. The hadron outer covers the pseudorapidity region of $-1.26 < |\eta| < 1.26$, while the hadron barrel (HB) covers the pseudorapidity region of $-1.4 < |\eta| < 1.4$.

3.3.4 Muon system

CMS has been optimized to reconstruct muons with high resolution. The muon system is the most important detector together with the tracker, in the analysis of this thesis. Figure 3.6 shows a schematic view of the muon system.

Three types of gaseous detectors are used: Drift Tubes (DT), Cathode Strip Chambers (CSC) and Resistive Plate Chambers (RPC). The selection of different technologies is motivated by the large surface to be covered and the different radiation environments. The DT covers the barrel region ($|\eta| < 1.2$) and the CSC extends the coverage up to ($|\eta| < 2.4$). Both systems are complemented by the RPC which is used to ensure the performance in conditions with high event rates. The fast response of the RPCs gives a resolutions of 3 ns, and thus it is possible to match a muon track with the specific bunch crossing. In total, there are 250 DT chambers, 540 CSC, and 610 RPC. The momentum of the muons, in the muon system, is measured by the

[1]Missing transverse energy is the energy not detected by the detector, but that is expected due to the conservation of energy and momentum in the transverse plane to the beam axis. For example, missing energy could be produced by the existence of a neutrino in the decay.

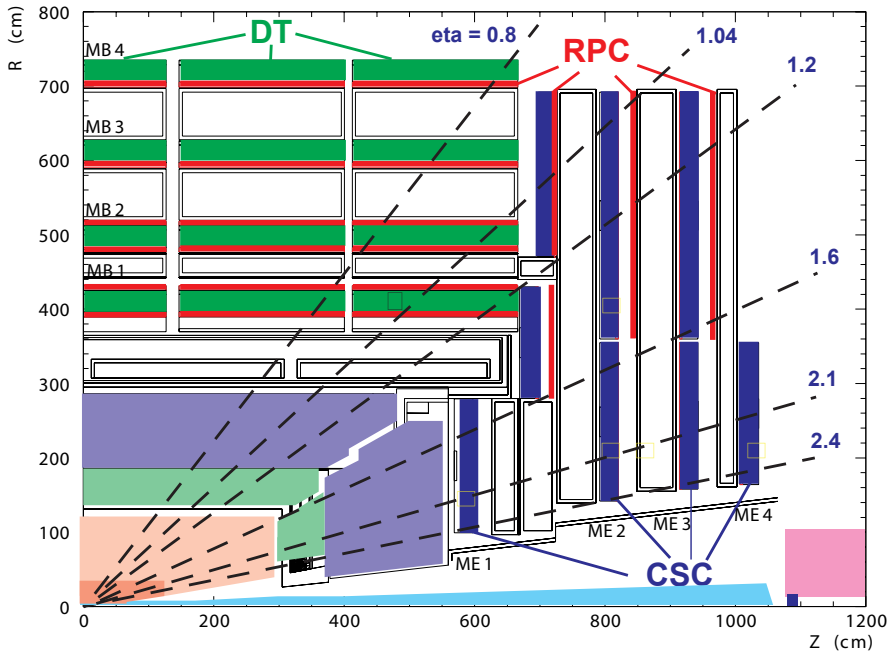

Figure 3.6: CMS schematic view of the muon system (courtesy of CMS).

muon bending angle at the exit of the 3.8 T coil, considering the interaction point as the origin of the muon.

3.4 Trigger system

During the 2011 data taking period, a peak luminosity of 3.6×10^{33} cm$^{-2}s^{-1}$ was achieved, with collisions every 50 ns. Such a rate implies that the bunches pass each of the collision points in the LHC 20 million times per second. Thus, it is not possible to write all the event data on tape. Online selections are applied to ensure that only events with interesting physics objects and topologies are selected, reducing the rate from 20 MHz to few hundreds of Hz.

The CMS trigger system is designed to cope with high luminosity and interaction rates. The trigger system reduces the data in two steps called Level-1 (L1), and High Level Trigger (HLT). The L1 trigger consists of custom-designed programmable electronics which apply online selections to reduce the data to 100 kHz, while the HLT consists of software algorithms running on a PC-farm[2] to reduce the data to hundreds of Hz.

The L1 works in three steps. First, the local trigger uses the energy deposited on the calorimeters or in the segmented data from the muon chambers and calorimeters

[2]Set of computers clustered, connected that can be viewed as a single system.

to trigger. Second, the regional trigger selects objects such as electrons and muons. Third, the global trigger takes the final decisions based on these objects. During this time, the data is stored in the detector front-end electronics waiting for the decision of the L1 trigger to build clusters in the calorimeters and segments in the muon chambers. Only then the accepted data is stored for further analysis. The L1 trigger responds within 3.2 μs in order to reduce the amount of data stored in the front-end electronics.

The HLT algorithm uses similar software that the one used for the offline reconstruction of events. The idea is to perform a more refined selection based on the object (electrons, muons, photons and other quantities) defined by the L1 trigger. The HLT menu consist of different decision algorithms, called paths, depending on the specification of the different offline analyses. The mean processing time is 100 ns per event.

The triggers bandwidth needs to be shared among the hundreds of different analyses at CMS. Only a percentage of the full bandwidth is assigned to the B-physics program, approximately 14 Hz. Given the limited bandwidth size, the B-physics coordination developed several paths, aimed for specific channels. The specific trigger used for the $B_s^0 \to J/\psi\ \phi$ analysis is explained in Section 4.3.

3.5 Particle reconstruction

In order to reconstruct an event, all the particles produced need to be tracked and characterized. When the particles cross the different sub-detectors they interact with its material. Depending on the type of particle, a characteristic signature is left. Figure 3.7 shows the trace left by different particles (electron, photon, neutral hadrons, charged hadrons, and muon) when traversing the sub-detectors. In the case of $B_s^0 \to J/\psi\ \phi$, the particles that need to be reconstructed are two muons and two kaons with opposite charge.

3.5.1 Tracking reconstruction

When charged particles traverse the tracking system, their trajectories are affected by the magnetic field. Knowing the strength of the magnetic field with precision allows for an estimate of the particle momentum, and charge sign by measuring the track curvature of the particle.

The track reconstruction is performed using a combinatorial track finder (CTF) algorithm, based on the Kalman filter algorithm [43]. The full reconstruction is done in three steps. The first step of the tracking, the seeding, is performed using pixel hits.

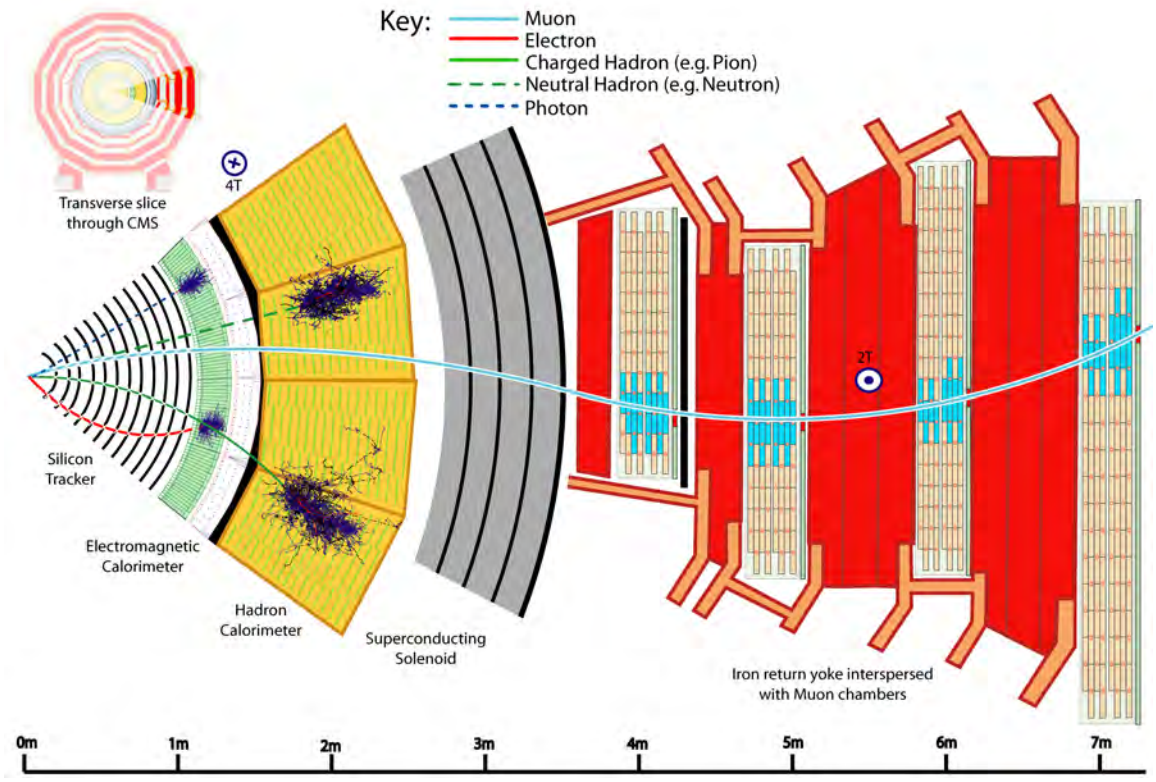

Figure 3.7: Schematic view of a transverse slice of the CMS detector. The track left by five types of particles when traversing the detector can be seen (courtesy of CMS).

Using two or three pixel hits it is possible to reconstruct the track candidates [44]. The second step uses a Kalman filter pattern recognition method, which propagates the track candidates through the tracker layers taking into account the magnetic field direction, strength and multiple scattering. The final step is to refit the tracks with a Kalman filter including all the hits, and then to use another filter to fit the tracks from the outermost layer to the one closer to the beam pipe.

3.5.2 Muon reconstruction

The muon reconstruction uses information from the reconstructed tracks in the muon chambers and in the tracker. The muon reconstruction is performed with two techniques: the "standalone", and the "global reconstruction".

The standalone reconstruction uses the information from the muon detectors. It starts with the track segments inside the muon chambers and reconstructs a track muon candidate trajectory applying a Kalman filter technique. It then uses the beam spot information to constrain the trajectory formed in the muon system.

The "global reconstruction" is performed combining the information from the silicon tracker and muon detectors only. The trajectory from the tracker is extrapolated

to the muon chambers. If the trajectory of the tracker candidate coincides with a standalone muon track, the full track is refitted and the final track is considered a "global" muon track.

3.5.3 Primary vertex reconstruction

The primary vertex reconstruction uses all tracks from the pixel detector. The tracks are selected based on the measurement of the transverse impact parameter with respect to the beam-line, the number of pixel hits, and the χ^2 of the track. The tracks are then grouped with the constraint of being less than 1 cm apart in the z direction from the neighbor. The clustered candidates are fitted with and adaptive vertex fit [45]. Weights are assigned to the track candidates depending on their distance to the common vertex [46, 47].

3.6 Alignment

The precise knowledge of the detector position is mandatory for the correct reconstruction of the tracks and its parameters. Displacements on the modules of the tracker were introduced during its installation, transportation and assembly. Also shifts on the structures occur when the magnetic field is changed or the detector is opened. Therefore the position of the modules of the sub-detectors is not as specified in the technical design report [38]. In order to correct the detector position to the so called "design position", the alignment algorithm has to be applied.

The alignment algorithm is in charge of measuring and providing the corrections to the deviation of the position of the tracks elements in the detector from their designed positions. The track reconstruction procedures use the corrections given by the alignment algorithm, to perform the correct reconstruction of the tracks [48, 49]. Figure 3.8 shows an overemphasized[3] reconstructed track with and without the alignment correction applied in an event with magnetic field B=0.

The CMS tracker detector is made out of 16500 independent silicon modules, and thus the alignment is a challenging task, as explained in [38]. The alignment uncertainties should not enlarge the tracker resolutions in a significant way, which implies that the alignment parameters have to be known better than the parameters of the resolution of the tracker. The small uncertainty in the alignment is possible since millions of tracks are used for its calculation, while the track parameters are calculated using tracks with 10 to 15 hits.

[3]The misalignment error is of the order of magnitude bellow to mm, not possible to be observed in the scale of the figure.

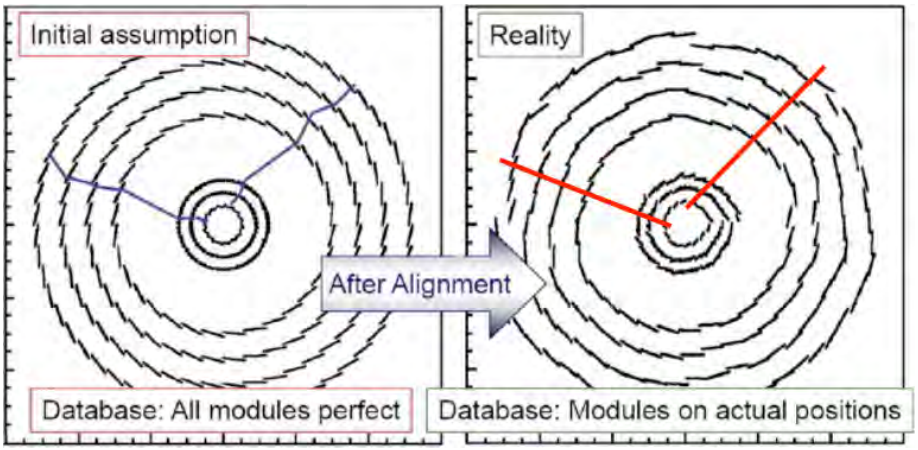

Figure 3.8: Left: Track reconstruction without using any alignment parameter and without magnetic field. Right: Track reconstructed using corrections from the alignment [50].

The first alignment of the CMS tracker used cosmic rays, optical survey information, and the laser alignment system, explained in detail in [51], but this section focuses on sub-detectors track-based alignment. Track-based alignment is designed to calculate the positions of the modules using a large sample of reconstructed charged particles tracks [48, 52]. The two track-based alignment algorithms used in CMS are the Hits and Impact Points algorithm (HIP) [53], and the MILLEPEDE-II algorithm (MP) [54, 55]. In both of them, the track residuals are minimized, where residual is the difference between the measured track position and the expected designed position.

The HIP algorithm is capable of determining all the alignment parameters per tracking sensor. The parameters are calculated using the hit residuals as a function of the alignment parameters of the modules. The HIP algorithm minimizes χ^2. This algorithm does not take into account the correlation between the alignment parameters for different modules in one iteration of the alignment, which is why it is called a local iterative algorithm. The HIP method performs an iterative procedure until the track reconstruction is stable.

The MP algorithm is a non-iterative method. MP fits all the tracks and alignment parameters at the same time, i.e. fitting simultaneously the global parameters related to the full module, and the local parameters within each module.

In 2011 the tracker alignment was done using cosmic and collision data. To validate the alignment parameters both methods (HIP and MP) were used independently which gave consistent results. Both methods were combined to obtain the final alignment used.

Chapter 4

Reconstruction and selection

This chapter summarizes the triggers and offline selection strategies used to reconstruct the $B_s^0 \to J/\psi\ \phi$ signal candidates. Monte Carlo simulations are used to understand accurately the different background contributions, as well as to assess the effects of the detector on the data collected. This work is done using data samples obtained during the 2011 run of the CMS detector, with approximately 5 fb^{-1} of data at $\sqrt{s} = 7$ TeV.

The details of the CMS data used are presented in Section 4.1. The simulation of the signal and background is discussed in Section 4.2. The trigger selection is presented in Section 4.3. The offline selection for the $B_s^0 \to J/\psi\ \phi$ is explained in Section 4.4, while the selection of the $B^0 \to J/\psi\ K^*(892)$ decay channel, which is used as a control channel for the validation of the proper decay length dependent efficiency calculations, is presented in Section 4.5. Validation of the data samples used is discussed in Section 4.6. Studies on the backgrounds are presented in Section 4.7, and finally validation studies of the data with simulation are discussed in Section 4.8.

4.1 Data samples

The LHC accelerator collided protons-protons since November 2009. From the start-up of the machine up to this date, the instantaneous luminosity $\mathcal{L}$ has not been constant, implying that the parameters defining $\mathcal{L}$, shown in Eq. 3.1, have varied. One of the most relevant parameters for this analysis is the number of protons per bunch, since this is one of the parameters that increases the number of proton-proton interactions per collision and produces more primary vertices reconstructed per event (pile-up).

As explained in Section 3.2, the data used in this thesis has an integrated lumi-

dataset	number of signal candidates $B_s^0 \to J/\psi\ \phi \to \mu^+\mu^- K^+ K^-$	integrated luminosity $\mathcal{L}$ [fb^{-1}]	proton bunches per beam	average pile-up
2011-A	6 776	2.1	<1 000	5
2011-B	7 663	2.9	1 400	11

Table 4.1: Comparison of LHC parameters in datasets 2011-A and 2011-B.

nosity of 5.0 ± 0.1 fb^{-1} at $\sqrt{s} = 7$ TeV. This data sample is taken while the LHC conditions are changing. The data sample selected is therefore divided in two parts, called 2011-A and 2011-B. The different conditions per each dataset are shown in Table 4.1, and the number of primary vertices reconstructed per dataset can be seen in Fig. 4.1. The average number of pile-up events in the dataset 2011-A is approximately 6, and for the dataset 2011-B it is around 11.

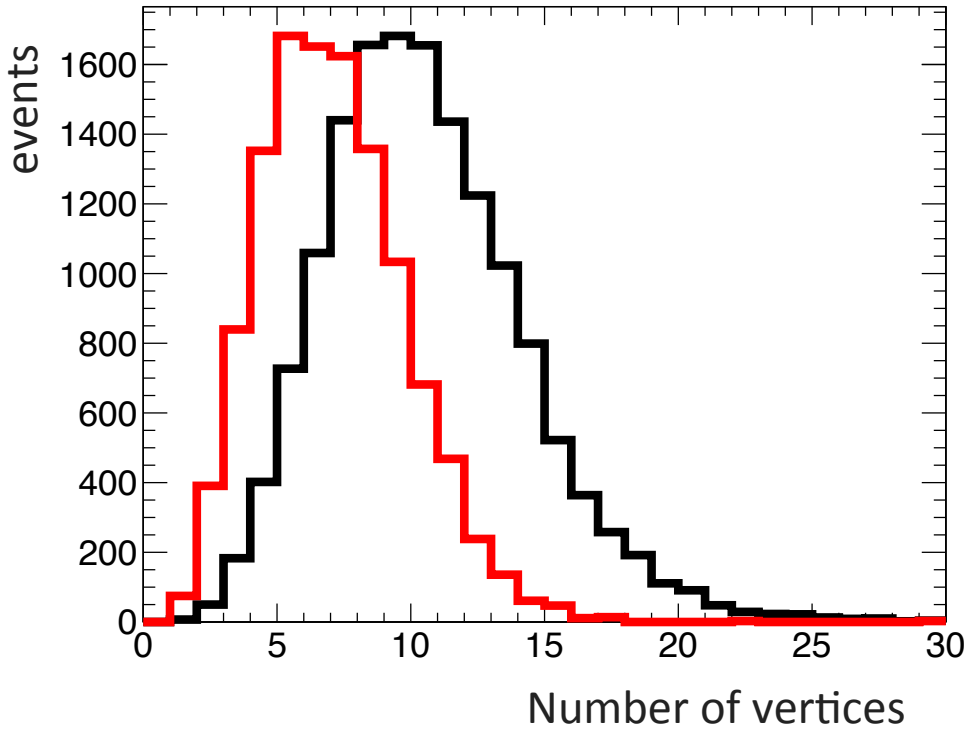

Figure 4.1: Number of vertices reconstructed per event, for the two data-taking periods, 2011-A in red and 2011-B in black.

In order to cope with the higher rate of events in the 2011-B dataset, the trigger conditions are changed between both datasets. Before merging the two datasets it is necessary to verify that the characteristics of the variables of the $B_s^0 \to J/\psi\ \phi$ candidates are similar for those datasets. Specifically one can look at the kinematics

and energy distributions of the track candidates, the validation plots between 2011-A and 2011-B are shown in Section A. If the characteristics of the events in the datasets are different, systematic effects could be introduced. The validation studies are further discussed in Section 4.6.

4.2 Monte Carlo samples

The simulated Monte Carlo (MC) data are used for several studies within this thesis. First, the MC data are used for studying the performance and reconstruction of the $B_s^0 \to J/\psi\ \phi \to \mu^+\mu^- K^+ K^-$ decay. Also, the simulation is used to study the properties and contributions of the possible background events, which are all the possible decays into $\mu^+\mu^- K^+ K^-$ final state that do not come from the $B_s^0 \to J/\psi\ \phi$ channel. Finally, the simulated data are used to validate the theoretical models and fitting techniques used for describing the properties of the $B_s^0 \to J/\psi\ \phi$ decay.

The MC samples used are generated, simulated, and reconstructed emulating the same conditions as the data recorded by the CMS detector during 2011. The MC production is performed in two steps. First, PYTHIA6 [57] is used to generate beauty production from proton-proton collisions, and hadronize the b-quarks in different b-hadron flavors (B^+, B^0, B_s^0, and Λ_b^0). Second, the b-hadrons are forced to a specific final state using EVTGEN [58], describing properly the angular distribution of the decay. A filter at generator level requires the presence of two muons, decaying within the detector acceptance ($-2.5 < \eta < 2.5$ and $p_T > 2.5$ GeV/c). Finally, events are passed through a simulation of the CMS detector based on GEANT4 [59]. The background MC samples used in this analysis are summarized in Table 4.2.

MC sample	number of events	cross section (pb)
$B_s^0 \to J/\psi\, X \to \mu^+\mu^- X$	2 092 273	2.41×10^7
$B^0 \to J/\psi\, X \to \mu^+\mu^- X$	7 890 942	2.65×10^7
$B^+ \to J/\psi\, X \to \mu^+\mu^- X$	8 389 825	2.99×10^7
$\Lambda_b^0 \to J/\psi\, X \to \mu^+\mu^- X$	2 184 854	8×10^6

Table 4.2: Summary of the used background MC samples. The number of generated events after the pre-selection cuts is shown in the second column, and the corresponding cross section in the third column.

Two signal MC samples with different $\Delta\Gamma_s$ values are generated. One sample is generated forcing the $\Delta\Gamma_s = 0$, and the other sample with the $\Delta\Gamma_s = 0.0685$ ps^{-1} (value expected by the SM).

parameter	value
$\|A_0\|^2$	0.6
$\|A_\perp\|^2$	0.16
$\|A_0\|^2$	0.24
δ_0	0
$\delta_{\|\|}$	2.50
$\delta_\perp$	-0.17
$\Delta\Gamma_s$	0.0685 ps^{-1}
$\Delta\Gamma_s/\Gamma_s$	10%
ϕ_s	0.04

Table 4.3: Parameter values used for the signal MC.

parameters	value
$\|A_0\|^2$	0.6
$\|A_\perp\|^2$	0.16
$\|A_0\|^2$	0.24
δ_0	0
$\delta_{\|\|}$	2.50
$\delta_\perp$	-0.17
$\Delta\Gamma_s$	0
$\Delta\Gamma_s/\ \Gamma_s$	0
ϕ_s	0

Table 4.4: Parameter values used for the signal MC with $\Delta\Gamma_s = 0$.

The helicity parameters used for generating the exclusive $B_s^0 \to J/\psi\ \phi$ sample with $\Delta\Gamma_s$ value expected by the SM are shown in Table 4.3. These parameters are defined in Section 2.4, and the parameter values used for the generation of the MC correspond to the Standard Model expectations. The helicity parameters used for generating the signal MC sample with $\Delta\Gamma_s$ equals to zero are presented in Table 4.4.

The signal MC samples are used to model the detector acceptance, to estimate the expected distribution of the efficiency function of the triggers, to calculate the efficiency of the selection cuts, and to validate the probability density function of the signal events. Specifically, the signal MC sample with $\Delta\Gamma_s$ =0 is needed for calculating the efficiency functions, explained in Section 5.3. That sample assures that

the time and angle variables are not correlated and that the efficiency is determined without introducing a bias [60].

4.3 Trigger selection

This section explains the different triggers used to select $B_s^0 \to J/\psi\,\phi \to \mu^+\mu^- K^+K^-$ candidate events. As explained in Section 3.4, an optimal trigger selection is necessary to obtain the highest possible number of signal events, and to reduce as much as possible contamination from background events.

In the $B_s^0 \to J/\psi\,\phi \to \mu^+\mu^- K^+K^-$ decay channel, the four-track candidates are displaced from the primary vertex due to the displaced decay of the B_s^0 meson. Previous MC studies on the $B_s^0 \to J/\psi\,\phi$ channel at CMS showed that the so called prompt J/ψ mesons (J/ψ decaying close to the interaction point) represent the dominant background [61]. Those studies motivated the use of triggers with a displaced di-muon vertex which eliminates the prompt J/ψ mesons. The trigger chain is the following: first the L1 muon trigger selects the muon candidates, and later the HLT trigger selects the di-muon displaced from the vertex.

4.3.1 L1 muon trigger

Muons have the largest probability to cross the full CMS detector without interacting until they reach the muon chambers. Therefore, they are good objects to trigger on. As explained in Section 3.4 and 3.5.2, the muon trigger and reconstruction code identify muons and calculate their momenta and locations using the information from the three different sub-detectors of the CMS muon system: Drift Tubes (DT), Cathode Strip Chambers (CSC), and Resistive Plate Chambers (RPC) [38]. First, the electronics of the L1 muon trigger are in charge of obtaining the information from the hits in the muon sub-detectors, and construct the tracks using a track finder algorithm. Then, the momentum is calculated for each muon candidate. The trigger keeps the four-tracks with the highest p_T and the best quality conditions. After that, the Global Muon Trigger (GMT) is in charge of correlating the muon candidates from the DT and CSC with the four candidates from the RPC. Moreover, the GMT can access information in the hadronic calorimeters to define the isolation of the muon candidates. Finally, the four-tracks with the best correlation, highest transverse momentum and qualities are selected to pass to the global trigger, where the full tracker information is used in order to define the global muon candidates.

4.3.2 Displaced J/ψ trigger selection

The HLT triggers used for heavy flavor searches at CMS are based on the identification of two muons with opposite charge. The different trigger paths available with 1.1 fb^{-1} of data in 2011 are shown in Fig. 4.2.

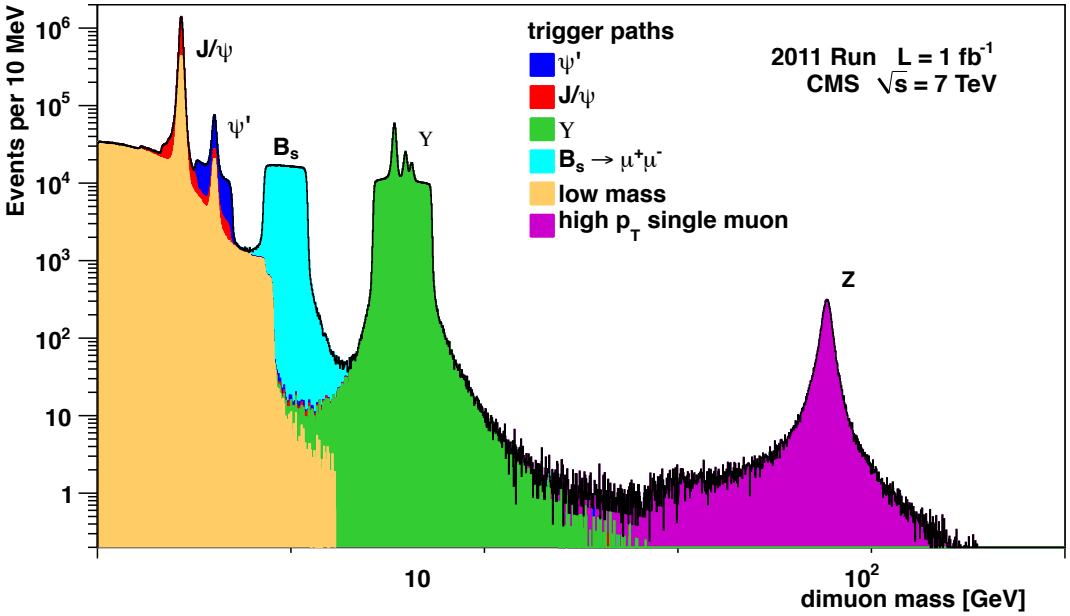

Figure 4.2: Di-muon mass distribution obtained from overlapping several trigger paths, including a series of high p_T single muon paths.

As explained in Section 4.1, during the acquisition of the data the LHC conditions changed. To cope with the variations in the rate of events, the trigger conditions are changed between different runs, being different HLT triggers (different versions of the J/ψ displaced trigger) for the two datasets. This section summarizes all the cuts used for the different versions of the displaced J/ψ trigger.

The displaced J/ψ trigger requires di-muon events with the presence of a J/ψ candidate with a vertex displaced from the primary vertex. The displaced trigger is optimized for b-hadrons with a J/ψ meson in their decay. For the di-muon pair to be accepted as a J/ψ candidate, the muons need to fulfill the kinematic requirements on the $p_T(\mu^+\mu^-)$, and $\eta(\mu^+\mu^-)$ distributions. The displaced trigger applies a requirement on the flight distance, called *significance decay length cut*. This cut is defined as $(L_{xy}/\sigma_{L_{xy}})$, where L_{xy} is the transverse distance between the beam-spot vertex position and the di-muon vertex position, and $\sigma_{L_{xy}}$ is the uncertainty on L_{xy} (including the measurement uncertainty of the di-muon vertex, and the width of the beam-spot). To constrain the direction of the di-muon transverse momentum vector

and L_{xy} to be co-linear, a cut is applied on the angle between the two, which is defined as α. The muon tracks are required to have a minimum distance from each other in the event, called distance of closest approach (DCA). To assure that the di-muon pair comes from a common vertex, a cut is placed on the vertex probability (χ^2/dof), the vertex fits are applied to the tracks using a Kalman filter. Finally, the di-muon pair is constrained to the J/ψ mass, and a cut on the p_T is applied to it.

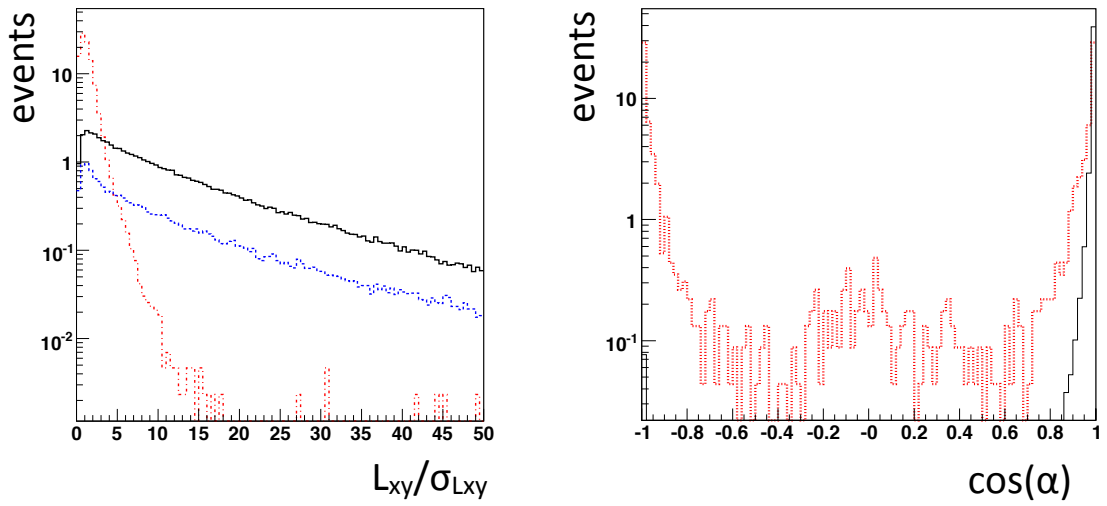

Figure 4.3: Left: Distribution of the significance of the decay length $L_{xy}/\sigma_{L_{xy}}$ with simulation data. In red are the prompt J/ψ events, and in black are the signal ($B_s^0 \rightarrow J/\psi\ \phi$) events. Right: Distribution cos(α) after applying the significance decay length cut. The prompt J/ψ events are in red, and the $B_s^0 \rightarrow J/\psi\ \phi$ signal events in black (taken from [61]).

In Fig. 4.3 are shown two simulation plots that motivated some of the trigger cuts. The left plot shows the significance decay length plots for the signal, prompt J/ψ background, and a combination of $b \rightarrow J/\psi X$ backgrounds events. The right plot shows the distribution of the cos(α), for $B_s^0 \rightarrow J/\psi\ \phi$ signal and prompt J/ψ events.

In order to create an uniform dataset, the tightest trigger selection cuts are applied offline to the full data set, with in total 5 fb^{-1}. The following trigger requirements are applied:

- Each muon is required to have a transverse momentum of $p_T > 4$ GeV/c.
- Each muon must be within a pseudorapidity of $|\eta| < 2.2$.
- The di-muon pair is required to have a transverse momentum of $p_T > 6.9$ GeV/c.

- The significance decay length has to be $L_{xy}/\sigma_{L_{xy}} > 3$.
- The di-muon vertex is required to have $\chi^2/d.o.f. < 10$, which implies a vertex probability > 15 %.
- The di-muon pair is required to have a distance of closest approach of $(DCA) <$ 0.5 cm.
- The invariant mass of the di-muon pair must be between $2.9 < M(\mu^+\mu^-) < 3.3$ GeV/c^2.

The displaced trigger can induce systematic uncertainties on the data, produced as an effect of the displacement cut. The displaced trigger removes the events with proper decay time close to zero, which includes the region used for calculating the resolution of the decay time. A different set of triggers is necessary to verify the possible systematic effects, and to calculate the proper decay time resolution. The so-called "barrel" trigger is selected because it does not have a ct cut around zero, and it does not reject the prompt events. There are two reasons for not selecting the barrel trigger as nominal trigger. The first reason is that the number of event candidates is smaller than in the displaced trigger[1], and the second is that the signal to background yield is bigger.

The barrel trigger cuts are:

- The di-muon pair is required to have transverse momentum of $p_T > 6.9$ GeV/c.
- The di-muon pseudorapidity is required to be $|\eta| < 1.25$.
- The di-muon mass must be between 2.3 GeV/c^2 and 3.5 GeV/c^2.

The discussion about the calculus of the resolution parameters, and the possible differences between the displaced and barrel triggers can be found in Section 5.1.3.

4.4 $B_s^0 \to J/\psi\ \phi$ event reconstruction

Further cuts are necessary in order to reduce the background as much as possible in the $B_s^0 \to J/\psi\ \phi \to \mu^+\mu^- K^+K^-$ decay candidates. The offline reconstruction of the signal candidates is based on the identification of the $J/\psi \to \mu^+\mu^-$ candidates and their combination with the $\phi(1020) \to K^+K^-$ candidates.

[1]The barrel trigger is pre-scaled, that means there is a factor associated to the trigger that allows only a fraction of the possible events that are accepted by the trigger.

First the $\mu^+\mu^-$ candidates are selected from triggered global muons[2], coming from the same vertex. Additionally, the following cuts are applied to the muon pair:

- The di-muon pair is required to have transverse momentum of $p_T\ (\mu^+\mu^-) >\ 7$ GeV/c.

- The J/ψ mass difference with respect to the J/ψ mass value is required to be $|\Delta\ \mathrm{M}(J/\psi)|\ < 150$ MeV/c^2.

where the $\Delta\mathrm{M}(J/\psi)$ is the difference between the J/ψ reconstructed and the world-average J/ψ mass, $M(J/\psi)_{PDG} = 3096$ MeV/c^2 [12].

Once the J/ψ candidate is selected, the next step is to reconstruct the $\phi(1020) \rightarrow K^+K^-$ candidates. To reconstruct the meson, a pair of opposite charged tracks with more than five hits in the tracker is assumed to be kaons. The following conditions are applied to the pair of kaons candidates:

- The kaon pair is required to have transverse momentum of $p_T(K^{\pm}) >\ 0.7$ GeV/c.

- The kaon pair invariant mass difference with respect to the $\phi(1020)$ mass value should be $|\Delta\ \mathrm{M}(\phi(1020))| <\ 10$ MeV/c^2,

where $|\Delta M(\phi(1020))|$ is the difference of the mass between the reconstructed $\phi(1020)$ candidate and the measured world average $\phi(1020)$ mass, $M(\phi(1020))_{PDG} = 1019$ MeV/c^2 [12].

The B_s^0 candidates are formed combining the $\phi(1020)$ and J/ψ candidates with an invariant mass required to be between 4.5 and 6 GeV/c^2. Then, kinematic and vertex fits are applied to the tracks using a Kalman filter, while assuming the tracks to have a common vertex. The J/ψ meson candidates are constrained to the $M(J/\psi)_{PDG}$. The $\phi(1020)$ meson candidates masses are not constrained because the width of the $\phi(1020)$ is larger than the experimental resolution. More details of the kinematic and vertex fits can be found in [61, 62]. Figure 4.4 shows the invariant mass with and without the kinematic fit of simulated $B_s^0 \rightarrow J/\psi\ \phi$ events. The invariant mass resolution improved with the kinematic fit in 54%, from $\sigma = 35$ MeV/c^2 to $\sigma = 16$ MeV/c^2. The B_s^0 candidate is required to have a χ^2 vertex fit probability bigger

[2] For an explanation of global muons see Section 3.5.2.

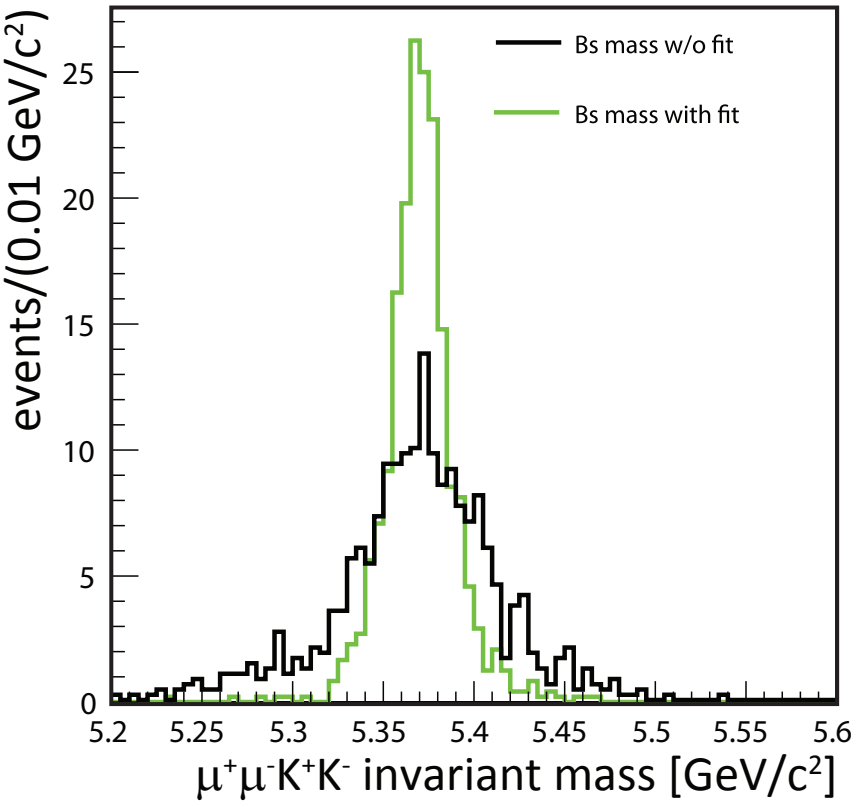

Figure 4.4: $\mu^+\mu^-K^+K^-$ invariant mass distribution without applying the kinematic fit (black), and with kinematic fit applied (green) for the simulated signal MC.

than 2%, and the reconstruction of the invariant mass has to be within 5.20 MeV/c^2 $< M(\mu^+\mu^-K^+K^-) <$ 5.6 MeV/c^2.

Finally, the last set of cuts is applied to perform the maximum likelihood fit, explained in Section 5.1. These cuts are:

- The B_s^0 candidates invariant mass must lie between 5.24 MeV/c^2 $< M(J/\psi K^+K^-) <$ 5.49 MeV/c^2.

- The proper decay length ct follows the range between 0.02 and 0.3 cm,

where the proper decay length is one of the main variables used in the description of the $B_s^0 \to J/\psi\ \phi$ decay channel in Chapter 5, and the definition is explained in Section 5.1.3 (the justification for the ct cut is given in Section 5.3.1). These last two cuts on the invariant mass and proper decay length are removed for the calculus of the distribution of the efficiency functions.

After all the cuts, the final number of $B_s^0 \to J/\psi\ \phi$ event candidates is 19 200 events. The invariant mass distributions of the $\phi(1020)$, and J/ψ meson candidates are shown in Fig. 4.5. The invariant mass distribution of the $B_s^0 \to J/\psi\ \phi \to \mu^+\mu^- K^+ K^-$ candidates, with sidebands regions (defined in the next section), is shown in Fig. 4.6.

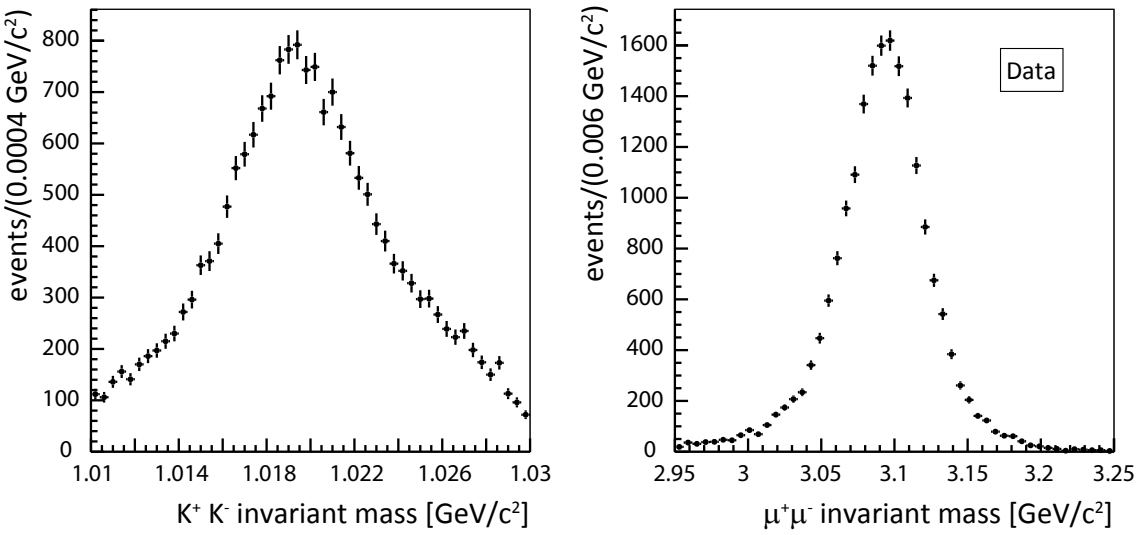

Figure 4.5: Invariant mass distribution of the $\phi(1020)$ meson (left) and J/ψ meson (right), after all the selection cuts.

4.4.1 Definition of the side bands

Figure 4.6 shows the sidebands definition. Two sidebands are defined, one to the left of the B_s^0 mass candidates peak, and one to the right. The mass sideband range that goes from 5.24 GeV/c^2 to 5.28 GeV/c^2 is defined as the left sideband. The mass sideband that goes from 5.45 GeV/c^2 to 5.49 GeV/c^2 is defined as the right sideband. Several background studies are performed on the data sample by fitting events from the sidebands of the B_s^0 mass peak.

4.5 $B^0 \to J/\psi\ K^*(892)$ event selection

The $B^0 \to J/\psi\ K^*(892)$ decay channel serves as a reference channel for this analysis. The decay is similar to the $B_s^0 \to J/\psi\ \phi$ decay, and it is used to validate the time-efficiency determination technique (see Section 5.3.1, and to study a possible source of background due to pion misidentification in the systematics (see Section 5.6.2).

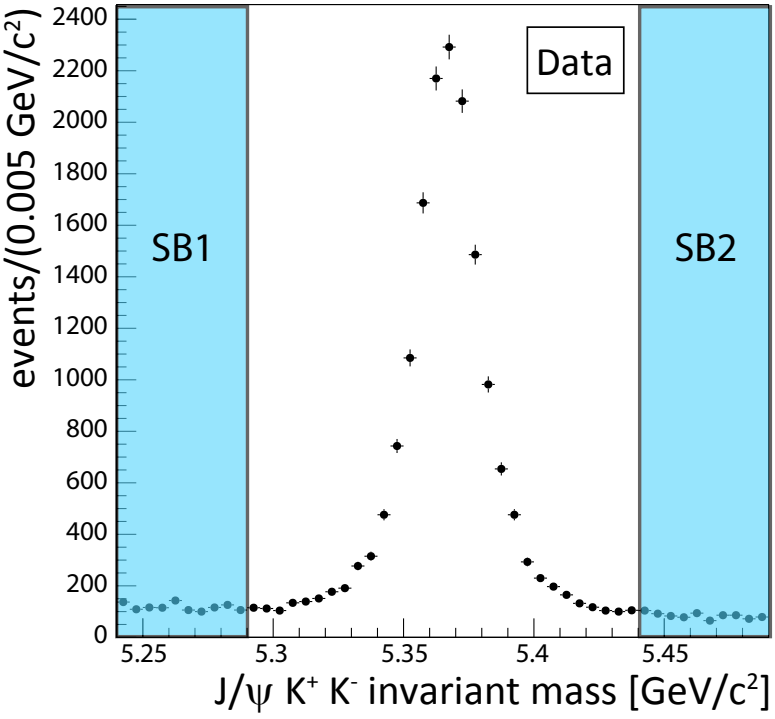

Figure 4.6: $J/\psi\ K^+K^-$ invariant mass distribution, with the sidebands definitions in blue. The left sideband is in the range $[5.24, 5.28]$ GeV/c^2, and the right sideband is in the range $[4.45, 5.49]$ GeV/c^2.

The strategy to reconstruct the $B^0 \to J/\psi\ K^*(892)$ decay is to utilize selection cuts as similar as possible to the ones applied to the $B_s^0 \to J/\psi\,\phi$ decay. The difference between them are on the B^0 mass (B^0 PDG mass value is 5279.58 ± 0.17 MeV/c^2), and on the cuts applied to reconstruct the $K^*(892) \to K^+\pi^-$ candidates. The selection of the K^* requires two oppositely charged tracks, where one track is assumed to be a pion, and the other track a kaon. Afterwards, the tracks with the invariant mass closest to the nominal PDG K^* mass value are selected, and the following cuts are applied,

- The $K^*(892)$ mass difference with respect to the $K^*(892)$ PDG value is required to be $|\Delta M(K^*(892))| < 150$ MeV/c^2.

- The invariant mass of the $K^*(892)$ meson candidates must be between $0.796 < M(K^*) < 0.996$ GeV/c^2.

- The B^0 candidates invariant mass is required to be within $5.05 < M(J/\psi\ K^+\pi^-) < 5.6$ GeV/c^2

where $\Delta M(K^*)$ is the difference between the K^* reconstructed mass and the world-average of the K^* mass, $M(K^*)_{PDG} = 892$ MeV/c^2 [12]. The error of wrong mass assignment is estimated to be of the order of 15%, from MC studies.

4.6 Combination of the data samples

A comparison of kinematic variables, between the datasets 2011-A and 2011-B, is performed to verify that the two data samples can be merged into one sample[3].

First the kinematic distributions of the four-track candidates are reviewed, regarding the distance of closest approach (DCA) of the two muons, the $\Delta\alpha$ between the muons, the pseudo-rapidity of the four-track candidates, and the transverse momentum p_T of the kaon and muon candidates. Afterwards, the distributions of the final B_s^0 candidates are compared, by checking the transverse momentum p_T, the pseudorapidity η, the primary and secondary vertex, the proper decay length, the invariant mass, and the angle distributions $\cos\theta$, φ, and $\cos\psi$ of the B_s^0 candidates.

No apparent difference could be observed when studying and comparing kinematics distributions of the $B_s^0 \to J/\psi\ \phi$ decay, between datasets 2011-A, and 2011-B. Based on this result, it is assumed that the analysis is pile-up independent, and both datasets can be merged.

4.7 Study of the backgrounds

The studies of the possible backgrounds are performed using the MC simulations listed in Section 4.2. The MC samples utilized contain different possible sources of background to the decay channel $B_s^0 \to J/\psi\ \phi \to \mu^+\mu^- K^+ K^-$. In order to emulate the same conditions in the simulations as in the real data, the trigger and offline selection cuts are applied to all the MC samples.

From previous analyses [61,63] two main types of possible backgrounds are known: prompt J/ψ, and non-prompt J/ψ background. The prompt J/ψ background, as explained in Section 4.3, are all the candidates events that form a J/ψ meson produced at the proton-proton interaction point. However, with the use of the displaced trigger, and the tight selection cut in the significance of the decay length, ($L_{xy}/\sigma_{L_{xy}} > 3$), most of the J/ψ prompt events are removed, and the event candidates selected are the ones produced in a secondary vertex. The non-prompt J/ψ events are all the

[3]More details can be found in [8].

events produced in a secondary vertex, and that are misreconstructed as $B_s^0 \rightarrow J/\psi\ \phi \rightarrow \mu^+\mu^- K^+K^-$ event candidates. Since the CMS detector does not have particle identification, in the reconstruction of the $\phi(1020)$ candidates all the tracks are considered kaons, leading to combinatorial backgrounds.

The backgrounds affecting this analysis are the B mesons decaying into J/ψ and two tracks: B^0, B^+, and Λ_b^0. However, the Λ_b^0 mesons contribution in the misreconstructed events is found to be small. Figure 4.7 shows the $\mu^+\mu^- K^+K^-$ invariant mass peak with the contribution of the different backgrounds. In Table 4.5 can be seen how the main backgrounds are reduced after the $B_s^0 \rightarrow J/\psi\ \phi$ selection cuts.

Table 4.5: Number of events passing for scaled MC samples after different selection cuts.

Cut	N_{events} $B^0 \rightarrow J/\psi X$	N_{events} $B^+ \rightarrow J/\psi X$	N_{events} $B_s^0 \rightarrow J/\psi \phi$
Events before cuts	7 110 942	7 069 825	377 878
$p_T(\mu^\pm) > 4$	1 368 100	1 338 890	15 449
After kinematic fit	496 653	484 408	15 449
K^+K^- vertex probability$> 2\%$	104 194	99 558	12 645
$p_T(K^\pm) > 0.7$ GeV	57 915	54 683	11 464
$\lvert\Delta M(\phi(1020))\rvert <$ 10 MeV/c^2	30 321	12 779	10 171
$L_{xy}/\sigma_{Lxy} > 3$	1 890	1 316	7 243

As can be seen in Fig. 4.7, the channel $B^0 \rightarrow J/\psi\ K^*(892) \rightarrow \mu^+\mu^- K^+\pi^-$ is one of the main background contributions, producing a broad distribution underneath the $\mu^+\mu^- K^+K^-$ peak. This channel can be called a peaking background. The $B^0 \rightarrow J/\psi\ K^*(892)$ decay has a similar topology to the $B_s^0 \rightarrow J/\psi\ \phi$ decay. When the kaon mass is assigned to the pion track, due to misidentification, the wrong $\mu^+\mu^- K^+K^-$ invariant mass is reconstructed. The $B^0 \rightarrow J/\psi\ K^*(892)$ background is parameterized and it is considered as a possible source of systematic errors in the final results of Section 5.6.

4.8 Data and simulation comparison

To ensure that the signal $B_s^0 \rightarrow J/\psi\ \phi \rightarrow \mu^+\mu^- K^+K^-$ is simulated correctly, the MC sample is compared with data. An accurate simulation of the events is important because the MC is used to determine the effects of the geometry of the detector in

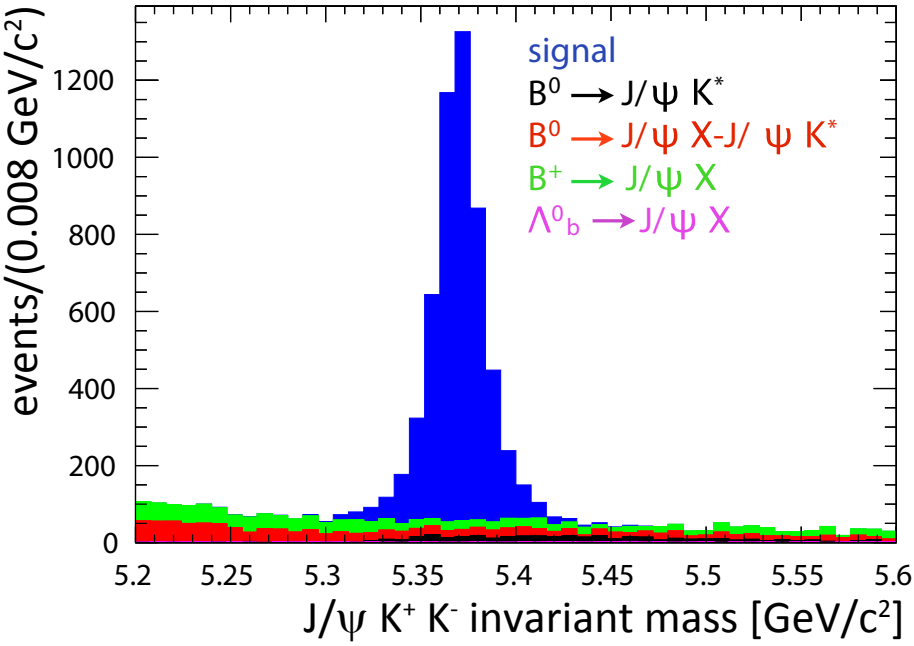

Figure 4.7: Invariant mass of $J/\psi\ K^+K^-$ as obtained from simulations.

the reconstruction of the events, to measure the resolution effects, and to calculate the reconstruction efficiency on the software.

In order to select a clean sample of signal events from the data, the background from the sidebands regions is subtracted to the signal region. The signal region in the data are selected using a tight region around the peak of the B_s^0 mass candidates, [5.33, 4.4] GeV/c^2. The sideband regions selected are explained in Section 4.4.1. Then, the normalized distributions of the MC $B_s^0 \to J/\psi\ \phi \to \mu^+\mu^- K^+K^-$ events are compared with the events left in data from the sidebands subtraction.

The distributions that are compared between MC and data are:

- The distribution of the p_T of the decaying products. In Fig. 4.8 the p_T distributions for the two muons, and for the two kaons can be seen. Figure 4.9 shows the p_T distributions for the J/ψ, and $\phi(1020)$ mesons candidates.

- The invariant mass distribution of the J/ψ, and $\phi(1020)$ candidates. The different distributions are shown in Fig. 4.10. The J/ψ and the ϕ mass distributions appear to be simulated perfectly.

- The distributions of the three physical angles that define the $B_s^0 \to J/\psi\,\phi$ decay: $\cos\theta, \phi, \cos\psi$. The angle distributions can be seen in Fig. 4.11. The distribution $\cos\psi$ has some discrepancies between data and MC which are attributed to the

detector acceptance. Some differences between data and simulation can be seen as well in the edge of the $\cos\theta$ distribution, around the value one.

It is concluded that there are no apparent differences between the data and the simulation, except for the distributions mentioned before. These results give confidence to the signal simulation. The cases where some variations are found, are taken into account for possible systematic effects.

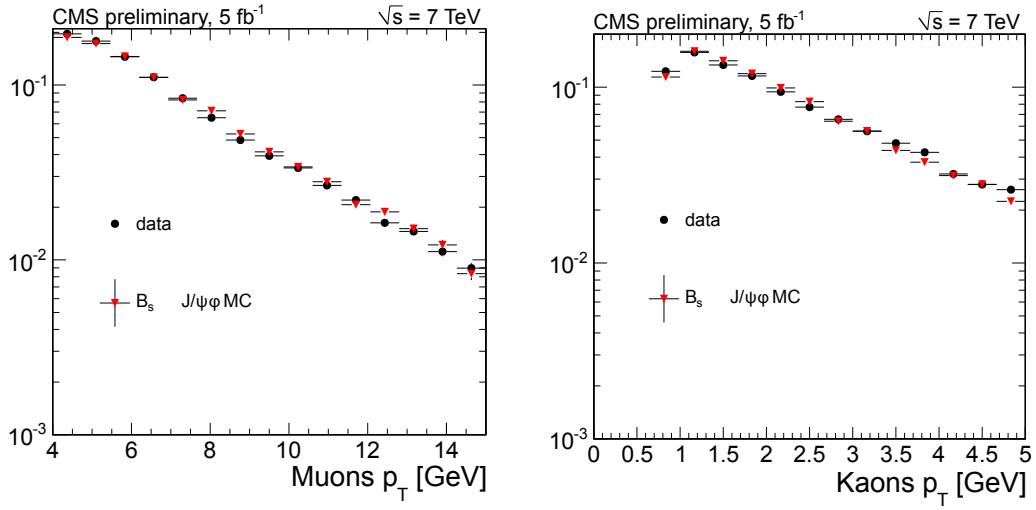

Figure 4.8: Normalized p_T distributions of the muon (left) and kaon (right) candidates.

4.9 Summary

This chapter describes the reconstruction and selection of the $B_s^0 \to J/\psi\ \phi$ decay channel. The data selected correspond to an integrated luminosity of 5.0 ± 0.1 fb^{-1} at $\sqrt{s} = 7$ TeV, collected during the 2011 data taking period. In the $B_s^0 \to J/\psi\ \phi \to \mu^+\mu^- K^+ K^-$ decay channel the four-track candidates are displaced from the primary vertex due to the displaced decay of the B_s^0 meson. The selection of the event candidates is therefore based on a trigger that requires di-muon events with the presence of a J/ψ candidate with a vertex displaced from the primary vertex. Different MC data are used to validate the theoretical models, the contributions of the possible background events, and the event selection techniques. The studies of the different possible triggers, while comparing the results obtained from real data with the results from MC studies, confirm that the triggering and selection methods used are appro-

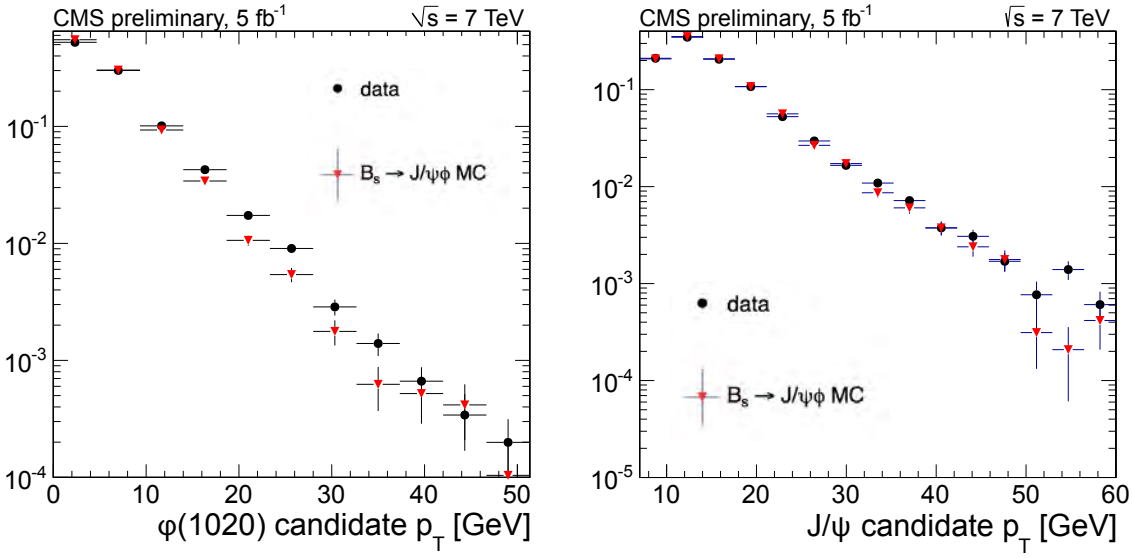

Figure 4.9: Normalized p_T distributions of the $\phi(1020)$ (left), and J/ψ (right) candidates.

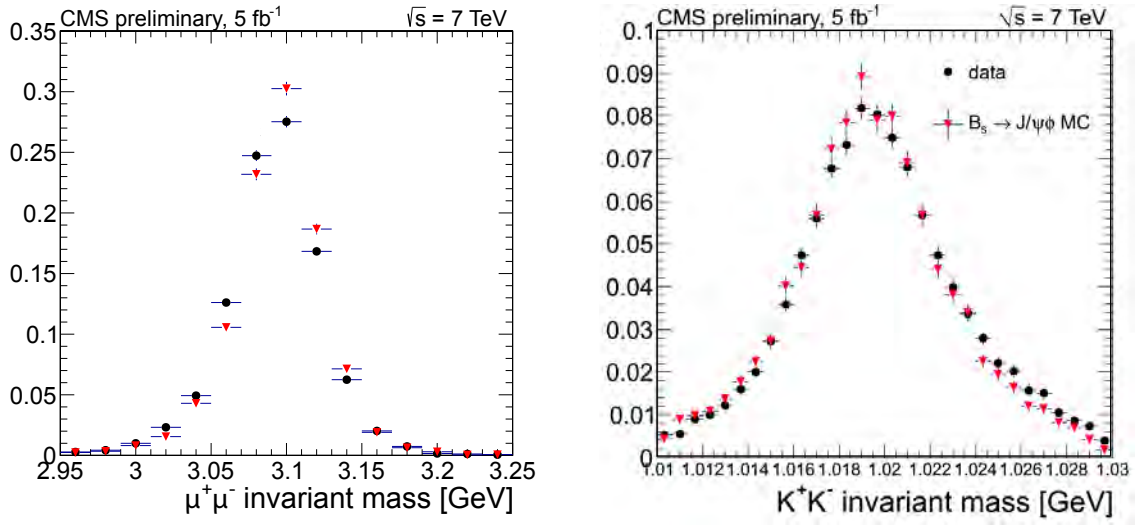

Figure 4.10: Normalized distribution of the invariant mass of the J/ψ (left), and $\phi(1020)$ (right) candidates.

priate for selecting the $B_s^0 \to J/\psi\ \phi \to \mu^+\mu^- K^+ K^-$ decay channel. After applying all selection cuts 19 200 $B_s^0 \to J/\psi\ \phi$ event candidates are left.

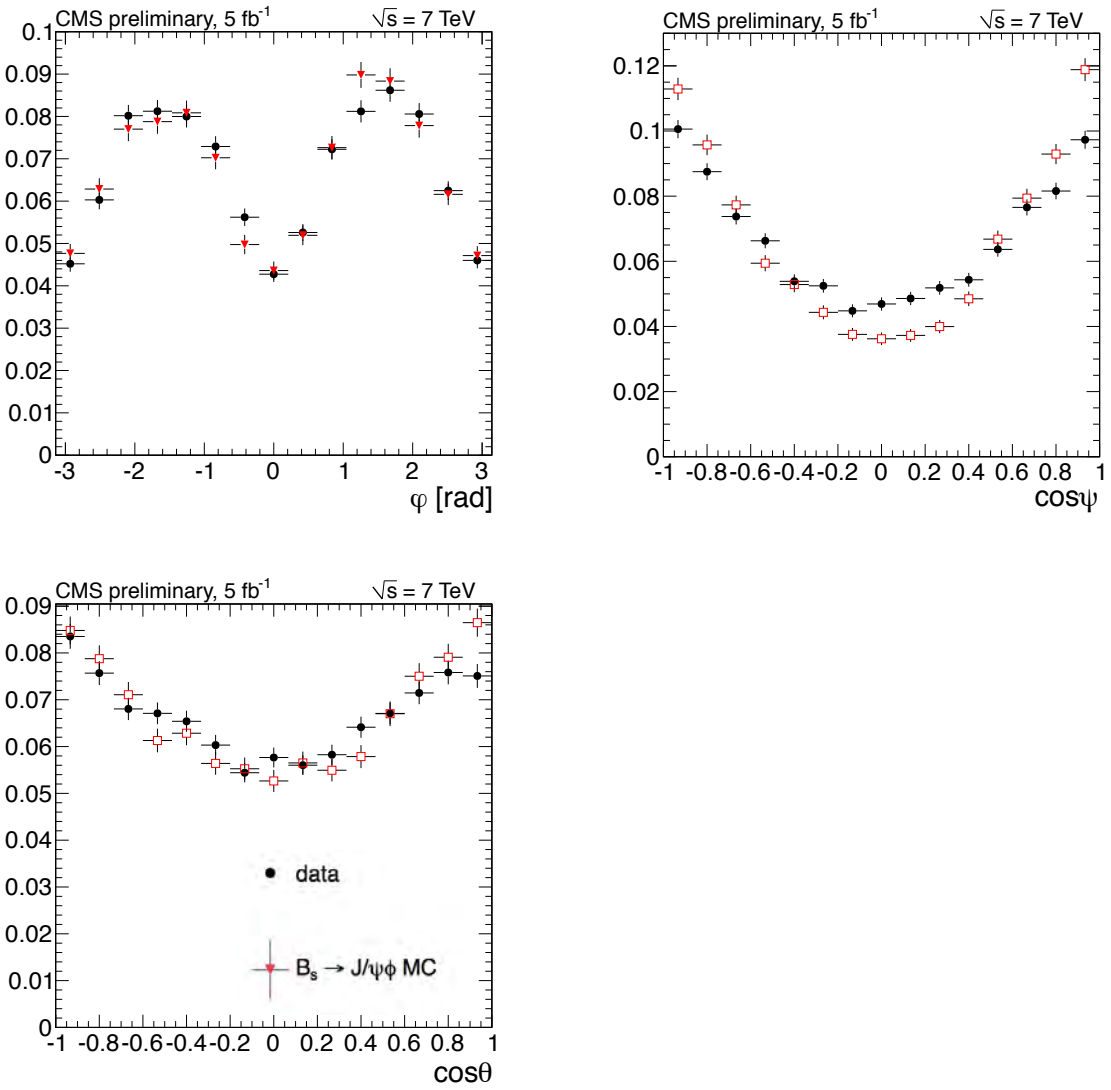

Figure 4.11: Normalized distribution of the angles φ (top left), $\cos\psi$ (top right), and $\cos\theta$ (bottom).

Chapter 5

$B_s^0 \to J/\psi\ \phi$ angular analysis

This chapter discusses the steps to determine the width difference $|\Delta\Gamma_s|$, Eq. 2.15, between the heavy and light mass eigenstates (B_s^L, and B_s^H) of an untagged sample of $B_s^0 \to J/\psi[\to \mu^+\mu^-]\phi(1020)[\to K^+K^-]$ candidates.

As described in Section 2.4, an angular analysis is necessary to disentangle the mass eigenstates of the $B_s^0 \to J/\psi\,\phi$ channel. In order to perform the angular analysis, first the B_s^0 meson candidates need to be selected from the full CMS data using the triggers and selection methods described in Section 4.3 and 4.4. Then, a multiple likelihood fit is developed to extract the parameters of interest. In the description of the fit it is necessary to include the detector distortions, the efficiency effects, and the function that describes the background model. Once the full probability function is built, a series of pseudo-experiments are used to validate the method. Finally, this analysis assumes that the mixing phase ϕ_s is zero, and the following parameters are extracted: Γ_s, $|\Delta\Gamma_s|$, $|A_0|^2$, $|A_\perp|^2$, and the strong phase $\delta_{||}$. This study does not determine the signed of the value $\Delta\Gamma_s$, but presents the positive result based on the verification of this property by [25].

5.1 Full probability density function

The fitting technique, developed for extracting the physical parameters α=$\{\Gamma_s$, $|\Delta\Gamma_s|$, $|A_0|^2$, $|A_\perp|^2$, $\delta_{||}\}$, is based on the maximum-likelihood method. For simplicity $\Delta\Gamma_s$ in this section is written without the absolute value. The algorithm estimates the value of the parameters given a finite data sample, such that these parameters maximize the likelihood function [64]. For example, if $f(x, \lambda)$ is the probability function for x measured quantities and a free parameter λ, the probability of measuring x_j...+x_j+dx

is:

$$dP_j = f(x_j, \lambda)dx_j. \tag{5.1}$$

Then, the probability of $j = 1, ...N$ measurements is the likelihood function L defined as:

$$L(\lambda) = dP = \prod_{j=1}^{N} f(x_j, \lambda)dx, \tag{5.2}$$

where N is the number of events, and λ is the most likely value for which L is maximum.

The total probability density function (PDF) that describes the $B_s^0 \to J/\psi\,\phi$ decay, after reconstructing and selecting the event candidates, needs to include signal and background components. The unbinned maximum likelihood fit is performed using the distributions of the invariant mass of $\mu^+\mu^-K^+K^-$ events denoted by M, the proper decay length represented as t, and the angles that define the kinematics of the decay denoted by $\Theta = (\cos\theta, \varphi, \cos\psi)$.

Equation 5.3 defines the full likelihood function developed for this study:

$$L(\alpha) = \prod_{i=1}^{N}[N_s\mathcal{P}(\Theta_i, \alpha, t_i, M_i) + N_b\mathcal{B}(\Theta_i, t_i, M_i)], \tag{5.3}$$

where $\mathcal{P}$ is the signal PDF, $\mathcal{B}$ is the background PDF, N_s is the number of signal events, N_b is the number of background events, and α is the set of physics parameters evaluated for the i candidate.

In the next sections, the signal and background PDFs are defined for the full modeling of the datasets.

5.1.1 The signal PDF

The theoretical signal PDF, without any detector or selection distortion, is modeled using the decay rate function as described in Section 2.3:

$$\frac{d^4\Gamma(B_s(t))}{d\Theta dt} = f(\Theta, \alpha, t) = \sum_{i=1}^{6} O_i(\alpha, t).g_i(\Theta), \tag{5.4}$$

where O_i are the kinematics-independent observables presented in Eq. 2.23, g_i are the angular distributions, introduced in Eq. 2.25, α is the set of physics parameters ($\Delta\Gamma_s$, Γ_s, $|A_\perp|^2$, $|A_0|^2$, and $\delta_{||}$) to be extracted from the fit, Θ are the angles that define the kinematic of the decay $(\cos\theta, \varphi, \cos\psi)$ defined in Eq. 2.24, and t is the proper decay length[1]. In reality, detector, triggers, and reconstruction effects distort

[1]The variable is ct, where c is the velocity of light, but t is used by simplicity

the observable distributions used for the analysis. All the distortions are included in the fit using an efficiency function ϵ, which factorizes into proper decay length dependent efficiency ($\epsilon(t)$), and angular efficiency ($\epsilon(\Theta)$):

$$\epsilon(t, \Theta) = \epsilon(t) \times \epsilon(\Theta). \tag{5.5}$$

The efficiency function multiplies the theoretical signal PDF. In Section 5.3 the methods to calculate the efficiencies are detailed. The complete signal PDF that describes the $B_s^0 \to J/\psi\ \phi$ signal event candidates in data is defined as:

$$\mathcal{P} = (f(\Theta, t; \alpha) \otimes G(t; \kappa, \sigma_t)) \cdot \mathcal{P}_m(M) \cdot \epsilon(t) \cdot \epsilon(\Theta), \tag{5.6}$$

where $f(\Theta, t; \alpha)$ is the theoretical signal PDF, and $G(t; \kappa, \sigma_t)$ is the resolution function of the proper decay length, including the uncertainty for each individual event σ_t scaled by a factor κ. The parameterization of $G(t; \kappa, \sigma_t)$ is explained in Section 5.2. The $\mathcal{P}_m(M)$ is the B_s^0 mass signal model PDF, defined as the sum of two Gaussian functions.

5.1.2 The background PDF

The background events present in the data sample are all the events that are not the signal decay $B_s^0 \to J/\psi\ \phi \to \mu^+\mu^- K^+ K^-$ and are not rejected by the selection cuts. To parameterize the background events, an empirical model is developed using the sideband regions of the B_s^0 mass peak. The total background PDF is given by:

$$\mathcal{B}(\Theta, t, M) = \mathcal{B}f(\Theta) \times \mathcal{B}_m(M) \times \mathcal{B}_t(t) \times R(ct; \mu_{br}, \sigma_{b1}, \sigma_{b2}), \tag{5.7}$$

where $\mathcal{B}f(\Theta)$ is the PDF of the angular distributions, $\mathcal{B}_m(M)$ is the PDF that models the invariant mass distribution, $\mathcal{B}_t(t)$ is the PDF of the proper decay length distribution, and $R(ct; \mu_{br}, \sigma_{b1}, \sigma_{b2})$ is the resolution function. The different parameterizations used for the background PDFs are defined as follows:

- $\mathcal{B}_m(M)$ of the mass distribution for the background events is an exponential function.
- $\mathcal{B}_t(t)$ proper decay length is given by two decay functions, convoluted with a Gaussian as a resolution function:

  $$\mathcal{B}_t(t) = f e^{-ct/(c\tau_s)} + (1 - f) e^{-ct/(c\tau_l)}, \tag{5.8}$$

  where f is the fraction of the decay for the short-lived background events (τ_s), and $(1 - f)$ is the fraction for the long-lived background events (τ_l).

- $R(ct; \mu_{br}, \sigma_{b1}, \sigma_{b2})$ is the resolution function defined with two Gaussian functions with a common mean μ_{br}, and the two standard deviations σ_{b1} and σ_{b2}.

- $\mathcal{B}f(\Theta)$ has been assumed to be factorizable as $\mathcal{B}f(\Theta) = PDF(\cos\theta) \times PDF(\cos\psi) \times PDF(\varphi)$. The distributions for $\cos\theta$ and $\cos\psi$ are described analytically by a series of Legendre functions, while the PDF of the angle φ is given by the following parameterization:

$$A + B \times \sin(2 \times \varphi + C). \tag{5.9}$$

The possible correlation between the angles in the sideband regions has been added to the studies of the systematic effects discussed in Section 5.6.

5.1.3 Multiple likelihood fit input variables

The multiple likelihood fit describes the observables of the $B_s^0 \to J/\psi\,\phi \to \mu^+\mu^- K^+ K^-$ candidates: $\cos\theta$, φ, $\cos\psi$, M, and ct. The variables are defined as follows:

- **Invariant mass of the $B_s^0 \to J/\psi\ \phi \to \mu^+\mu^- K^+ K^-$ candidates.** The measurement of the invariant mass of the B_s^0 candidates is used for its discriminating power of signal and background, as explained in Section 5.1.1. As seen in Fig. 5.1, thanks to the large statistic, the B_s^0 mass peak is prominent defining the signal region with good accuracy.

- **Angular distributions: $\cos\theta$, φ, $\cos\psi$.** The definition of $\Theta = (\cos\theta, \varphi, \cos\psi)$ is given in Eq. 2.24, Section 2.6. Figure 5.2 shows the three distributions for the full dataset used in this analysis.

- **Proper decay length.** The proper decay length is calculated transforming the proper decay length measured on the lab frame to the particle frame through a Lorentz transformation. In the B_s^0 particle reference frame:

$$ct = c\frac{t_{lab}}{\gamma} = c\frac{L}{\beta\gamma c} = cL\frac{M}{p} = cL_{xy}\frac{M}{p_T}, \tag{5.10}$$

  where M is the world average B_s^0 meson mass value [12], p (p_T) is the momentum (transverse momentum) of the reconstructed particle, L (L_{xy}) is the decay length distance (transverse decay distance in xy-plane) between the beam spot and secondary vertex, and γ is the usual Lorentz factor:

$$\gamma = \frac{1}{\sqrt{1-\beta^2}}, \tag{5.11}$$

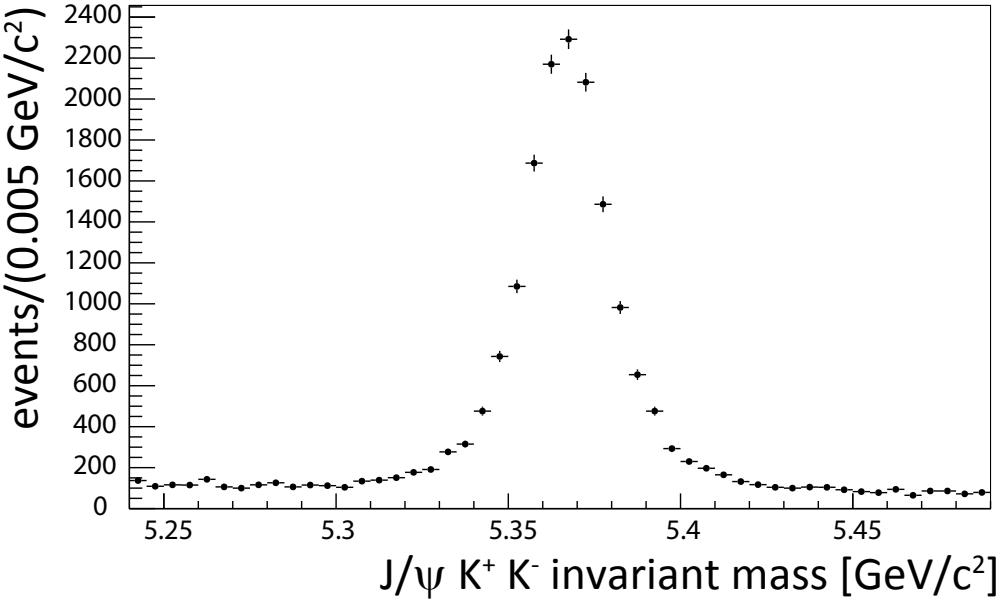

Figure 5.1: $J/\psi\, K^+K^-$ invariant mass distribution after all selection cuts.

where and $\beta = \nu/c$, and ν is the velocity of the B_s^0 meson. In Fig. 5.3 the distributions of the transverse decay length in the xy-plane, and the proper decay length on data are presented.

5.2 Resolutions

The resolution effects of a variable are the uncertainties on the measured parameters, for example due to a misreconstructed particle. If these effects are underestimated, the calculation of the physical parameters may lead to a bias. As a result, the resolution effects need to be well understood, and added in the description of the data observables.

The following sections study the resolution effects on the observables: Proper decay length, the angles describing the kinematics of the decay, and invariant mass.

5.2.1 Proper decay length resolution

The detector resolution and the fitting of the tracks affect the measurement of the decay time. Since the error associated to the decay time measurement changes for each event, this analysis uses a resolution function with per-event errors. Figure 5.4 shows the distribution of the error associated to the proper decay length. The error

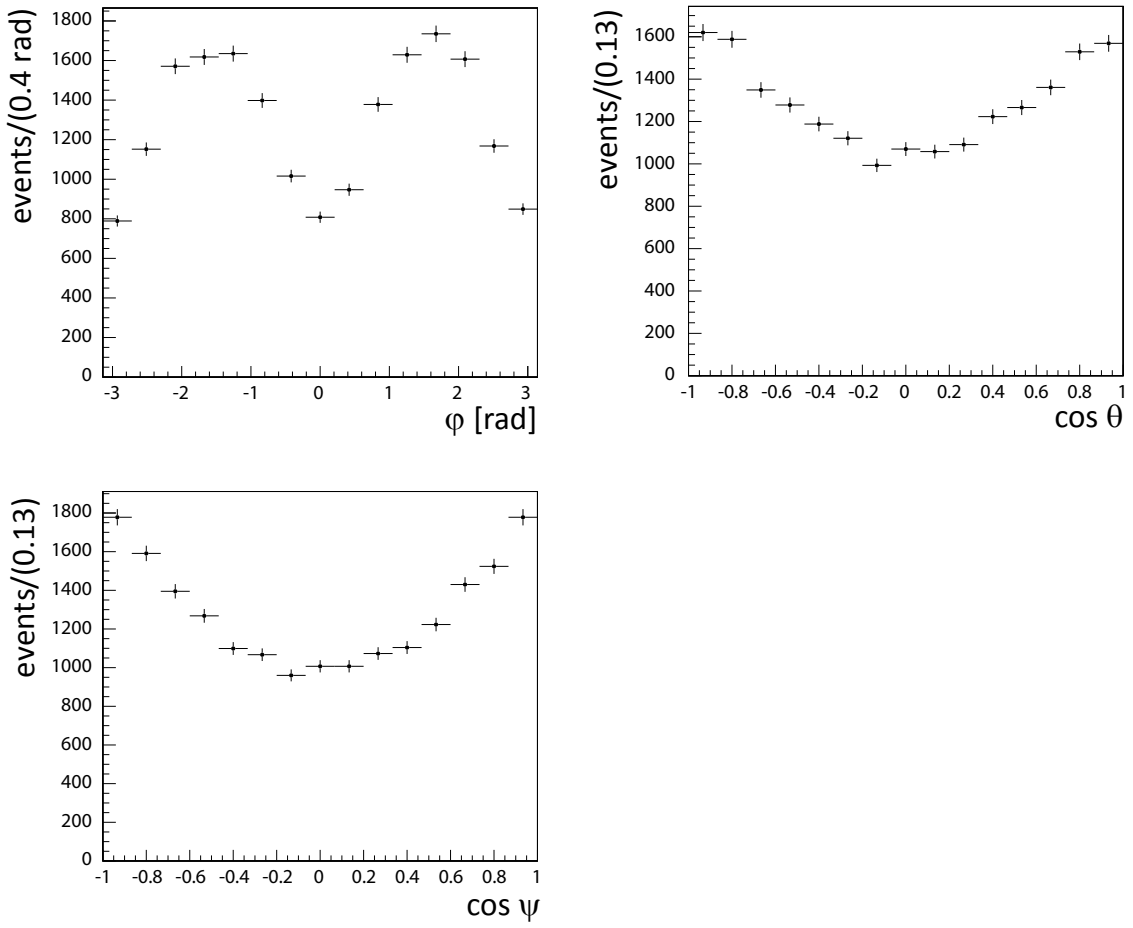

Figure 5.2: Distribution of the measured φ (top left), $\cos\theta$ (top right), and $\cos\psi$ (bottom).

is defined as:

$$\sigma_t = \sigma_{ct} = \sigma_{L_{xy}} \frac{M}{p_T}, \tag{5.12}$$

where M is the world average B_s^0 mass value [12], σ_{L_xy} is the error associated to the transverse decay distance in the xy-plane, and p_T is the B_s^0 transverse momentum. Additionally, the uncertainty σ_t needs to be corrected for the overestimation or underestimation of the calculated track errors due to the vertex fitting. This correction is known as the scale-factor SF (or called κ):

$$\sigma_t \mapsto SF \times \sigma_t. \tag{5.13}$$

The method used to extract the scale factor from data is explained in the following section.

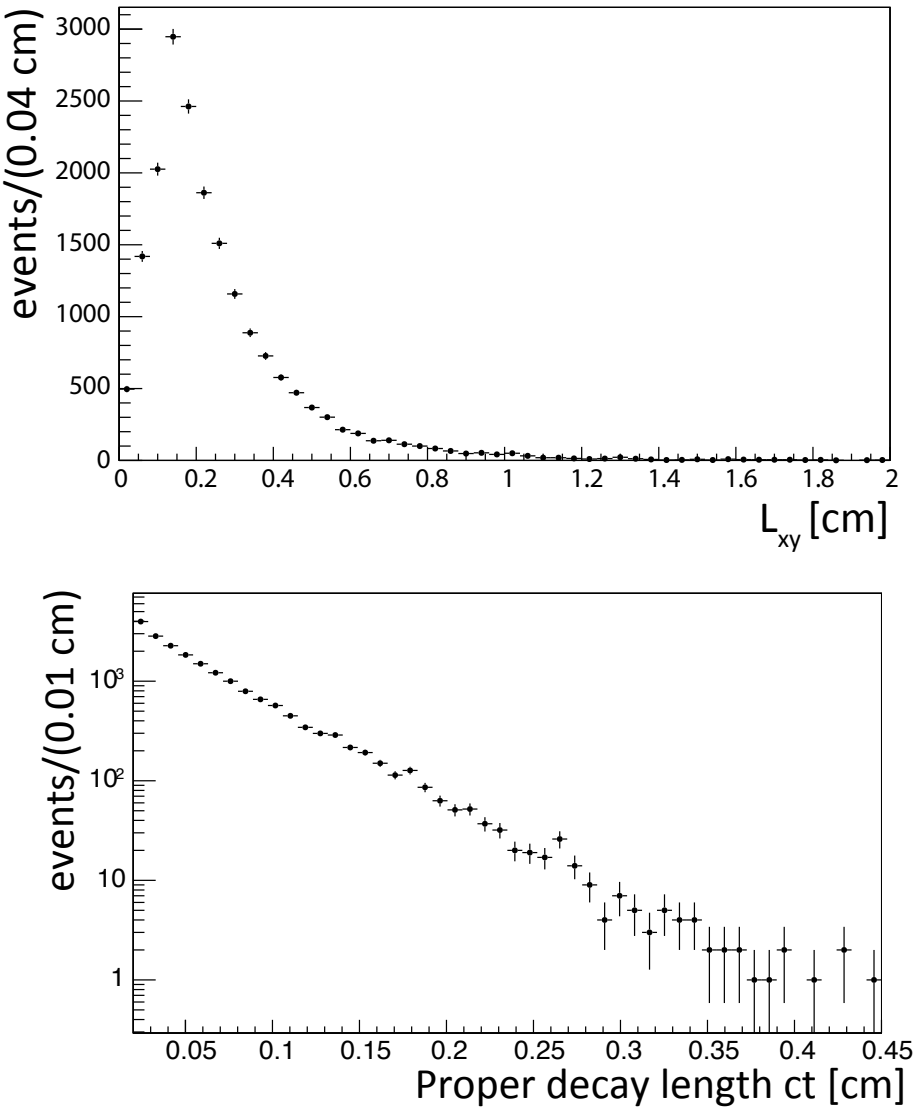

Figure 5.3: Distributions of the projected decay length L_{xy} (top), and the proper decay length (bottom) into the xy-plane (defined in the text).

Measurement of the resolution parameters

The B_s^0 prompt decays are needed to calculate the proper time resolution in data, since the effects of the resolution can be measured in them. Unfortunately, a cut on ct in the region around zero is implemented in the displaced trigger used for the analysis, as explained in Section 4.3. The cut around zero eliminates the possibility of calculating the resolution with the prompt events. The barrel triggers without the ct cut around zero are selected to evaluate the resolution effect on data.

A two-dimensional fit, depending on the invariant mass M and the time ct of the B_s^0 meson candidates, is used to calculate the parameters of the resolution function

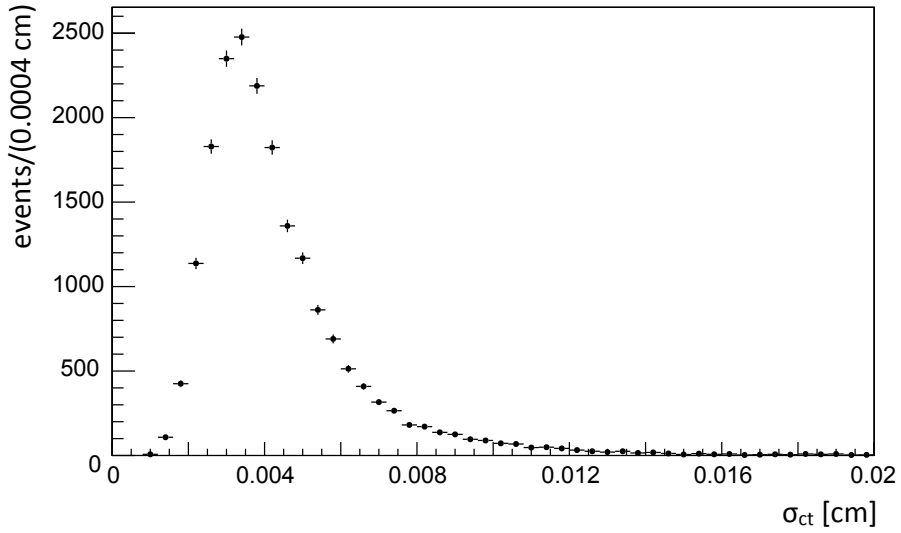

Figure 5.4: Proper decay length error distribution σ_t.

$G(t;\kappa,\sigma_t)$. This analysis assumes that the resolution function valid for the two-dimensional fit is valid in the nominal fit as well. The following likelihood function is used:

$$\begin{aligned} L_{2D} = N\ PDF_S(2D)(ct,M)\epsilon(ct) \otimes G(ct;\kappa,\sigma_t) \\ +B\ PDF_B(2D)(ct,M) \otimes R(ct;\mu_{br},\sigma_{b1},\sigma_{b2}), \end{aligned} \tag{5.14}$$

where PDF_S is the probability density function for the signal distribution, PDF_B is the probability density function for the background distributions, G is the gaussian per event resolution, R is the double gaussian resolution function used for the background events, N is the number of signal events, and B is the number of background events.

The PDF_S is defined as follows:

- The B_s^0 mass PDF is parameterized with two Gaussian functions.
- The ct PDF is parameterized with an exponential function, convoluted with the Gaussian resolution function of the proper decay length $G(t;\kappa,\sigma_t)$ which includes the uncertainty for each individual event σ_t scaled by a factor κ. The gaussian resolution function is the same used in the nominal fit.

The PDF_B is defined as follows:

- The distribution function for the mass of the background events is fitted with a first order polynomial.

Table 5.1: Functional form of the $B_s^0 \to J/\psi\ \phi$ mass PDF for Eq. 5.14.

Component	PDF	Parameter
signal	$Ae^{-\frac{(x-\mu_1)^2}{2\sigma_1}} + (1-A)e^{-\frac{(x-\mu_2)^2}{2\sigma_2}}$	$\mu_1, \sigma_1, \mu_2, \sigma_2, A$
background	$a_0 + a_1 x$	a_0, a_1

Table 5.2: Functional form of the $B_s^0 \to J/\psi\ \phi\ ct$ PDF for Eq. 5.14.

Component	PDF	Parameter
signal	$e^{-\frac{(ct)^2}{c\tau}} \bigotimes G(ct; \kappa, \sigma_t)$	τ, κ, σ_t
background	$(fe^{-ct/(c\tau_s)} + (1-f)e^{-ct/(c\tau_l)}) \bigotimes R(ct; \mu_{br}, \sigma_{b1}, \sigma_{b2})$	$f, \tau_s, \tau_l, \mu_{br}, \sigma_{b1}, \sigma_{b2}$

- The proper decay length PDF for the background events is the same as Eq. 5.8 used in the nominal fit, convoluted with a double gaussian resolution function, $R(ct; \mu_{br}, \sigma_{b1}, \sigma_{b2})$, that share the same mean μ_{br}.

In Table 5.2.1 and Table 5.2.1 are shown the functional forms of the B_s^0 mass and ct PDFs respectively.

The two-dimensional fit, Eq. 5.14, is performed in a similar way to the nominal five-dimensional fit, explained in Section 5.5, in order to avoid introducing additional systematic uncertainties. To include the events around zero, the ct fitting range covers from -0.02 to 0.3 cm. The fit is performed in several steps:

1. The PDF_B is fitted to the sidebands.
2. All the parameters of the PDF backgrounds are fixed based on the results of the fit. Table 5.3 shows the value of the parameters resulting from the fit.
3. The full two-dimensional fit, L_{2D}, is performed on the B_s^0 candidates in a mass range of 5.24 to 5.49 GeV/c^2, and a ct range of -0.02 to 0.3 cm.

The per-event resolution scale factor and the background resolution terms from the results, are used as direct input in the nominal fit. The fit results are presented in Table 5.4, and the plots are shown in Fig. 5.5.

Table 5.3: Fitted parameters of the ct PDF in the two-dimensional fit to the sidebands region $[5.24 < M < 5.28]$ GeV/c^2 and $[5.45 < M < 5.49]$ GeV/c^2.

Output from the fit on the sidebands	value [cm]
μ_{br}	$(-2.05 \pm 0.25) \times 10^{-3}$
σ_{b1}	$(3.81 \pm 0.10) \times 10^{-3}$
σ_{b2}	$(1.09 \pm 0.08) \times 10^{-2}$
Long lived backgrounds $c\tau_l$	$(4.23 \pm 0.27) \times 10^{-2}$
Short lived backgrounds $c\tau_s$	$(2.32 \pm 0.29) \times 10^{-3}$

Table 5.4: Fitted parameters in the two-dimensional fit to the full mass range for the B_s^0 candidates $[5.24, 5.49]$ GeV/c^2.

Output from the fit on full mass range	value
Scale-factor κ	1.49 ± 0.11
Number of signal events N	$4\,961.4 \pm 93.6$
Number of background events B	$25\,040.3 \pm 169.8$

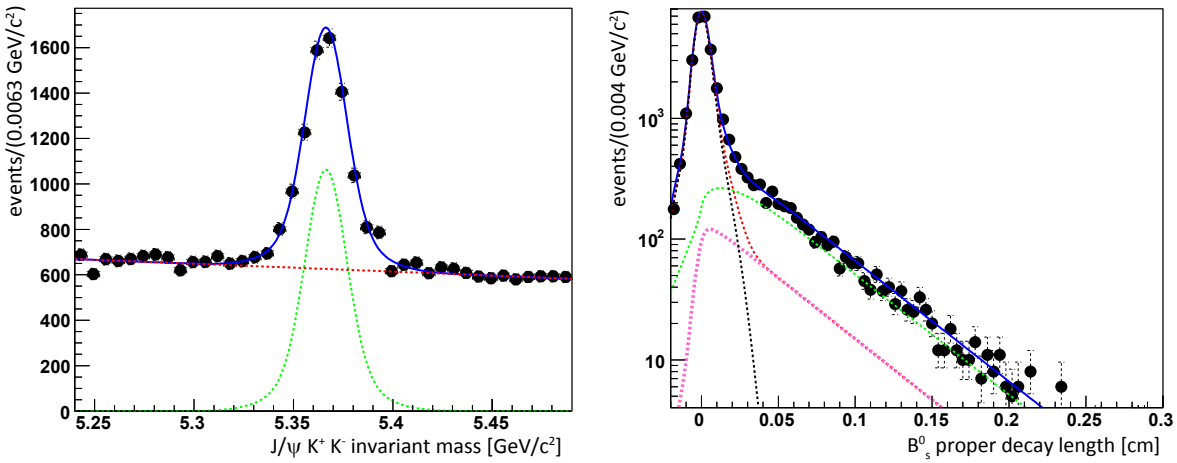

Figure 5.5: Results from the two-dimensional maximum likelihood fit for the channel $B_s^0 \to J/\psi\ \phi$ using data taken with the barrel triggers. Left: $J/\psi\ K^+K^-$ invariant mass. Right: B_s^0 candidates proper decay length. The black points are the data, the blue lines are the fits, the green dashed curves are the signal model, and the dashed red curves are the background model. The magenta dashed curve is the long-lived ct ($c\tau_l$) background, and the black dashed curve is the short-lived ct ($c\tau_s$) background.

5.2.2 Angular resolution

The angles $\cos\theta, \cos\psi$, and φ are smeared with a Gaussian function to account for the angular resolutions. The full signal MC sample is used to calculated the resolution. In Table 5.5 are shown the values of the standard deviation of the gaussian. Similarly

Table 5.5: Angular resolution smeared with a gaussian of the three physical angles $\cos\theta$, $\cos\psi$, φ. The present values are the standard deviation σ of the gaussians.

	$\cos\theta$	$\cos\psi$	φ [rad]
σ	0.009	0.009	0.011

to the analysis presented in [61], the uncertainties on the angles are very small. Therefore, the angular resolutions are not included in the fit.

5.3 Efficiencies

The theoretically expected distributions of the main five observables are distorted due to the geometry of the detector and the selection cuts used to reconstruct the event candidates. Accurate corrections to the distortions are important to avoid systematic biases on the estimation of the physical parameters.

The study of the efficiency distortions is performed using $B_s^0 \to J/\psi\,\phi \to \mu^+\mu^- K^+ K^-$ simulations, explained in Section 4.2, but without applying the cut on the J/ψ displaced distance, and the samples use the full $B_s^0 \to J/\psi\ \phi$ candidates mass range of [5.20, 5.60] GeV/c^2. The efficiency correction term, ϵ, depends on the observables ct, $\cos\theta$, $\cos\psi$, and φ, and compensates for the distortion due to geometry of the detector (detector acceptance), trigger selection, and event selection. This analysis assumes the factorization of the efficiency in the following way:

$$\epsilon(ct, \cos\theta, \cos\psi, \varphi) = \epsilon(ct) \cdot \epsilon(\cos\theta, \cos\psi, \varphi). \tag{5.15}$$

Correlation studies are performed to quantify the relation among the variables. For these studies the signal simulation sample with difference in partial widths $\Delta\Gamma_s$ equal to 10% is used. The resulting values from the correlation are shown in Table 5.6.

There is a small correlation (15%) between the angles $\cos\psi$ and φ, and it is considered as a possible systematic effect and discussed in Section 5.6.3. On the other hand, the results do not show correlations between the time and angular variables.

Table 5.6: Correlation among the observables involved in the fit.

Variables	Correlation coefficient
$\cos\theta - \cos\psi$	0.01
$\cos\theta - \varphi$	0.01
$\cos\psi - \varphi$	-0.15
$ct - \varphi$	0.02
$ct - \cos\psi$	-0.02
$ct - \cos\theta$	-0.02

5.3.1 Decay length efficiency

The efficiency functions to be included in the multiple likelihood are chosen using the $B_s^0 \to J/\psi\,\phi$ simulation sample with $\Delta\Gamma_s = 0$. The signal simulation selected ensures that the angular and proper decay length efficiencies can be factorized and analyzed without introducing systematic uncertainties [60].

The efficiency depending on the decay length $\epsilon(ct)$ is calculated dividing the ct distributions of the fully reconstructed events by the ct distributions of the selected events produced at generation level (without the detector simulation). The distribution of the efficiency is shown in Fig. 5.6.

The efficiency distribution is assumed flat for the range of $ct > 0.02$ cm and $ct < 0.3$ cm, implying there is no correlation between the efficiency and the decay length in that range. To avoid dealing with components that could influence the ct measurement, the ct efficiency is parameterized with a straight line after applying a cut on $ct > 0.02$ cm at selection level. The distribution is fitted with the following curve:

$$\epsilon(ct) = k_1 + k_2 ct, \tag{5.16}$$

where k_n are the fit coefficients. The variations of the fitted values within their errors are treated as systematic uncertainties, and they are discussed in Section 5.6.3.

One can see that the first bins of the curve, ct range [0, 0.02] cm, show a dependence between the efficiency and the proper decay length. This curve, named turn-on curve, is produced due to the significance decay cut applied at trigger level and at the events selection, motivating the use of the ct cut.

5.3.2 Angular efficiency

In a similar way to the calculation of the ct efficiency, each angular efficiency curve is calculated dividing the angular distributions of the fully reconstructed events by

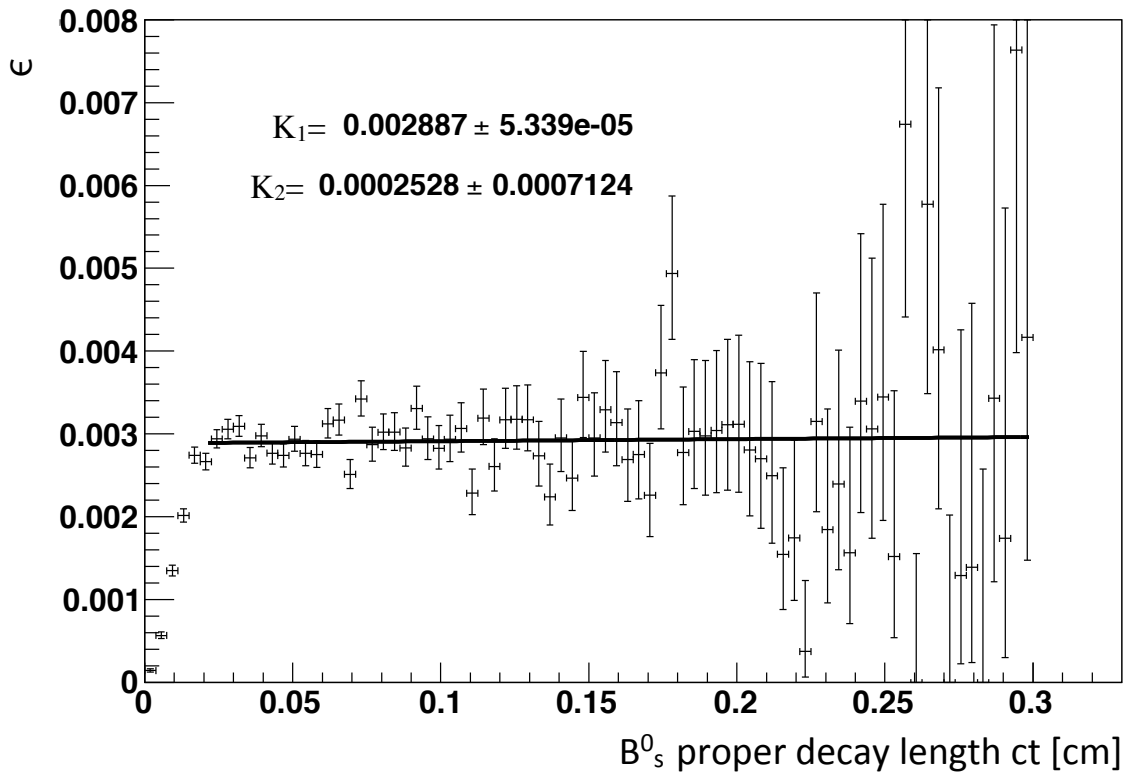

Figure 5.6: Distribution of the efficiency as a function of the decay length using the simulation $B_s^0 \to J/\psi\ \phi \to \mu^+\mu^- K^+ K^-$. The straight line is a fit.

the angular distributions of the selected events produced at generation level. To parameterize the curve, different distribution functions are tested. In the end, a single angular parameterization is done using a set of Legendre polynomials. The efficiency plots for the three angular variables are shown in Fig. 5.7.

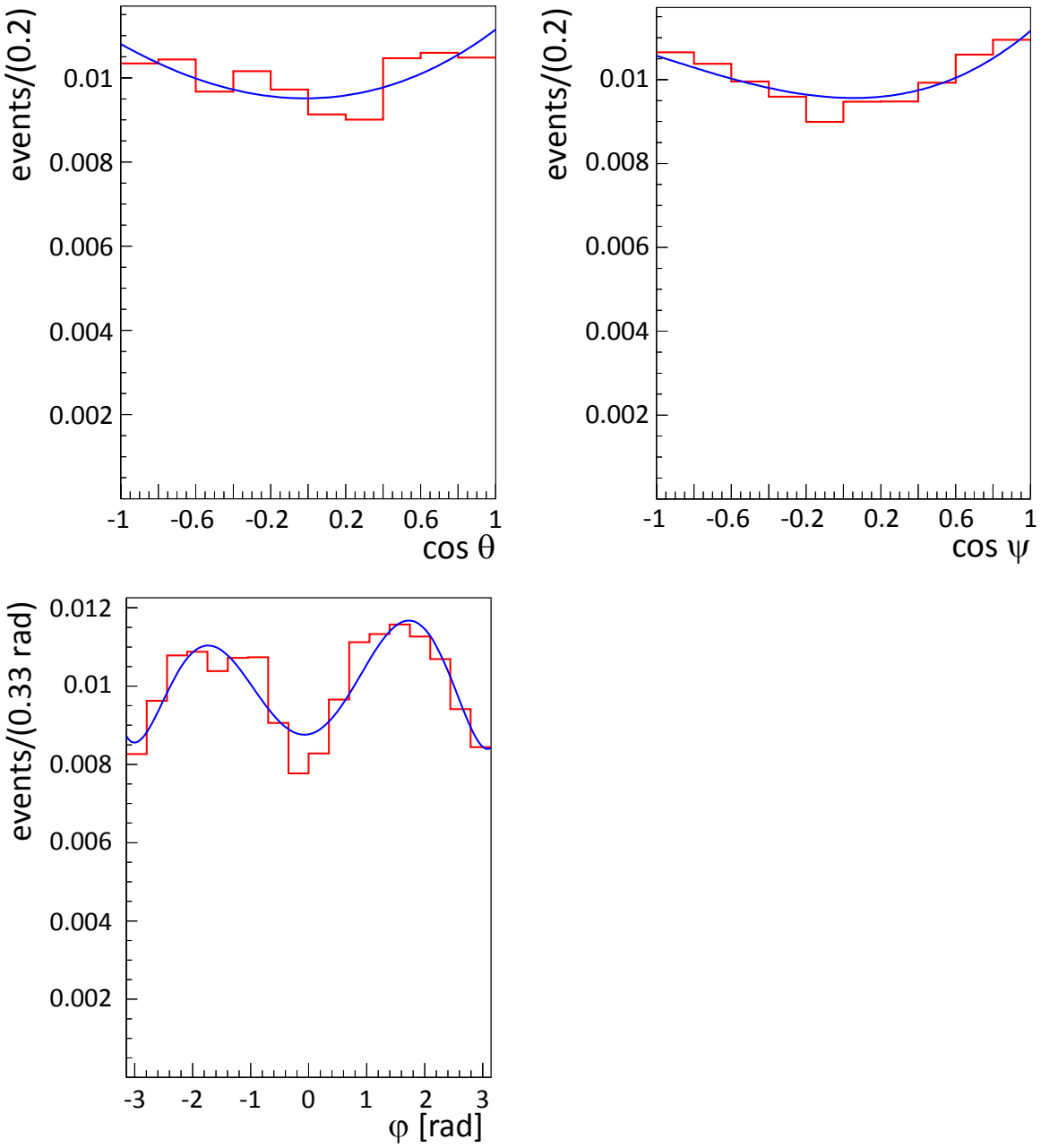

Figure 5.7: Angular distribution of the efficiencies: $\cos\theta$ (top left), $\cos\psi$ (top right), and φ (bottom). The red histograms are the simulated distributions, and the blue lines are the fits.

5.4 Validation of the probability density functions

As shown in Eq. 5.3, the full PDF description includes the signal and the background components. A series of validations using simulations are performed to ensure that the PDFs are defined correctly, and to determine possible bias. First, the theoretical model is validated, and afterward the full model, including the signal and background, is checked.

5.4.1 Validation of the signal model

The first validation test consist in fitting on simulations at generation levels, without the detector simulation, to ensure that the theoretical descriptions of PDFs (presented in Eq. 5.4) are correct. This description does not include the efficiencies or the backgrounds. The signal MC simulation sample contains approximately five millions events at generator level.

The multiple likelihood fit depending on the four observables (ct, $\cos\psi$, φ, $\cos\psi$) is performed. The result from the fit, and the parameter values used for the signal MC are shown in Table 5.7, and the fitted distributions of the observables are shown in Fig. 5.8. The output values measured from the fit are consistent with the parameters values used to generate the MC sample.

Table 5.7: Results obtained from the signal fit (Eq. 5.4), and the parameters values used for generating the signal MC. The signal MC sample used contains approximately five million events at generator levels.

Variable	Fit output	Statistical error	MC value
$\lvert A_0\rvert^2$	0.59966	0.00040	0.6006
$\lvert A_\perp\rvert^2$	0.16007	0.00057	0.1593
$\delta_{\lvert\rvert}$	2.4820	0.0032	2.50
$\Delta\Gamma_s$ (cm^{-1})	0.0379	0.0594	0
$c\tau_s$ (cm)	0.044012	0.000044	0.04399

The second validation test on the signal model is done using pseudo-experiments (toy Monte Carlo studies). The pseudo-experiments are performed generating data according to a specified PDF model, and later the maximum likelihood fit is complete on that data. The idea is to compare the values obtained from the fit, with the parameters used for generating the MC sample. To do the comparison the pull (P_x)

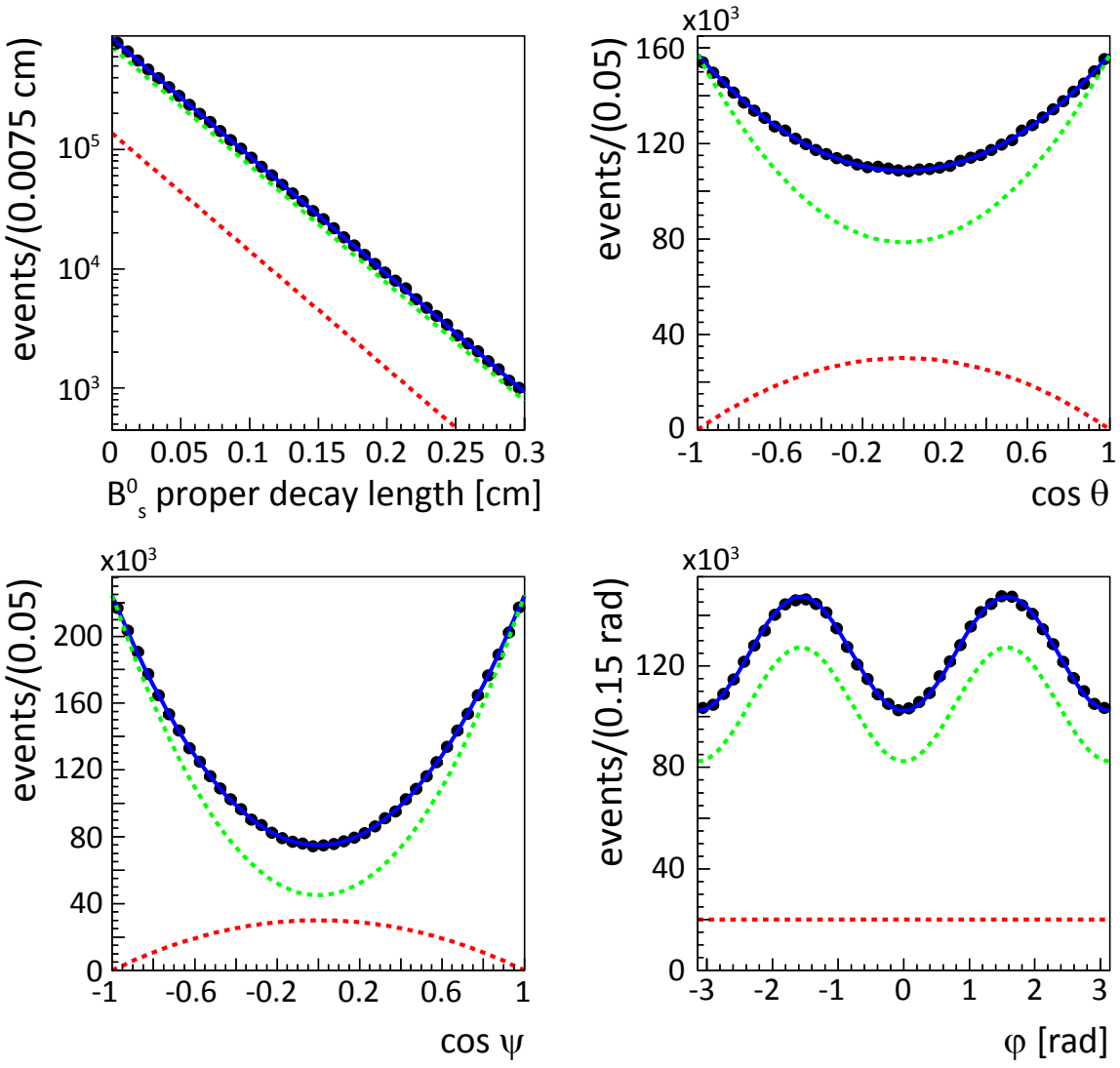

Figure 5.8: Distributions of the fit observables (ct, $\cos\theta$, $\cos\psi$, φ) using only signal simulation at generator level, without any distortion from the detector or selection cuts. The solid lines are the fits, the dashed red lines are the CP odd components, the dashed green lines are the CP even components.

is calculated and defined as:

$$P_x = \frac{x_{fit} - x_{MC}}{\sigma_x}, \tag{5.17}$$

being x_{fit} the parameter obtained by the fit, x_{MC} the value used for generating the MC sample, and σ_x the error associated to the fitted value. Moreover, the distributions of the pulls are fitted with a Gaussian. A result is said to be un-biased if the mean is zero and the width of the Gaussian is one.

One thousand pseudo-experiments are completed to validate the signal model,

each of them with a generated dataset of 14 000 events. In Figure 5.9 are shown the pull distribution plots for the variables α, and the values of the fitted mean and sigma can be seen in Table 5.8.

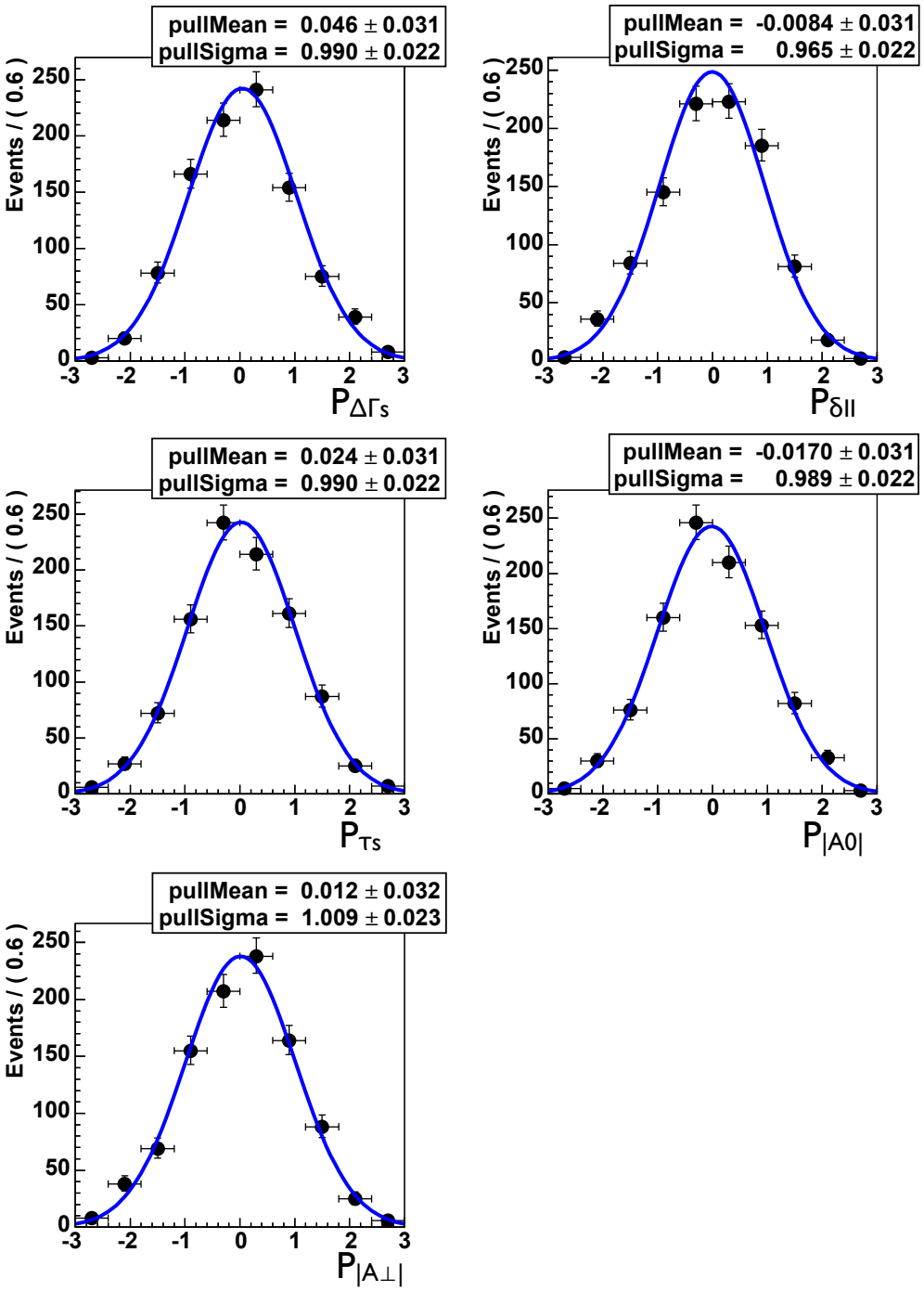

Figure 5.9: Distribution of the pulls of the signal PDF with 1 000 pseudo-experiments.

Table 5.8: Mean and width values of the Gaussians that fit the pull distribution of the pseudo-experiments for each of the parameters of interest for the signal PDF.

Pull (P)	$\|A_0\|^2$	$\|A_\perp\|^2$	$\delta_\|$	$c\tau_s$	$\Delta\Gamma_s$
mean	-0.0170 ± 0.031	0.012 ± 0.032	-0.008 ± 0.031	0.024 ± 0.031	0.046 ± 0.031
width	0.989 ± 0.022	1.009 ± 0.023	0.965 ± 0.022	0.990 ± 0.022	0.990 ± 0.022

5.4.2 Validation of the fit at reconstructed level

Analog to the signal model validation, two methods are used to validate the full PDF model of Eq. 5.3. The first method is to test the full fit using the MC simulations discussed in Section 4.2. The MC samples used for simulating the backgrounds are the $B_s^0 \to J/\psi\, X \to \mu^+\mu^- X$, without including $B_s^0 \to J/\psi\, \phi \to \mu^+\mu^- K^+K^-$, $B^0 \to J/\psi\, X \to \mu^+\mu^- X$, and $B^+ \to J/\psi\, X \to \mu^+\mu^- X$. The signal sample is the sample $B_s^0 \to J/\psi\, \phi \to \mu^+\mu^- K^+K^-$. The samples are combined to increase statistics, and to achieve a signal-background ratio as similar as possible to the real data.

The multiple likelihood fit is performed on the simulated samples using the same methodology as in Section 5.5. First, the multiple likelihood fit $\mathcal{P}_{background}(\Theta, t, M)$, Eq. 5.7, is implemented on the sidebands region. Figure 5.10 shows the projection of the angular distributions fit on the sidebands. Then, all the results from the sidebands fit are fixed in the full model. The full fit, Eq. 5.3, is performed in the full B_s^0 mass range, and the results are presented in Table 5.9.

Table 5.9: Results obtained from the nominal fit on MC simulations at reconstruction level. In the table are shown as well the parameter values used for generating the signal MC.

Variable	Fit output	Statistical error	MC value
$\|A_0\|^2$	0.606	0.013	0.6006
$\|A_\perp\|^2$	0.170	0.017	0.1593
$\delta_\|$	2.76	0.16	2.50
$\Delta\Gamma_s$ (cm^{-1})	1.16	1.37	0
$c\tau_s$ (cm)	0.0443	0.0010	0.04399

The results show that the only variable that has more than one sigma deviation from the expected value is the variable $\delta_\|$. The full projection distribution of the angles on the full mass range can be seen in Fig. 5.11.

Pseudo-experiments are the second method to investigate the potential biases in the nominal PDF. In the toy MC the data samples are generated according to the

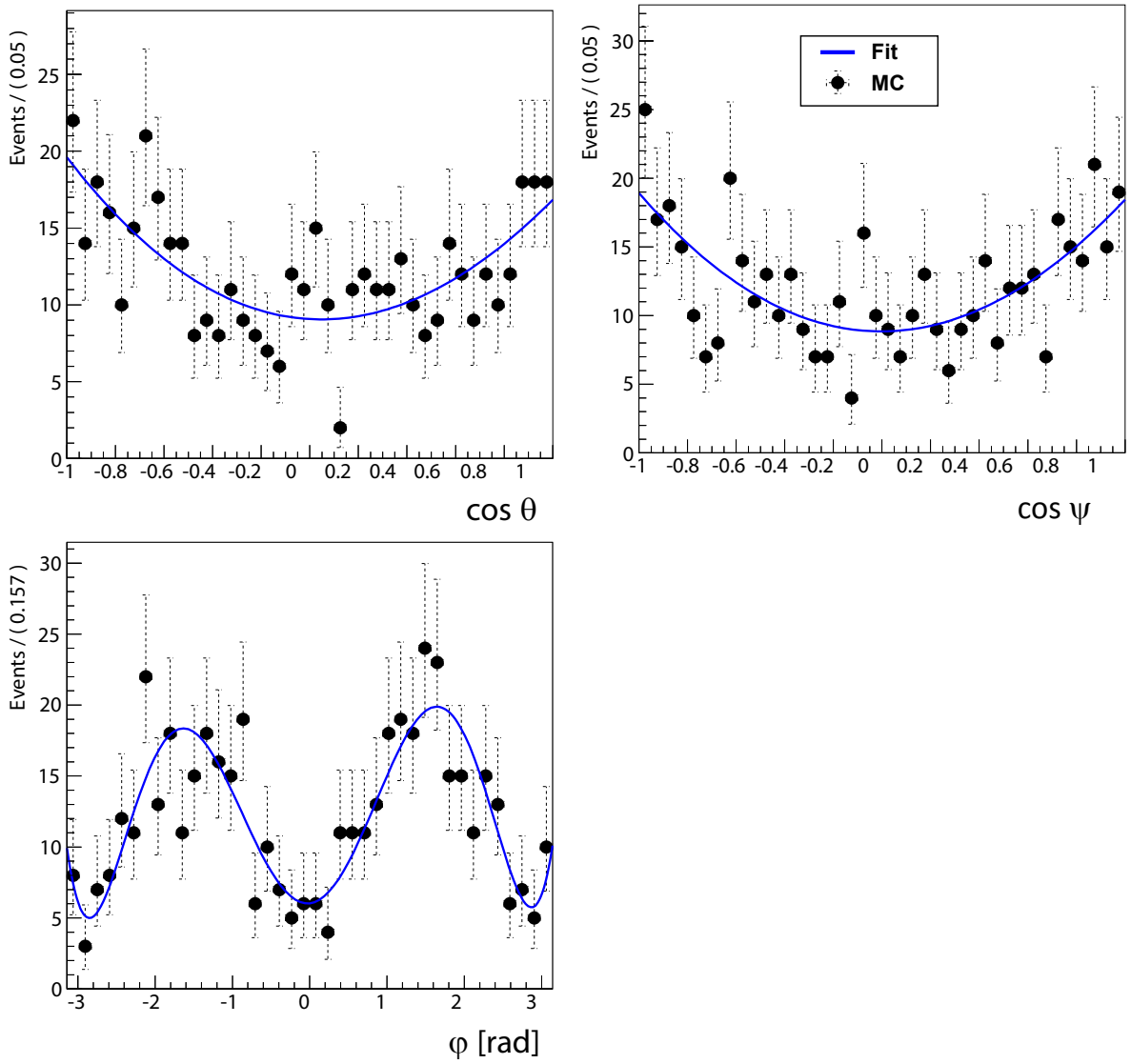

Figure 5.10: $\cos\theta$ (top left), $\cos\psi$ (top right) and φ (bottom) distribution of the MC samples for the sidebands events: the blue lines are the fit, and the points are the MC distributions.

nominal PDF shown in Eq. 5.3. Then, the maximum likelihood fit is performed on the generated data, as explained in Section 5.5.

The pull distributions, Eq. 5.17, are generated for each parameter to verify the bias on them. Each pull distribution is fitted with a Gaussian distribution, and their mean and width are analyzed. The number of events in the data samples generated (19 200 events in total) is the same as the number of candidate events present in the real data, including signal and background. The number of experiments is 1 250. In Fig. 5.12 are presented the pull distributions for each of the parameters of interest, including the values of the mean and width of the pulls.

Finally, 1 250 pseudo-experiments are performed of 19 200 events in total (signal and background). The plots with the pull distributions for the involved variables are shown in Fig. 5.12, and the results from the pseudo-experiments are presented in Table 5.10.

Table 5.10: Pseudo-experiment results of the full model PDF, with 1 250 experiments and the number of events (19 200) equivalent to the number of events in data

Pull (P)	$\|A_0\|^2$	$\|A_\perp\|^2$	$\delta_{\|\|}$	$c\tau_s$	$\Delta\Gamma_s$
mean	-0.046 ± 0.028	0.014 ± 0.029	0.101 ± 0.028	-0.063 ± 0.029	-0.007 ± 0.029
sigma	1.001 ± 0.020	1.018 ± 0.020	1.002 ± 0.020	1.029 ± 0.021	1.012 ± 0.020

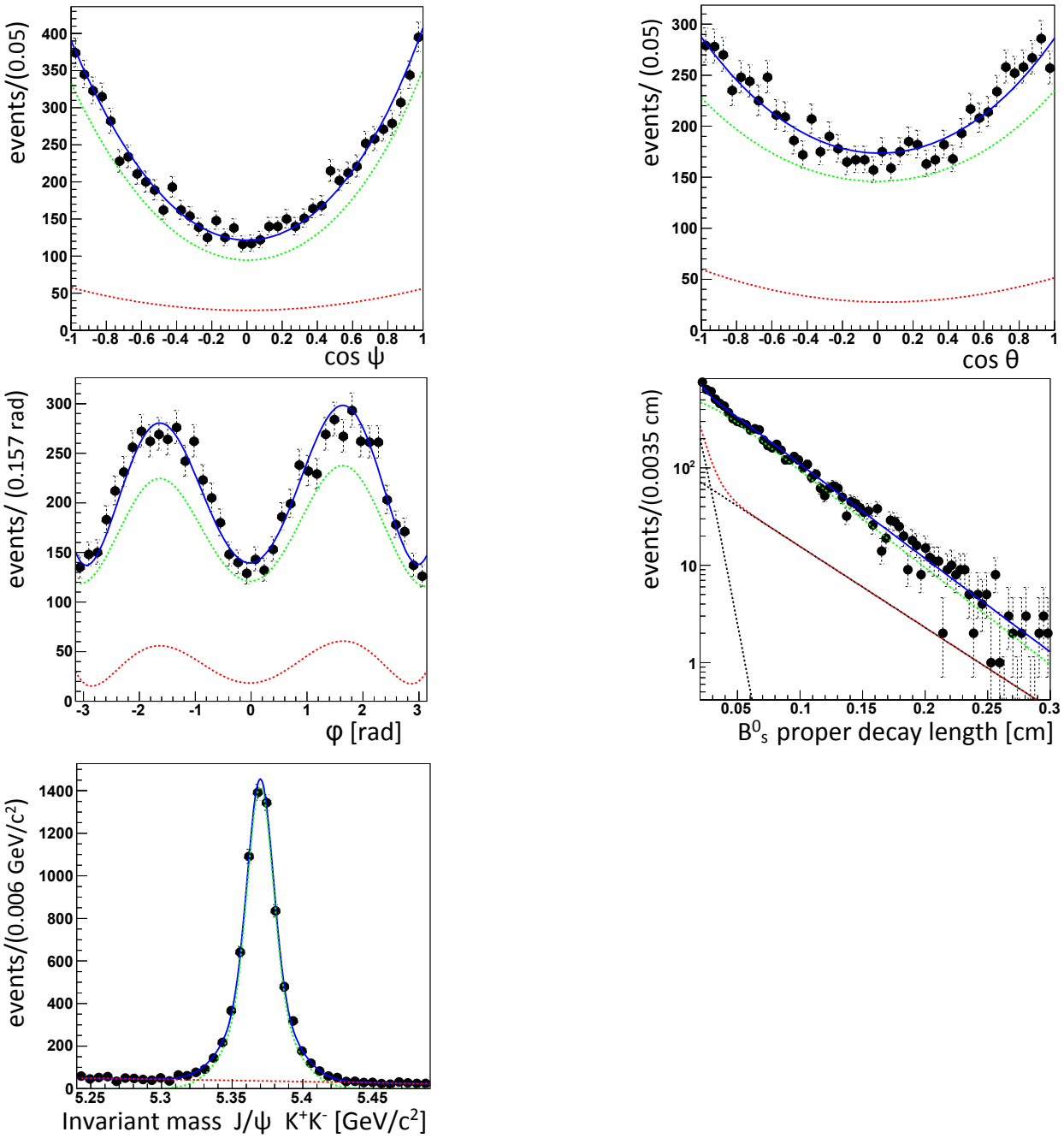

Figure 5.11: Results of the five-dimensional maximum likelihood fit on the MC samples. The upper two figures are $\cos\psi$ (top left), and $\cos\theta$ (top right). The middle figures are the distributions of the angle φ (middle left), and the proper decay length (middle right). The lowermost figure is the $B_s^0 \to J/\psi\ \phi \to \mu^+\mu^- K^+ K^-$ invariant mass distribution. The solid lines are the fits, the dashed green lines are the signal components, the dashed red lines are the background components, the dashed black lines present in the proper decay length distribution are the long-lived and short-lived background components, and the points are the MC distributions.

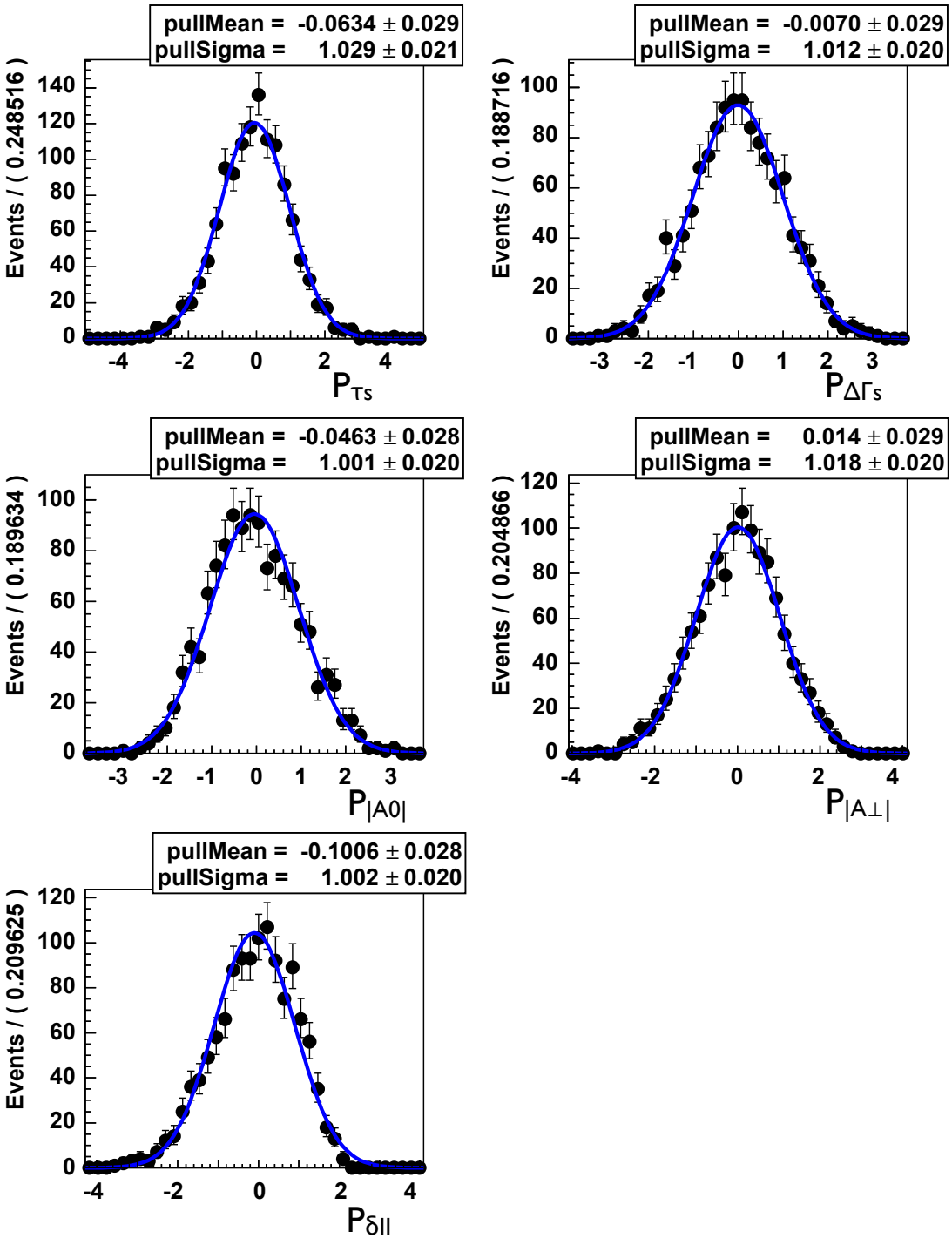

Figure 5.12: Pseudo-experiment pulls of the full model PDF, with 1 250 experiments and the number of events (19 200) equivalent to the number of events in data. The black points are the data generated, and the blue line is the fitted Gaussian.

5.5 Likelihood maximization

After selecting 19 200 $B_s^0 \to J/\psi\ \phi \to \mu^+\mu^- K^+K^-$ candidate events, and validating the full likelihood function PDFs, an unbinned maximum likelihood fit is performed. Five observables are fitted simultaneously namely the invariant mass of the B_s^0 candidate, the proper decay length, $\cos\theta$, φ and $\cos\psi$. This analysis assumes the mixing phase ϕ_s to be equal to zero. The physical parameters α=$\{\Delta\Gamma_s$, Γ_s, $|A_\perp|^2$, $|A_0|^2$, δ_0, and $\delta_{||}\}$ are obtained from the multi-dimensional fit. The fit is performed in several steps.

First, a one-dimensional mass fit is performed on the B_s^0 candidates invariant mass range [5.24, 5.49] GeV/c^2. The mean of the two-Gaussians, and the smaller width of the two Gaussians is fixed. In Table 5.11 are shown the values for the mean of the invariant mass peak, and the width fixed in the full model.

Table 5.11: One-dimensional fit on the invariant mass.

Parameter	Fit results
mean of the two Gaussians GeV/c^2	5.36688 ± 0.00013
sigma of the narrowest Gaussian GeV/c^2	$(9.78 \pm 0.35) \times 10^{-3}$

Second, the data sidebands are fitted with $\mathcal{P}_{background}(\Theta, t, M)$. The parameters that define the angles distributions are extracted from the fit and fixed in the full model. In Fig. 5.13 are represented the projection of the angles $\cos\psi$, φ, and $\cos\psi$ on the sideband regions.

In the final step, the extended likelihood $L(\alpha)$ fit is performed on data. All the parameters are left floating except the mean, and the smaller width of the two Gaussians defining the invariant mass, the angular distributions on the background sidebands, and the proper decay length resolution scale factor (discussed in Section 5.2.1).

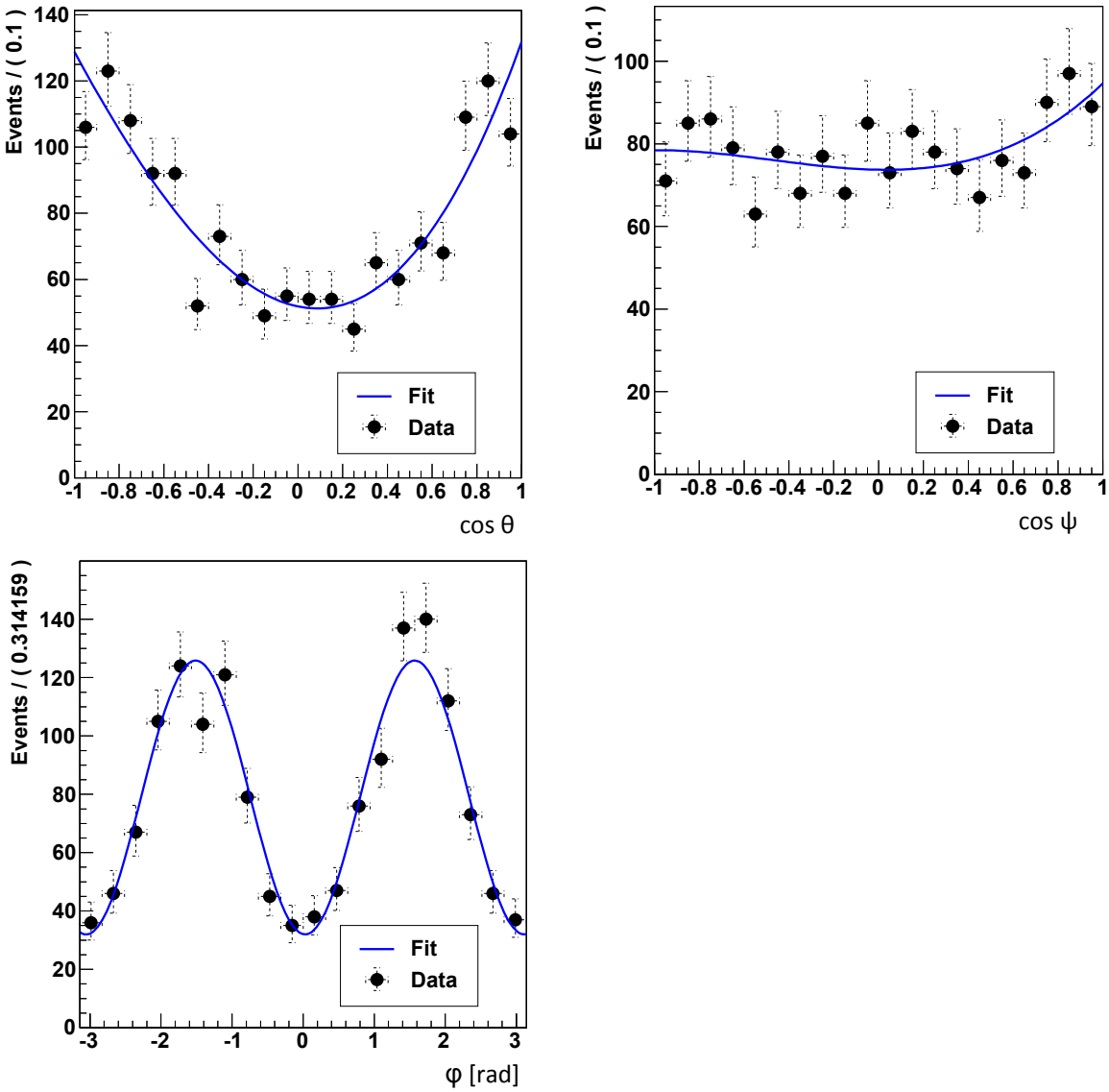

Figure 5.13: $\cos\theta$ (top left), $\cos\psi$ (top right) and φ (bottom) distributions for the sideband events. The blue line is the fit, and the points are the data.

5.5.1 Results from the full probability density function

Figures 5.14, 5.15, and 5.16 show the invariant mass, the proper decay length, and angular the distributions. In Table 5.12 are presented the results from the full fit using the 5 fb^{-1} of data taken during the 2011 CMS run period. From the 19 200 candidates events, the measured signal yield is 14 310 $\pm$ 138 events, with a mass mean of 5 366.8 $\pm$ 0.1 MeV/c^2. This number is comparable with the world average measurement given by the Particle Data Group [12] 5 366.77 $\pm$ 0.24 MeV/c^2.

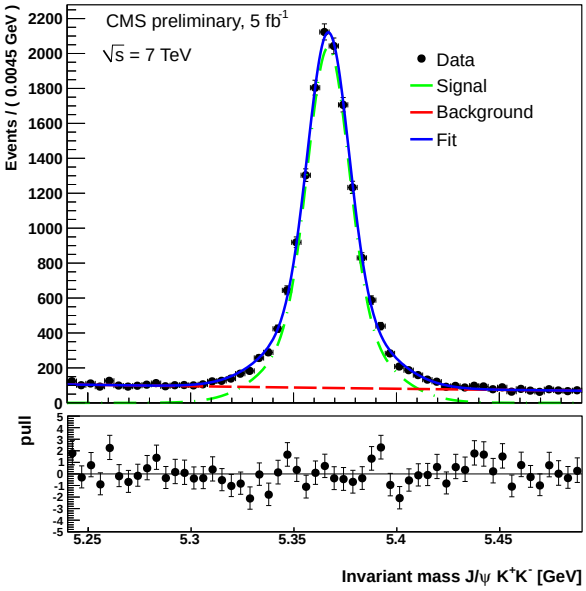

Figure 5.14: Distribution showing the B_s^0 peak from the five-dimensional maximum likelihood fit on data, where the M(K^-K^+) is center with the $\phi(1020)$ mass. The blue line is the fit; the green line is the signal model; and the red line is the background model.

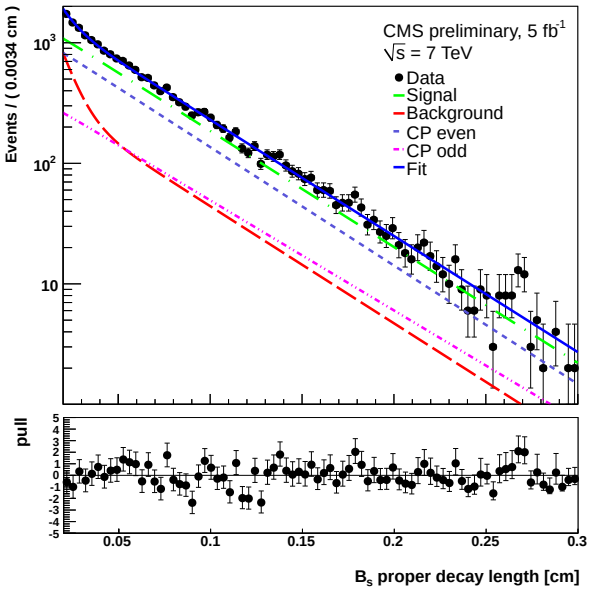

Figure 5.15: Distribution of the proper decay length from the five-dimensional maximum likelihood fit on data. The solid blue line is the fitted function; the black points are the data; the green line is the signal model; the red line is the background model; the magenta dash line is the CP odd component; the purple dash line is the CP even component.

Table 5.12: Results from the multiple likelihood fit on data.

Variable	Fit output	Statistical error
$\|A_0\|^2$	0.528	0.010
$\|A_\perp\|^2$	0.251	0.013
$\delta_{\|\|}$	2.79	0.14
$\Delta\Gamma_s$ (ps^{-1})	0.048	0.024
$c\tau_s$ (cm)	0.0458	0.00058
τ_s (ps)	1.527	0.020
Number of signal events	14 456	1 39
Number of background events	4 742	99

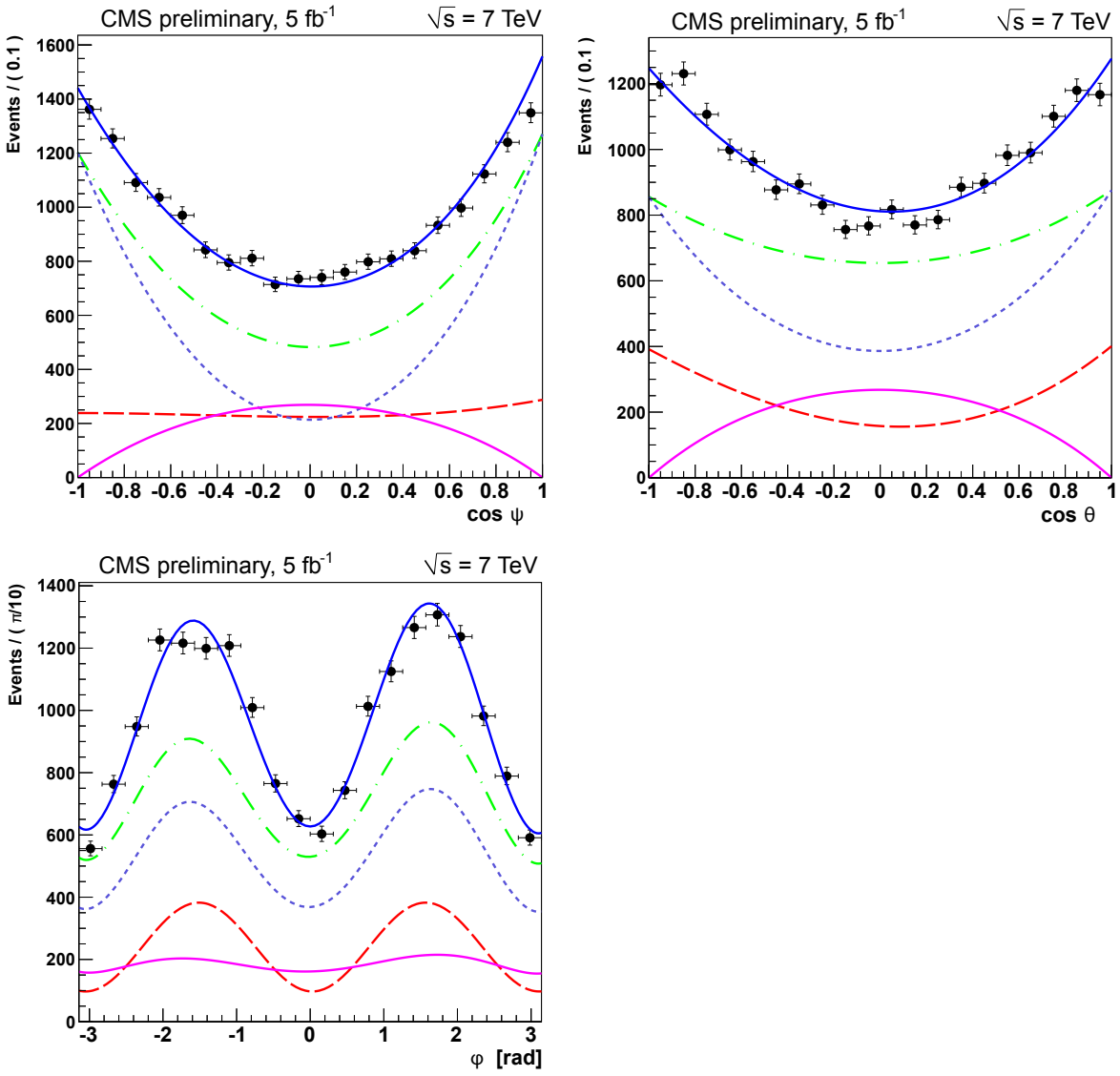

Figure 5.16: Five-dimensional maximum likelihood fit on data. The upper two figures are the distributions of the angular variables $\cos\psi$ (top left), and $\cos\theta$ (top right). The lower figure is the distribution of the angle φ (bottom). The solid blue lines are the fit; the green lines are the signal; the red lines are the background; the magenta lines are the CP odd component; and the purple dash lines are the CP even component.

5.6 Systematics uncertainties

Several sources of systematic uncertainties are considered by testing the various assumptions made in the nominal fit model and the possible systematic errors associated with the fit procedure.

Table 5.13 summarizes all the systematic uncertainties considered for this analysis, which are further explained in the following sections. The parameterization of the distribution of angular efficiency is the biggest contribution to the uncertainty of the main physical parameter measured $\Delta\Gamma_s$. The full systematic uncertainty, the quadratic sum of all the errors, is quoted as systematic uncertainty in the final result of this dissertation.

Table 5.13: Systematic uncertainties on the full fit for 5.01 fb^{-1} of data at 7 TeV center of mass.

Systematic	$\Delta\Gamma_s$ (ps^{-1})	$c\tau_s$ (cm)	$\|A_0\|^2$	$\|A_\perp\|^2$	$\delta_{\|\|}$
Signal PDF modeling					
Time resolution	0.00170	0.00006	0.0007	0.0000	0.007
Mass model	0.00072	0.00012	0.0022	0.0006	0.039
ϕ_s approximation	0.00000	0.00001	0.0000	0.0000	0.002
S-wave assumption	0.00109	0.00001	0.0130	0.0066	0.056
Background PDF					
Lifetime model	0.00040	0.00000	0.0001	0.0002	0.003
Mass model	0.00019	0.00000	0.0000	0.0001	0.003
Angular model	0.00175	0.00003	0.0001	0.0064	0.161
Peaking B^0 background	0.00025	0.00006	0.0002	0.0022	0.050
Efficiencies					
Proper decay length parameters	0.00000	0.00005	0.0000	0.0000	0.000
shape	0.00181	0.00014	0.0005	0.0007	0.001
Angular parameters	0.00019	0.00002	0.0057	0.0055	0.037
shapes	0.00063	0.00003	0.0021	0.0086	0.007
Full PDF bias	0.00000	0.00004	0.0004	0.0000	0.014
Quadratic sum	0.00341	0.00022	0.0146	0.0140	0.187

Two methods are used for measuring the systematic uncertainties. One method is based on performing several pseudo-experiments to investigate the PDF models used for fitting the data, in addition to analyzing possible biases in the selection and fitting procedure of the data. The second method is performed varying the nominal fit to compute how much the variations on the fitting model affects the final result, and then accounting the difference between the results from the nominal fit and the modified fit as systematic uncertainties.

5.6.1 PDF signal model

The bias associated to each of the components of the PDF signal model, Eq. 5.6, are calculated. The PDF signal model uncertainties are separated as follows:

- Mass model

  The B_s^0 mass peak can be parameterized with different PDF shapes. The uncertainty due to the modeling of the B_s^0 mass is obtained considering a model with a different mass shape. The signal mass PDF is changed using a three-Gaussian function instead of the two-Gaussian function. The differences of the parameters of the fit with respect to the nominal fit are considered the systematic uncertainty per physics parameter α.

- Proper decay length resolution

  The trigger path used to calculate the proper decay length resolution is not the same as the one used to perform the analysis. Ideally, a data sample without any decay length cut would be needed to calculate the scale factor. Therefore, as explained in Section 5.1.3, the proper decay length resolution is calculated using data taken with the barrel trigger without a decay length cut on the B_s^0 candidates, and with a pseudo-rapidity range that covers only the barrel region ($|\eta| < 1.25$). However, this analysis is performed using the displaced triggers, which cover the full pseudo-rapidity region ($|\eta| < 2.1|$). A correction for the change of triggers must be applied on the scale factor. The uncertainty of this correction induces a systematic error on the proper decay length resolution.

  The correction factor is determined using the $B_s^0 \to J/\psi\,\phi$ MC sample. Selection cuts to mimic the trigger paths are applied on the MC sample. The correction factor is calculated in the following way. First, the scale factor (SF) of the resolution is calculated in the barrel region SF_{barrel}. The scale factor obtained in this case is SF_{barrel}=1.15 $\pm$ 0.05. Then, the scale factor is calculated for the full pseudo-rapidity region $SF_{barrel+endcaps}$, with a measured value in this case of $SF_{barrel+endcaps}$=0.88 $\pm$ 0.27. Finally, the correction factor defined is the fraction $0.88/1.15 = 0.77$.

  Knowing the scale factor in data is $SF = 1.5 \pm 0.1$ for the barrel region, when applying the correction factor to the barrel results, for the full pseudorapidity region the expected scalar factor is $SF = 1.14$. The systematic uncertainty is evaluated performing 1075 pseudo-experiments with two different scale factors SF 1.14 and 1.6. The scale factor that gives the biggest difference is considered the systematic error.

- ϕ_s approximation

  To calculate the systematic uncertainty associated to the assumption of ϕ_s equal to zero, 950 pseudo-experiments are performed using ϕ_s value equal to the Standard Model value of -0.04. The mean error from the pseudo-experiments times the nominal statistical error is considered systematic uncertainty.

- S-wave assumption

  This analysis studies the $B_s^0 \to J/\psi\ \phi \to \mu^+\mu^- K^+K^-$. However, the kaon pair can be obtained through other resonant particles like $f_0(980)$ or in a non-resonant K^+K^- decay with spin-0, having an invariant mass close to the $\phi(1020)$ region [65]. These contributions can produce a flat distribution under the B_s^0 mass peak, as seen in Fig. 4.7. In order to consider the possible contributions and interference by the S-wave, the angular functions shown in Eq. 5.18 and Table 5.14 [31] must be included in the analysis, where the amplitude $|A_S|$ describes the CP odd contribution of $B_s^0 \to J/\psi\, f_0(980)$ or $B_s^0 \to J/\psi\, K^+K^-$ being $f_0(980)$ and K^+K^- in a S-wave state.

$$\begin{aligned} g_7 &= 2[1-\sin^2\theta\cos^2\phi], \\ g_8 &= \sqrt{6}\sin\psi\sin^2\theta\sin 2\phi, \\ g_9 &= \sqrt{6}\sin\psi\sin 2\theta\cos\phi, \\ g_{10} &= 4\sqrt{3}\cos\psi[1-\sin^2\theta\cos\phi]. \end{aligned} \tag{5.18}$$

Table 5.14: S-wave angular functions extension

g_i	$O_i(\alpha,t)$	
g_7	$\lvert A_S(t)\rvert^2$	$\lvert A_S(0)\rvert^2 e^{-\Gamma_s t}[\cosh(\Delta\Gamma_s t/2)+\cos\phi_s\sinh(\Delta\Gamma_s t/2)-\sin\phi_s\sin(\Delta m_s t)]$
g_8	$Re(A_S^*(t)A_{\lvert\rvert}(t))$	$\lvert A_S(0)\rvert\lvert A_{\lvert\rvert}\rvert e^{-\Gamma_s t}[-\sin(\delta_{\lvert\rvert}-\delta_S)\sin\phi_s\sinh(\Delta\Gamma_s t/2)$ $+\cos(\delta_\perp-\delta_S)\cos(\Delta m_s t)-\sin(\delta_\perp-\delta_S)\cos\phi_s\sin(\Delta m_s t)$
g_9	$Im(A_S^*(t)A_\perp(t))$	$\lvert A_S(0)\rvert\lvert A_\perp(0)\rvert e^{-\Gamma_s t}\sin(\delta_\perp-\delta_S)[\cosh(\Delta\Gamma_s t/2)$ $+\cos\phi_s\sinh(\Delta\Gamma_s t/2)-\sin\phi_s\sin(\Delta m_s t)]$
g_10	$Re(A_S^*(t)A_0(t))$	$\lvert A_S(0)\rvert\lvert A_0(0)\rvert e^{-\Gamma_s t}[-\sin(\delta_0-\delta_S)\sin\phi_s\sinh(\Delta\Gamma_s t/2)$ $+\cos(\delta_0-\delta_S)\cos(\Delta m_s t)-\sin(\delta_0-\delta_S)\cos\phi_s\sin(\Delta m_s t)]$

To study the systematic uncertainty associated to the S-wave contribution, the S-wave equations are included the full PDF description, assuming a contribution of $|A_s|^2$ of 0.03. For the study using the S-wave contributions, 366 pseudo-experiments are simulated. The mean error from the simulation times the nominal statistical error is considered systematic uncertainty.

5.6.2 Background PDF model

In order to estimate the systematic uncertainties associated to the PDF of background descriptions (Eq. 5.7) the possible uncertainties are separated in the following way:

- Mass model

  The background mass PDF can be modeled using a different PDF, and an exponential function is selected for the nominal fit. A first order polynomial function is used in the fit to assess the error associated to this selection. The differences between the fit using the polynomial and the nominal fit are considered systematic uncertainties.

- Lifetime model

  The PDF of the proper decay distance of the background is parameterized by two decay functions, one for the short lived particles and the other for the long lived ones. Nevertheless, the PDF of the lifetime can be modeled as well using three decays functions. To evaluate the systematic uncertainty associated with the lifetime model selection, the nominal model is modified using three decay functions. The difference in the extracted physical parameters with respect to the parameters obtained from the nominal fit are taken as systematic uncertainties.

- Angular model

  The angular PDFs are parameterized using Legendre functions. However, the parameterization is not perfect. To calculate the uncertainty associated to this selection, three histograms obtained from the side-bands are included in the fit instead of fitting the sidebands shapes. With the modified PDF, 366 pseudo-experiments are performed. The mean error from the simulation times the nominal statistical error is considered systematic uncertainty.

- Peaking B^0 background

  The misreconstruction of the $B^0 \to J/\psi\ K^* \to \mu^+\mu^- K^{(+/-)}\pi^{-/+}$ as $B_s^0 \to J/\psi\ \phi \to \mu^+\mu^- K^+K^-$ events may produce some bias. The nominal PDF does not include the peaking $B^0 \to J/\psi\ K^* \to \mu^+\mu^- K^{(+/-)}\pi^{-/+}$ contribution. To study this effect, pseudo-experiments are performed modifying the nominal fit by adding a third term that accounts for the B^0 peaking background. The

peaking background PDF is built using the MC sample $B^0 \rightarrow J/\psi\, K^* \rightarrow \mu^+\mu^- K^{(+/-)}\pi^{-/+}$. The ratio of misreconstructed events is obtained from the MC sample (as explained in section 5.1.2).

$$L(\alpha) = \prod_{i=1}^{N}[N_s\{\mathcal{P}(\Theta_i, \alpha, t_i, M_i)\}+ \\ N_b\{\mathcal{B}(\Theta_i, t_i, M_i)+ \\ \mathcal{P}B(\Theta_i, t_i, M_i)\}],$$

where N is the number of events, $\mathcal{P}$ is the signal PDF, $\mathcal{B}$ is the non peaking background PDF, $\mathcal{P}B$ is the peaking background PDF, N_B is the number of background events, and N_s is the number of signal events.

The biggest difference with the nominal fit result is taken as systematic uncertainties.

5.6.3 Dependence of the efficiency on the decay length

In this section are presented the biases associated to the efficiency calculation. There are two main sources of errors, one is related to the shape of the efficiency curve, and the other one related to the parameters of the efficiency curve. The systematic uncertainties are shown for the proper decay length dependent efficiency, and angular efficiencies as follows:

- Decay length dependent parameters

  The systematic errors due to proper decay length dependent efficiency are estimated using the errors associated to each parameter of the parameterization function $\epsilon(ct)$. Each parameter of the parameterization is changed within its error and the fit is recalculated. The difference on the physics parameters α=$\{\Gamma_s$, $\Delta\Gamma_s$, $|A_0|^2$, $|A_\perp|^2$, $\delta_{||}\}$ with respect to the nominal results are taken as systematic effect.
  The proper decay length dependent efficiency $\epsilon(ct)$ depends on the parameters (k_i) where $i = 1, 4$. The parameters k_i are obtained using the changed parameter α_{k_i} fit performed at each stage. Then, the difference of values is $(\delta^{\alpha}_{k_i} = \alpha - \alpha_{k_i})$ and the final errors are computed like:

  $$\sigma^{\epsilon(ct)}_{\alpha} = V(\delta^{\alpha}_{k_i}/\sigma_{k_i}) \times C(k_i) \times V(\delta^{\alpha}_{k_i}/\sigma_{k_i})^T, \tag{5.19}$$

  where $C(k_i)$ is the covariance matrix. In this way the correlations between the k_i parameters are taken into account.

- Decay length dependent efficiency shape definition

  To estimate the systematic uncertainty due to the proper decay length efficiency, the multiple likelihood fit is performed without efficiency curve, and with a second order efficiency curve. The biggest difference with the nominal fit result is considered as systematic uncertainty.

- Angular parameters

  The angular efficiency corrections, for the $\cos\theta$, $\cos\psi$ and φ angles, are calculated in the same was as for the proper decay length dependent efficiency parameters correction. The final error is the quadratic sum of the single angle errors.

- Angular efficiencies shape definition

  The parameterization of the angles efficiency is performed using a set of Legendre polynomial functions for each angle. To study the systematic errors associated to the shape of the angles efficiency curves, the fit is re-calculated using the efficiency histograms directly into the full PDF. The efficiency histogram has the following shape: One dimension histogram for the $\cos\theta$, and a two-dimensional histogram for the angles ($\cos\psi$, φ) to account for a possible correlation in the last two angular variables. 1250 pseudo-experiments are performed with the modified PDF. The mean error from the simulation times the nominal statistical error is considered systematic uncertainty.

5.6.4 Full PDF model bias

There is an intrinsic bias associated to the full nominal model. In order to study this uncertainty, 1 250 pseudo-experiments were produced, using the same conditions as the nominal fit. The mean error from the simulation times the nominal statistical error is considered systematic uncertainty.

5.6.5 Summary

In this chapter a full untagged angular analysis is performed to disentangle the mass eigenstates of the $B_s^0 \to J/\psi\,\phi \to \mu^+\mu^- K^+ K^-$ channel and to extract the parameters Γ_s, $\Delta\Gamma_s$, $|A_0|^2$, $|A_\perp|^2$, and the strong phase $\delta_{||}$. To do so, a fitting technique is developed, based on the maximum-likelihood method. The probability density function (PDF) that describes the decay, includes signal and background contributions defined by Eq. 5.3. The signal PDF is defined by the theory, as explained in Section 5.1.1, and the background PDF is defined by an empirical model. The PDF describes the

observables $\cos\theta$, φ, $\cos\psi$, M, and t. For this thesis the CP violating phase ϕ_s is equal to zero, and the result presented of $\Delta\Gamma_s$ has a positive value, based on the verification of this property by [25].

The fit is performed in several steps. Firstly, the B_s^0 invariant mass distribution is fitted between [5.24, 5.49] GeV/c^2. Secondly, the sideband regions are fitted with the empirical model that defines the background PDF. Thirdly, the full likelihood fit is performed and the physical parameters are extracted. From the fit performed on the five observables of 19 200 event candidates, 14 556 $\pm$ 139 signal events are found with a decay width difference of $\Delta\Gamma_s = 0.048 \pm 0.024$ (stat.) $\pm$ 0.003 (syst.) ps^{-1}, and a lifetime of $\tau_s = 1.527 \pm 0.020$ (stat.) $\pm$ 0.010 (syst.) ps.

Chapter 6

Discussion

In the Standard Model, the oscillation frequency of the B_s^0 mesons is $\Delta m_s^{SM} = (17.3 \pm 2.6)\text{ps}^{-1}$, and the CP violation phase is expected to be small [26, 32, 33]:

$$\phi_s = -0.0363^{+0.0016}_{-0.0015} \text{ rad}, \tag{6.1}$$

implying that $\Delta\Gamma_s^{SM} \simeq 2|\Gamma_{12}^s|$ (from Eq. 2.19). As a consequence, the SM value for the decay width difference becomes:

$$\Delta\Gamma_s^{SM} \simeq 2|\Gamma_{12}| = (0.087 \pm 0.021) \text{ ps}^{-1}, \tag{6.2}$$

where $\Delta\Gamma_s^{SM}/\Gamma_s \simeq 2|\Gamma_{12}|/\Gamma_s = 0.133 \pm 0.032$.

As explained in Section 2.5, the latest experimental values of the width difference of $\Delta\Gamma_s$ are obtained performing time-dependent analyses of the $B_s^0 \to J/\psi\ \phi$ decay rate at the experiments CDF [36], D0 [35], ATLAS [34] and LHCb [19].

The two experiments from the Fermilab Tevatron Collider obtained their results at $\sqrt{s} = 1.96$ TeV. The CDF experiment accumulated a luminosity of 9.6 fb^{-1} of data, and the D0 experiment a luminosity of 8 fb^{-1}. The referenced studies are performed using flavor tagged decay $B_s^0 \to J/\psi\ \phi$. One of the main characteristics of these analyses is the use of multivariate techniques to discriminate signal from background events. In the D0 study the systematic uncertainties are not detailed in their results. For the CDF analysis the biggest systematic uncertainties derive from the imperfect knowledge of the vertex detector alignment for the lifetime measurement Γ_s, and the decay time model of the background events for the measurement of the decay width difference $\Delta\Gamma_s$.

From the LHC accelerator, the LHCb experiment presented the results using a tagged analysis with an integrated luminosity of 1 fb^{-1} of data at $\sqrt{s} = 7$ TeV. LHCb obtained the first observation of $\Delta\Gamma_s$ different from zero and is currently the most

precise value for $\Delta\Gamma_s$ and the CP violation phase ϕ_s [25]. The analysis performed a study of the CP asymmetry in $B_s^0 \to J/\psi\ K^+K^-$, being the dominant contribution the $B_s^0 \to J/\psi\ \phi$ decay. In the selection process of the $B_s^0 \to J/\psi\ K^+K^-$ the range of the invariant mass of the K^+K^- is broader that the $\phi(1020)$ invariant mass window applied in this thesis (the events selected are within $\pm 30 \text{MeV/c}^2$ window around the $\phi(1020)$ mass) to include the K^+K^- resonances and increase the statistics.

Finally, the ATLAS detector published an untagged analysis of $B_s^0 \to J/\psi\ \phi$ [34] with an integrated luminosity of 4.9 fb^{-1} of data at $\sqrt{s} = 7$ TeV. This analysis is the more similar to this thesis. The difference is that the ATLAS result let float the value of the CP violating phase ϕ_s, and the trigger path used does not require a displacement from the vertex.

Table 2.2 summarizes the aforementioned results from the different experiment, including the results shown in this thesis which are the current public result from the CMS collaboration. Figure 6.1 shows the plane ($\Delta\Gamma_s$, ϕ_s), indicating the measurements from CDF, D0, LHCb, ATLAS and the Standard Model result. The result from this thesis is also shown for reference. The combined region in Fig. 6.1 will be pushed towards lower values with the inclusion of the results of this dissertation. Both Fig. 6.1 and Table 6.1 show that the results presented in this thesis, are in agreement within the errors with the Standard Model predictions. However, the results from ATLAS and CMS are around two sigmas away from the LHCb results. The main difference between the analyses is that ATLAS and CMS performed untagged analyses, while LHCb is based on flavor tagged decay. As explained before, LHCb analyzes the decay channel $B_s^0 \to J/\psi\ K^+K^-$, increasing the statistic. In addition, the LHCb detector has been optimized for the study of heavy flavor physics, their bandwidth is dedicated to b-physics events, and having a particle identification detector allows a better reduction of the backgrounds.

Table 6.1: Summary of the $\Delta\Gamma_s$ and $\Delta\Gamma_s/\Gamma_s$ from the D0 and CDF experiments from the Tevatron accelerator, and LHCb, ATLAS, and CMS experiments from the LHC accelerator.

Experiment	$\Delta\Gamma_s$ (ps^{-1})	Γ_s (ps^{-1})	$\Delta\Gamma_s$ /Γ_s
D0	$0.163^{+0.065}_{-0.064}$	$0.693^{+0.018}_{-0.017}$	0.235
CDF	0.068 ± 0.026 (stat.) ± 0.009 (syst.)	0.654 ± 0.008 (stat.) ± 0.004 (syst.)	0.105 ± 0.048
LHCb	0.100 ± 0.016 (stat.) ± 0.003 (syst.)	0.663 ± 0.005 (stat.) ± 0.006 (syst.)	0.151 ± 0.024
ATLAS	0.053 ± 0.021 (stat.) ± 0.010 (syst.)	0.677 ± 0.007 (stat.) ± 0.004 (syst.)	0.078 ± 0.031
CMS	0.048 ± 0.024 (stat.) ± 0.003 (syst.)	0.655 ± 0.009 (stat.) ± 0.003 (syst.)	0.073 ± 0.037
(This thesis)			

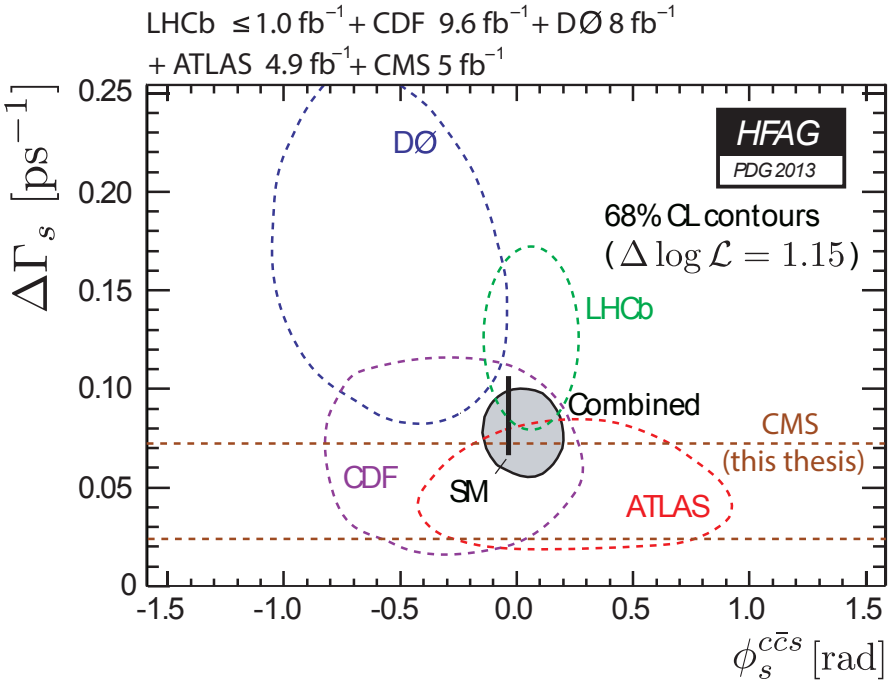

Figure 6.1: $\Delta\Gamma_s$ vs. ϕ_s plane showing the measurements from CDF, D0, ATLAS, and LHCb with their combination [12]. I have added the $\Delta\Gamma_s$ value obtained from CMS.

Chapter 7

Conclusions

This thesis focuses on the study of the decay channel $B_s^0 \to J/\psi\ \phi \to \mu^+\mu^- K^+K^-$ to measure the width difference $|\Delta\Gamma_s|$ between the light and heavy eigenstates of the B_s^0 meson. The analysis is performed using an integrated luminosity of 5 fb^{-1} collected in proton-proton collisions at $\sqrt{s} = 7$ TeV taken by the CMS detector at the LHC.

After the reconstruction and selection of the B_s^0 meson decaying into J/ψ ($\to \mu^+\mu^-$) and $\phi(1020)$ ($\to K^+K^-$) mesons, explained in Chapter 4, a full untagged angular analysis is performed to disentangle the mass eigenstates of the $B_s^0 \to J/\psi\ \phi$ channel and to extract the parameters Γ_s, $|\Delta\Gamma_s|$, $|A_0|^2$, $|A_\perp|^2$, and the strong phase $\delta_{||}$, detailed in Chapter 5. For this work it is assumed that the CP violating phase ϕ_s is equal to zero. The results are only given for a positive value of $\Delta\Gamma_s$, as measured in Ref. [25]. From a sample of 19 200 event candidates, $14\,556 \pm 139$ B_s^0 events are found, with a B_s^0 mean mass of $5\,366.8 \pm 0.1$ (stat.) MeV/c^2. The final values obtained from the maximum likelihood fit of the angular analysis together with their systematic uncertainties are shown in Table 7.1.

The validations of the full PDF presented in Section 5.4 show stable performance of the methods used in this work. The studies of the different possible triggers, while investigating the resolution effects in the proper decay length in the Section 5.2.1, confirm that the triggering and analysis methods used are appropriate for the width difference $\Delta\Gamma_s$ measurement in the $B_s^0 \to J/\psi\ \phi \to \mu^+\mu^- K^+K^-$ decay channel of the CMS experiment. It would be advisable nevertheless to insist in maintaining the triggers without cuts on the decay length for validation of the methods in future analyses. An upgrade of this analysis would be the inclusion of the resonances in K^+K^- and to perform a flavor tagged analysis.

Table 7.1: Results obtained in this thesis from the multiple likelihood fit on data.

Variable	Value	Statistical error	Systematic uncertainty
$\|A_0\|^2$	0.528	0.009	0.009
$\|A_\perp\|^2$	0.251	0.014	0.014
$\delta_{\|\|}$ (rad.)	2.79	0.14	0.42
$\Delta\Gamma_s$ (ps^{-1})	0.048	0.024	0.003
τ_s (ps)	1.527	0.020	0.007

Appendix A

Comparison between 2011-A and 2011-B datasets

This appendix summarizes the comparisons that have been made to ensure that the datasets 2011-A and 2011-B could be combined for a single analysis. The specifications of each dataset are detailed in Section 4.1.

First, the kinematic distributions of the four-track candidates are revised[1].

Distribution of the distance of closest approach (DCA) of the two muons. Figure A.1 shows the normalized distribution of the DCA of the two muons, the significance value DCA/σ_{DCA}, and the separation angle $\cos(\Delta\alpha)$.

Distribution of the pseudo-rapidity of the two muons. Figure A.2 shows that the normalized distribution of the pseudo-rapidity of the muons does not present any drastic differences.

Distribution of the transverse momentum p_T of the muon and kaon candidates. Figure A.3 presents the normalized p_T distributions of the two muons and the two kaons. Figure A.4 shows the normalized p_T distributions of the J/ψ and $\phi(1020)$ mesons.

Second, the kinematic distributions of the B_s^0 meson candidates are compared for both datasets.

Distribution of the p_T and η of the B_s^0 meson candidates. Figure A.5 displays the normalized distributions or p_T and η for the B_s^0 event candidates. The comparisons

[1]The distributions of the kinematic variables of the muons are the first variables to be compared because both datasets had different cuts on the J/ψ displaced trigger paths. This comparison verifies that the offline cuts make the full dataset uniform.

of the two datasets do not show any drastic differences that could affect the angular analysis.

Distribution of the vertex probability of the di-muon and the B_s^0 meson candidates. The selection of these variables was motivated because the vertex probability is one of the selection cuts applied at trigger level. Figure A.6 compared the probability distributions for the two datasets. There are no significant differences between the two datasets, showing that the vertex probabilities to select the J/ψ and B_s^0 candidates are not dependent on the number of primary vertices reconstructed.

Distribution of the significance decay length cut of the B_s^0 meson. Figure A.7 presents the distribution of the decay length significance, which is defined as $L_{xy}/\sigma_{L_{xy}}$. This distribution is very important, because it affects directly the proper decay time measurement. The distribution comparison between the two samples does not show discrepancies.

Finally, the distributions of the following observables used in the fit are compared: B_s^0 invariant mass, proper decay time, and the three angles $\cos\theta$, φ, $\cos\psi$.

Distribution of the main observables. Figure A.8 and Fig. A.9 shows the distribution comparison of the main observables presented in the Multiple Likelihood Fit B_s^0 invariant mass, proper decay time ct, and the three angles that describes the kinematics of the decay $\cos\theta$, φ, $\cos\psi$. In the comparisons there is no significance difference between the variables for both datasets.

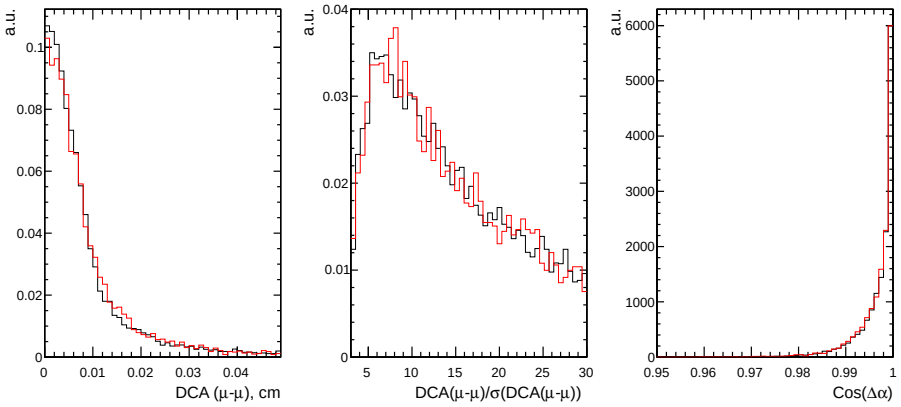

Figure A.1: Normalized distribution of the distance of closet approach of the two muons (DCA) (left), significance of the DCA (center), and normalized distribution of $\cos(\Delta\alpha)$ (right). The dataset 2011-A is shown in red, and the dataset 2011-B in black.

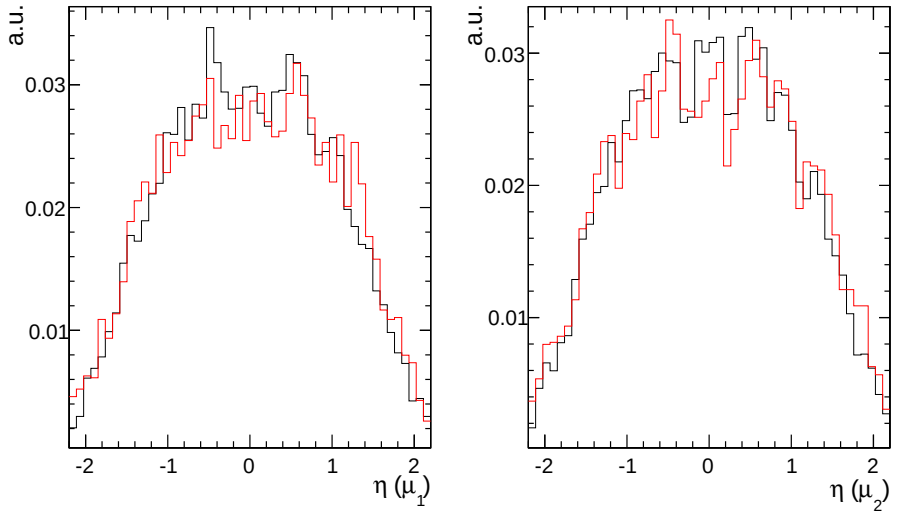

Figure A.2: Normalized η distribution for each muon candidate. The figure in the left shows the distribution $\eta(\mu^+)$, and the distribution $\eta(\mu^-)$ is shown in the right. The dataset 2011-A is shown in red, and the dataset 2011-B in black.

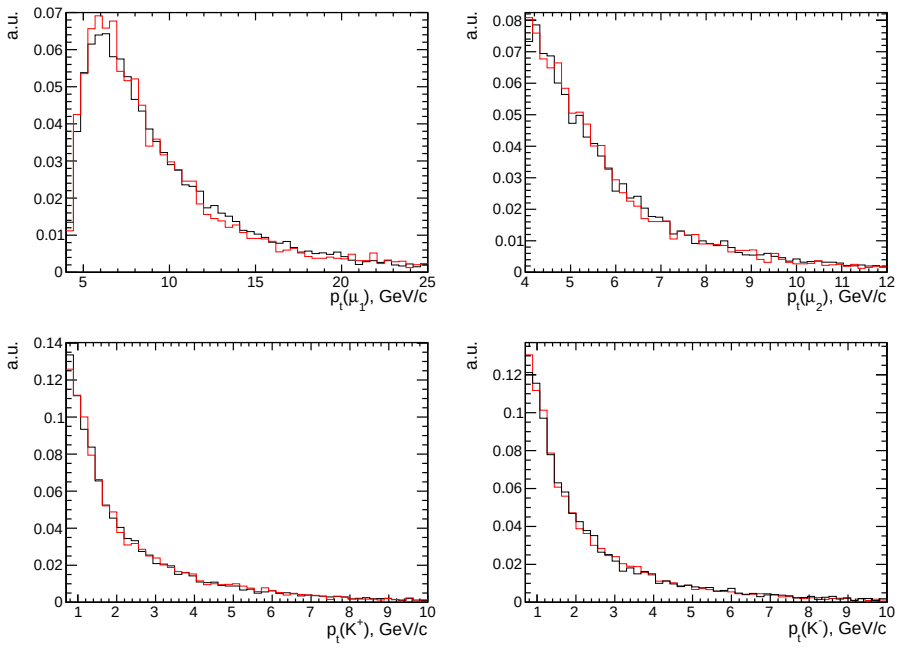

Figure A.3: Normalized distributions of the p_T of the $\mu^+\mu^-K^+K^-$ track candidates. The upper left figure is the p_T (μ^+), and in the the upper right is p_T (μ^-). The p_T (K^+) is presented in the left, and in the lower right is presented the distribution of p_T (K^-). The dataset 2011-A is shown in red, and the dataset 2011-B in black

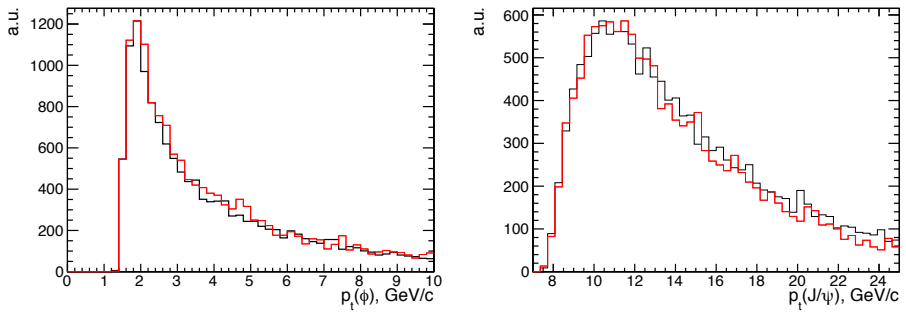

Figure A.4: Normalized distribution of the transverse momentum of J/ψ meson, and the $\phi(1020)$ meson. The dataset 2011-A is shown in red, and the dataset 2011-B in black.

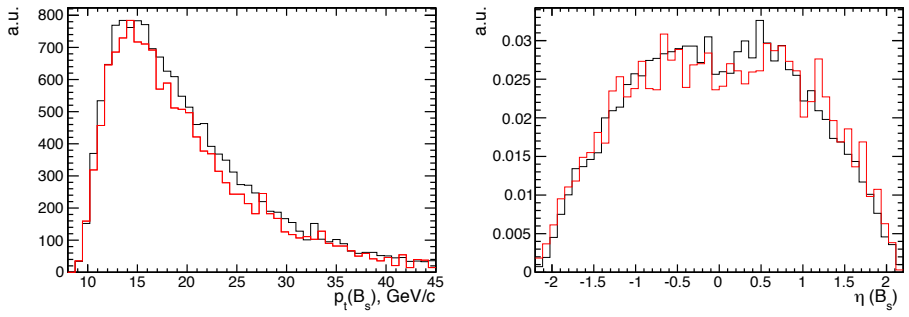

Figure A.5: Normalized distribution of the p_T (B_s^0) candidates, and $\eta(B_s^0)$ candidates for the two different datasets obtained from 2011 run. The dataset 2011-A is shown in red, and the dataset 2011-B in black.

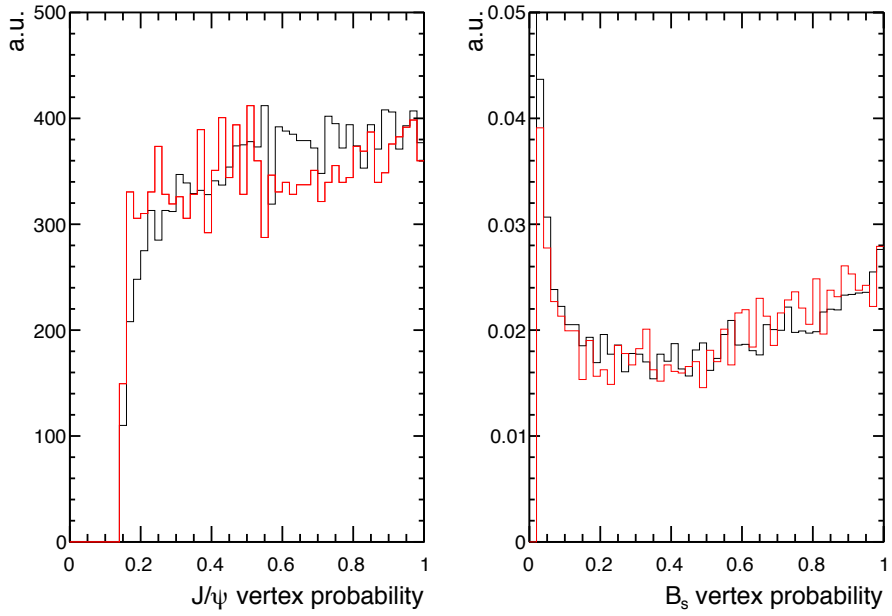

Figure A.6: Normalized distribution of the reconstruction vertex probability for the J/ψ di-muon candidates (left), and B_s^0 meson candidates (right). The dataset 2011-A is shown in red, and the dataset 2011-B in black.

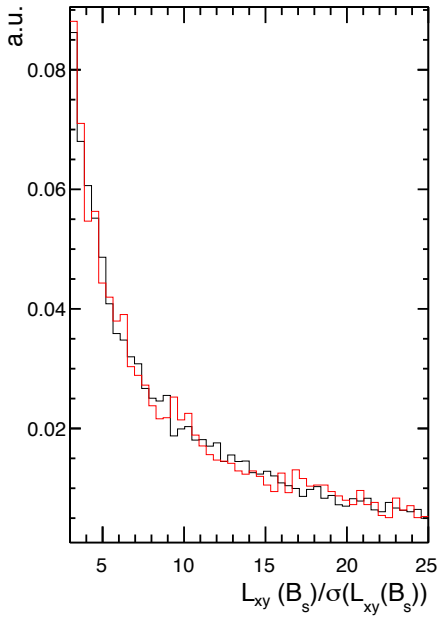

Figure A.7: Normalized distribution of the significance decay length of the B_s^0 meson candidates. The dataset 2011-A is shown in red, and the dataset 2011-B in black.

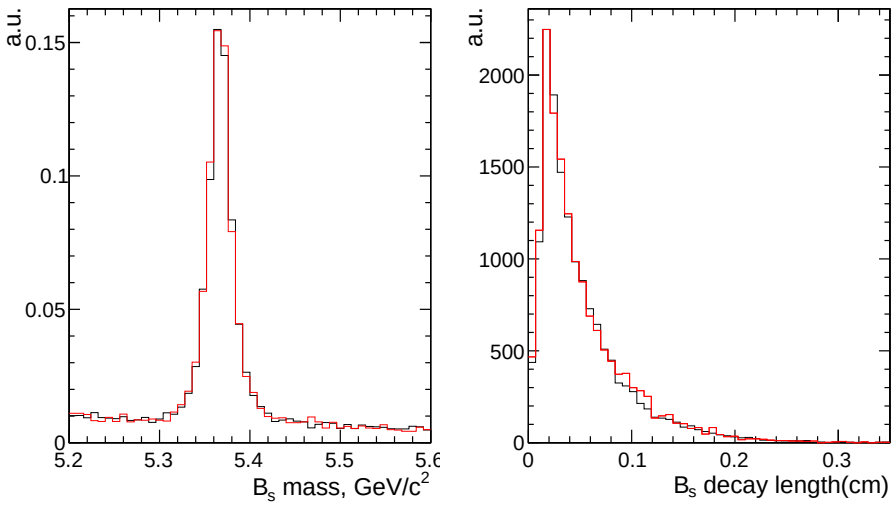

Figure A.8: Normalized distribution of the mass (left), and time decay length (right) variables for the $B_s^0 \to J/\psi\ \phi \to \mu^+\mu^- K^+ K^-$ candidates. The dataset 2011-A is shown in red, and the dataset 2011-B in black.

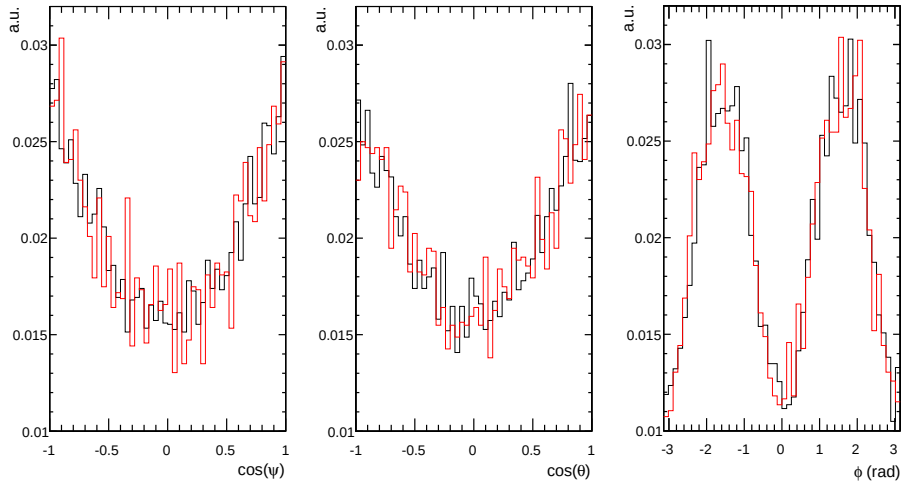

Figure A.9: Normalized distribution of the angles ($\cos\theta$, φ, $\cos\psi$) that defined the kinematics of the $B_s^0 \to J/\psi\ \phi$ decay. The figure in the left is the $\cos\psi$, the one in the center is $\cos\theta$, and the one far in the right is the φ. The dataset 2011-A is shown in red, and the dataset 2011-B in black.

Bibliography

[1] S. Glashow, "Partial Symmetries of Weak Interactions", *Nucl.Phys.* **22** (1961) 579. doi:10.1016/0029-5582(61)90469-2. (Cited on page 3.)

[2] L. Evans and P. Bryant, "LHC Machine", *Journal of Instrumentation* **3** (2008). (Cited on pages 3, 18, and 20.)

[3] ATLAS Collaboration, "Observation of a new boson at a mass of 125 GeV with the {CMS} experiment at the {LHC}", *Physics Letters B* **716** (2012), no. 1, 30. doi:http://dx.doi.org/10.1016/j.physletb.2012.08.021. (Cited on page 3.)

[4] CMS Collaboration, "Observation of a new particle in the search for the Standard Model Higgs boson with the {ATLAS} detector at the {LHC}", *Physics Letters B* **716** (2012) 1. doi:http://dx.doi.org/10.1016/j.physletb.2012.08.020. (Cited on page 3.)

[5] C. L. Bennett et al., "First-Year Wilkinson Microwave Anisotropy Probe (WMAP) Observations: Preliminary Maps and Basic Results", *The Astrophysical Journal Supplement Series* **148** (2003) 1. (Cited on page 3.)

[6] C. L. Bennett et al., "Nine-year Wilkinson Microwave Anisotropy Probe (WMAP) Observations: Final Maps and Results", *accepted to The Astrophysical Journal Supplement Series* (2012). (Cited on page 3.)

[7] H. G. F. et al., "Nine-year Wilkinson Microwave Anisotropy Probe (WMAP) Observations: Cosmological Results", *accepted to The Astrophysical Journal Supplement Series* (2012). (Cited on page 3.)

[8] CMS Collaboration, "Measurement of the lifetime difference $\Delta\Gamma_s$ in the decay $B_s \to J/\psi\,\phi$", technical report, CERN, (2012). (Cited on pages 4 and 44.)

[9] CMS Collaboration, "Measurement of the Bs lifetime difference", Technical Report CMS-PAS-BPH-11-006, CERN, Geneva, (2012). (Cited on page 4.)

[10] J. Christenson et al., "Evidence for the 2π Decay of the K_2^0 Meson", *Phys. Rev. Lett.* **13** (1964) 138. doi:10.1103/PhysRevLett.13.138. (Cited on pages 5 and 6.)

[11] M. Kobayashi and T. Maskawa, "CP-Violation in the Renormalizable Theory of Weak Interaction", *Progress of Theoretical Physics* **49** (1973) 652. doi:10.1143/PTP.49.652. (Cited on pages 5 and 6.)

[12] J. Beringer et al., "Review of Particle Physics", *Phys. Rev. D* **86** (2012). doi:10.1103/PhysRevD.86.010001. (Cited on pages 5, 6, 8, 9, 10, 16, 40, 44, 53, 55, 74, 86, 104, and 106.)

[13] G. Luders, "Proof of the TCP theorem", *Annals of Physics* **2** (1957) 1. doi:10.1016/0003-4916(57)90032-5. (Cited on page 6.)

[14] C. S. Wu et al., "Experimental Test of Parity Conservation in Beta Decay", *Phys. Rev.* **105** (1957). doi:10.1103/PhysRev.105.1413. (Cited on page 6.)

[15] S. W. Herb et al., "Observation of a Dimuon Resonance at 9.5 GeV in 400-GeV Proton-Nucleus Collisions", *Phys. Rev. Lett.* **39** (1977) 252. doi:10.1103/PhysRevLett.39.252. (Cited on page 6.)

[16] CDF Collaboration, "Observation of top quark production in $\bar{p}p$ collisions", *Phys.Rev.Lett.* **74** (1995) 2626. doi:10.1103/PhysRevLett.74.2626. (Cited on page 6.)

[17] L. Wolfenstein, "Parametrization of the Kobayashi-Maskawa Matrix", *Phys. Rev. Lett.* **51** (1983) 1945. doi:10.1103/PhysRevLett.51.1945. (Cited on page 7.)

[18] C. Jarlskog, "Commutator of the Quark Mass Matrices in the Standard Electroweak Model and a Measure of Maximal CP Nonconservation", *Phys.Rev.Lett.* **55** (1985). doi:10.1103/PhysRevLett.55.1039. (Cited on page 8.)

[19] LHCb Collaboration, "Measurement of CP violation and the B_s^0 meson decay width difference with $B_s^0 \to J/\psi K^+K^-$ and $B_s^0 \to J/\psi\pi^+\pi^-$ decays", *Submitted to Phys. Rev. D* (2013) arXiv:1304.2600. (Cited on pages 8, 17, and 84.)

[20] J. Charles et al., "CP violation and the CKM matrix: assessing the impact of the asymmetric B factories", *The European Physical Journal C - Particles and Fields* **41** (2005) 1. doi:10.1140/epjc/s2005-02169-1. (Cited on pages 9, 10, and 102.)

[21] CDF Collaboration, "Measurement of the CP-Violating Phase $\beta_s^{J/\Psi\phi}$ in $B_s^0 \to J/\Psi\phi$ Decays with the CDF II Detector", *Phys.Rev.* **D85** (2012) arXiv:1112.1726. doi:10.1103/PhysRevD.85.072002. (Cited on pages 10 and 102.)

[22] LHCb Collaboration, "Measurement of the CP-violating phase ϕ_s in the decay $B_s^0 \to J/\psi\phi$", *Phys.Rev.Lett.* **108** (2012) arXiv:1112.3183. doi:10.1103/PhysRevLett.108.101803. (Cited on pages 10 and 102.)

[23] CDF Collaboration, "Observation of $B_s^0 - \overline{B}_s^0$ Oscillations", *Phys.Rev.Lett.* **97** (2006). doi:10.1103/PhysRevLett.97.242003. (Cited on page 9.)

[24] LHCb Collaboration, "Measurement of the $B_s^0 - \bar{B}_s^0$ oscillation frequency Δm_s in $B_s^0 \to D_s^-(3)\pi$ decays", *Physics Letters B* **709** (2012) 177. doi:10.1016/j.physletb.2012.02.031. (Cited on pages 10 and 16.)

[25] LHCb Collaboration, "Determination of the sign of the decay width difference in the B_s system", *Phys.Rev.Lett.* **108** (2012) 241801. doi:10.1103/PhysRevLett.108.241801. (Cited on pages 11, 16, 50, 83, 85, and 87.)

[26] A. Lenz and U. Nierste, "Numerical Updates of Lifetimes and Mixing Parameters of B Mesons", *Phys.Rev.Lett.* (2011) arXiv:1102.4274. (Cited on pages 12, 16, and 84.)

[27] A. Lenz and U. Nierste, "Theoretical update of $B_s - \bar{B}_s$ mixing", *JHEP* **0706** (2007) 072. doi:10.1088/1126-6708/2007/06/072. (Cited on page 12.)

[28] K. Anikeev et al., "B physics at the Tevatron: Run II and beyond", arXiv:hep-ph/0201071. (Cited on page 12.)

[29] A. S. Dighe et al., "Angular distributions and lifetime differences in $B_s \to J/\psi\phi$ decays", *Phys.Lett.* **B369** (1996) 144. doi:10.1016/0370-2693(95)01523-X. (Cited on pages 13 and 14.)

[30] I. Dunietz, R. Fleischer, and U. Nierste, "In pursuit of new physics with B_s decays", *Phys. Rev. D* **63** (2001) 114015. doi:10.1103/PhysRevD.63.114015. (Cited on page 14.)

[31] Y. Xie et al., "Determination of $2\beta_s$ in $B_s^0 \to J/\psi\, K^+K^-$ decays in the presence of a K^+K^- S-wave contribution", *Journal of High Energy Physics* **2009** (2009) 74. (Cited on pages 14 and 79.)

[32] The CKMfitter Group Collaboration, "Predictions of selected flavor observables within the standard model", *Phys. Rev. D* **84** (2011) 033005. doi:10.1103/PhysRevD.84.033005. (Cited on pages 16 and 84.)

[33] Heavy Flavor Averaging Group Collaboration, "Averages of B-Hadron, C-Hadron, and tau-lepton properties as of early 2012", arXiv:1207.1158. (Cited on pages 16 and 84.)

[34] ATLAS Collaboration, "Time-dependent angular analysis of the decay $B_s^0 \to J/\psi\phi$ and extraction of $\Delta\Gamma_s$ and the $CP-violating$ weak phase ϕ_s by ATLAS ", *JHEP* **1212** (2012) 072. doi:10.1007/JHEP12(2012)072. (Cited on pages 17, 84, and 85.)

[35] D0 Collaboration, "Measurement of the CP-violating phase $\phi_s^{J/\psi\phi}$ using the flavor-tagged decay $B_s^0 \to J/\psi\phi$ in 8 fb^{-1} of $p\bar{p}$ collisions", *Phys.Rev.* **D85** (2012) 032006. doi:10.1103/PhysRevD.85.032006. (Cited on pages 17 and 84.)

[36] CDF Collaboration, "Measurement of the Bottom-Strange Meson Mixing Phase in the Full CDF Data Set", *Phys.Rev.Lett.* **109** (2012) 171802. doi:10.1103/PhysRevLett.109.171802. (Cited on pages 17 and 84.)

[37] C. Lefèvre, "The CERN accelerator complex. Complexe des accélérateurs du CERN", (2008). (Cited on pages 19 and 102.)

[38] G. L. Bayatian et al., "CMS Physics: Technical Design Report Volume 1: Detector Performance and Software". Technical Design Report CMS. CERN, Geneva, 2006. (Cited on pages 23, 30, and 36.)

[39] V. Karimaki, "The CMS tracker system project: Technical Design Report". Technical Design Report CMS. CERN, Geneva, 1997. (Cited on page 23.)

[40] C. Amsler et al., "Mechanical Design and Material Budget of the CMS Barrel Pixel Detector", *Journal of Instrumentation* **4** (2009) P05003. doi:10.1088/1748-0221/4/05/P05003. (Cited on pages 23 and 24.)

[41] CMS Collaboration, "Commissioning and performance of the CMS silicon strip tracker with cosmic ray muons", *Journal of Instrumentation* **5** (2010) T03008. (Cited on page 24.)

[42] CMS Collaboration, "The CMS experiment at the CERN LHC", *JINST* **3** (2008) S08004. doi:10.1088/1748-0221/3/08/S08004. (Cited on pages 25 and 102.)

[43] R. E. Kalman, "A New Approach to Linear Filtering and Prediction Problems", *Transactions of the ASME–Journal of Basic Engineering* **82** (1960) 35. (Cited on page 28.)

[44] S. Cucciarelli et al., "Track reconstruction, primary vertex finding and seed generation with the Pixel Detector", Technical Report CMS-NOTE-2006-026, CERN, Geneva, (2006). (Cited on page 29.)

[45] R. Frühwirth, W. Waltenberger, and P. Vanlaer, "Adaptive Vertex Fitting", Technical Report CMS-NOTE-2007-008, CERN, Geneva, (2007). (Cited on page 30.)

[46] T. Speer et al., "Vertex Fitting in the CMS Tracker", Technical Report CMS-NOTE-2006-032, CERN, Geneva, (2006). (Cited on page 30.)

[47] CMS Collaboration, "Tracking and Primary Vertex Results in First 7 TeV Collisions", Technical Report CMS-PAS-TRK-10-005, CERN, (2010). (Cited on page 30.)

[48] CMS Collaboration, "Alignment of the CMS silicon tracker during commissioning with cosmic rays", *Journal of Instrumentation* **5** (2010) T03009. (Cited on pages 30 and 31.)

[49] R. Castello, "Alignment of CMS Tracker detector using cosmic ray particles and its impact on early physics performance". PhD thesis, Università degli Studi di Torino, 2010. (Cited on page 30.)

[50] O. Brandt, "Alignment of the ATLAS Inner Detector Tracking System",. (Cited on pages 31 and 102.)

[51] W. Adam et al., "Alignment of the CMS silicon strip tracker during stand-alone commissioning", *Journal of Instrumentation* **4** (2009) T07001. (Cited on page 31.)

[52] G. Flucke and the CMS Collaboration, "Alignment of the CMS silicon tracker", *Journal of Physics: Conference Series* **368** (2012) 012036. (Cited on page 31.)

[53] V. Karimaki, T. Lampen, and F.-P. Schilling, "The HIP Algorithm for Track Based Alignment and its Application to the CMS Pixel Detector", Technical Report CMS-NOTE-2006-018, CERN, (2006). (Cited on page 31.)

[54] V. Blobel and C. Kleinwort, "A New method for the high precision alignment of track detectors", arXiv:hep-ex/0208021. (Cited on page 31.)

[55] "PHYSICS AT THE TERASCALE, Helmholtz Alliance". https://www.wiki.terascale.de/index.php/Millepede_II, December, 2012. (Cited on page 31.)

[56] CMS Collaboration, "Measurement of CMS Luminosity", Technical Report CMS-PAS-EWK-10-004, CERN, 1900. Geneva, (2010). (Cited on page 21.)

[57] T. Sjostrand, S. Mrenna, and P. Z. Skands, "PYTHIA 6.4 Physics and Manual", *JHEP* **0605** (2006) 026. doi:10.1088/1126-6708/2006/05/026. (Cited on page 34.)

[58] D. J. Lange, "The EvtGen particle decay simulation package", *Nuclear Instruments and Methods in Physics Research Section A: Accelerators, Spectrometers, Detectors and Associated Equipment* **462** (2001) 152. doi:10.1016/S0168-9002(01)00089-4. (Cited on page 34.)

[59] S. Agostinelli et al., "Geant4—a simulation toolkit", *Nuclear Instruments and Methods in Physics Research Section A: Accelerators, Spectrometers, Detectors and Associated Equipment* **506** (2003) 250. doi:10.1016/S0168-9002(03)01368-8. (Cited on page 34.)

[60] T. du Pree, "Search for a Strange Phase in Beautiful Oscillations". PhD thesis, Vrije Universiteit, Amsterdam, 2010. (Cited on pages 36 and 61.)

[61] L. Wilke, "Study of the Bs-Meson with the First LHC Data". PhD thesis, Zürich Universität, 2009. (Cited on pages 36, 38, 40, 44, 60, and 103.)

[62] K. Prokofiev, "Study of the $B_s^0 \to (J/\psi)\phi \to (\mu^+\mu^- K^+ K^-)$ Decay with the CMS Detector at LHC". PhD thesis, Zürich Universität, Zurich, 2005. (Cited on page 40.)

[63] CMS Collaboration, "Measurement of the Strange B Meson Production Cross Section with J/Psi ϕ Decays in pp Collisions at $\sqrt{s} = 7$ TeV", *Phys.Rev.* **D84** (2011) 052008. doi:10.1103/PhysRevD.84.052008. (Cited on page 44.)

[64] G. Cowan, "Statistical Data Analysis". Clarendon Press, Oxford, 2008. (Cited on page 50.)

[65] S. Stone and L. Zhang, "S-waves and the measurement of CP violating phases in B_s decays", *Phys. Rev. D* **79** (2009) 074024. doi:10.1103/PhysRevD.79.074024. (Cited on page 79.)

List of Figures

List of Tables